Modeling and Analysis of a Flywheel Energy Storage System for Voltage Sag Correction

A Thesis

Presented in Partial Fulfillment of the Requirements for the

Degree of Master of Science

With a

Major in Electrical Engineering

in the

College of Graduate Studies

University of Idaho

by

Satish Samineni

December 2003

Major Professor: Brian K. Johnson, Ph.D.

ABSTRACT

A shipboard power system is a stiff, isolated power system. Power is generated locally, and distributed over short distances making the system vulnerable to system transients. Power quality problems such as voltage sags, which arise due to a fault or a pulsed load, can cause interruptions of critical loads. This can be of a serious concern for the survivability of a combat ship. A series voltage injection type flywheel energy storage system is used to mitigate voltage sags. The basic circuit consists of an energy storage system, power electronic interface and a series connected transformer. In this case the energy storage system consists is a flywheel coupled to an induction machine. The power electronic interface consists of two voltage sourced converters (VSC) connected through a common DC link. The flywheel stores energy in the form of kinetic energy and the induction machine is used for energy conversion. Bi-directional power flow is maintained by regulating the DC bus voltage. Indirect field orientated control with space vector PWM is used to control the induction machine. Sinusoidal PWM is used for controlling the power system side VSC. This paper presents the modeling, simulation and analysis of a flywheel energy storage system and with a power converter interface using EMTDC.

ACKNOWLEDGEMENTS

I would like to thank my advisor Dr. Brian K. Johnson for giving me the opportunity to work on this thesis. I am greatly indebted for his encouragement, support and guidance given during this project. It is an honor and pleasure to have him as my advisor.

I am greatly thankful to Dr. Herbert L. Hess for his fruitful discussions and valuable suggestions throughout this project. His approach of solving complicated problems with simplified analysis helped greatly in this thesis.

I also wish to thank Dr. Dean B. Edwards for his interest in this topic and patience during the preparation of this thesis.

I am thankful to Dr. Joseph D. Law for sharing his technical knowledge and spending his valuable time during the crucial part of this thesis.

Financial supports from the Office of Naval Research and Department of Electrical and Computer Engineering are greatly acknowledged.

DEDICATION

"Dedicated to my beloved parents, brother and sister who have provided me encouragement and support throughout my studies"

TABLE OF CONTENTS

Preliminary

LIST OF FIGURES

LIST OF TABLES

1.0 INTRODUCTION

1.1 Flywheel basics

Flywheels have been used for a long time as mechanical energy storage devices. The earliest form of a flywheel is a potter's wheel that uses stored energy to aid in shaping earthen vessels [1]. The wheel is a disc made of wood, stone or clay. It rests on a fixed pivot and can be rotated around its center. The energy stored in a potter's flywheel is about 500J, which is by no means negligible. The main disadvantages are friction and material integrity. Most of energy is lost in overcoming frictional losses.

The word 'flywheel' appeared first during the start of industrial revolution. During this period, there were two important developments: one is the use of flywheels in steam engines and the other is widespread use of iron. Iron flywheels have greater material integrity than flywheels made up of wood, stone or clay. They can be built in a single piece and can accommodate more mass and moment of inertia in the same volume. These flywheels were used mostly for smoothing torque pulses in steam engines.

In the years after industrial revolution, the trend was mostly towards increasing mass for higher energy storage rather than increasing speed. Large flywheels made of cast steel, with heavier rims, were built for the largest engines. However, with the advent of the small internal combustion engine in the middle of 19^{th} century, the trend shifted towards high-speed flywheels with low inertia for automotive applications. More recently, the ability of a flywheel to deliver high power in a short time has been used in applications such as mechanical presses, lubrication or cooling pumps, mine locomotives, inertial friction welding and inertial starters.

The constant stress profile for steam turbines, developed by De Laval and later by Stodola, was very useful in the design of high-speed flywheels. During the

Stodola period it was demonstrated that a rotating mass supported by a shaft stores energy mechanically.

The second part of 20th century saw advances in the field of high-strength composite materials. Composite flywheels can operate at higher speeds and can store more energy for a given mass than a conventional steel flywheel. These flywheels have high material integrity, can be operated at high speeds and, as will be shown below, store more energy. The concept of a flywheel energy storage system for electric vehicles and stationary power backup was proposed during this period. Also, a distinction has been made between the flywheels that are used for smoothing torque pulses and the flywheels that store energy for backup power applications.

Flywheels store energy in the form of kinetic energy. The amount of energy 'E' stored in a flywheel varies linearly with moment of inertia 'I' and with the square of the angular velocity 'ω'.

$$E = \frac{1}{2} \cdot I \cdot \omega^2 \tag{1.1}$$

The moment of inertia is a physical quantity, which depends on the mass and shape of the flywheel. It is defined as the integral of the square of the distance 'x' from the axis of rotation to the differential mass 'dm_x'.

$$I = \int x^2 \, dm_x \tag{1.2}$$

The solution for a cylindrical flywheel of mass 'm' and radius 'r' will be:

$$I = m \cdot r^2 \tag{1.2a}$$

and

$$E = \frac{1}{2} \cdot m \cdot r^2 \cdot \omega^2 \qquad (1.2b)$$

Since the energy stored is proportional to the square of angular velocity, increasing the angular speed increases stored energy more effectively than increasing mass. But increasing angular speeds results in increased frictional losses and hence thermal problems. With the help of magnetic bearing technology, the frictional losses due to bearings can be overcome, but at the expense of reliability.

Also the energy stored can be expressed in terms of peripheral velocity 'v', which is defined as the product of perpendicular distance from the axis of rotation and angular speed as:

$$E = \frac{1}{2} \cdot m \cdot v^2 \qquad \text{since} \qquad v = r \cdot \omega \qquad (1.3)$$

The tensile strength, σ, of the material limits the peripheral velocity, and hence the amount of energy stored. For a mass density 'ρ', the tensile strength is defined as:

$$\sigma = \rho \cdot v^2 \qquad (1.4)$$

Energy density is a term generally used to characterize an energy storage system. Usually high energy density is preferred, but this can pose thermal problems. Energy density, E_m, is loosely defined for a flywheel as the ratio of energy stored to its mass:

$$E_m = \frac{1}{2} \cdot r^2 \cdot \omega^2 \qquad (1.5)$$

The volume energy density, E_v, is obtained by substituting m in the stored energy equation, as the product of volume and the mass density:

$$E_v = \frac{1}{2} \cdot \rho \cdot r^2 \cdot \omega^2 \qquad (1.6)$$

Therefore, if the dimensions are fixed, the maximum energy stored per volume 'E_{vmax}' depends on the tensile strength of the material as:

$$E_{vmax} = \frac{1}{2} \cdot \sigma_{max} \tag{1.7}$$

where 'σ_{max}' is the maximum tensile strength of the flywheel material.

Similarly the maximum energy stored per mass 'E_{mmax}' is

$$E_{mmax} = \frac{1}{2} \cdot \frac{\sigma_{max}}{\rho} \tag{1.8}$$

Therefore, the maximum energy storage capacity can be achieved by using a material with a low density and high tensile strength. Depending on the application, either volume energy density or mass energy density takes precedence during the design stage. For a transportation application, mass energy density is a major consideration, since mass is a limiting factor.

The energy density expressions above apply for a simple rim type flywheel. There are many designs for flywheels, and the general expression of maximum energy stored per mass is:

$$E_{mmax} = K \cdot \frac{\sigma_{max}}{\rho} \tag{1.9}$$

where K is defined as the flywheel shape factor, which depends on the geometry of the flywheel. The flywheel shape factors for several different types of flywheels are given in Table 1.1.

The value of K is obtained from the equation for the moment of inertia (1.2). The stress distribution in a flywheel due to centrifugal loading becomes complex for shape factors greater than 0.5, and a detailed analysis needs to be done to safely achieve it.

For low speed flywheels, the best way to maximize stored energy is by increasing moment of inertia. A massive rim or disc made of high density material such as cast iron or steel is sufficient in these cases. The main advantages of low speed flywheels are that they use a well-established technology and they are cheaper to build.

For high-speed applications, small discs with a constant stress profile, built with a low density and high strength materials, are better for maximizing energy density. The most commonly used composite material is Kevlar, a plastic material reinforced with glass, carbon or aramid fibers. The main disadvantage of this material is its high cost. The cheapest composite material is S-glass, but this material has a lower fatigue strength. The specific strengths of different flywheel materials is listed in Table 1.2. A comparison of flywheel energy storage capabilities is given in Table 1.3.

There is also a safety factor, which limits the amount of stored energy available for discharge [2]. When this is considered, the useful energy stored per mass is given by:

$$E_m = \left(1 - s^2\right) \cdot K \cdot \frac{\sigma}{\rho} \tag{1.10}$$

where ‘s’ is the ratio of minimum to maximum operating speed, usually set at 0.2.

So the maximum amount of energy stored doesn’t depend directly on inertia or on the angular velocity, since either of these can be chosen independently to obtain the required design stress. And within the design stress, the amount of energy stored is linearly proportional to the moment of inertia and to the square of its angular velocity.

Table 1.1 Flywheel shape factors [1]

Flywheel Shape	K
Constant stress disk	0.931
Constant thickness disc	0.606
Thin rim	0.500
Constant stress bar	0.500
Rod or circular brush	0.333
Flat pierced disc	0.305

Table 1.2 Specific strengths of flywheel materials [1]

Flywheel material	Specific strength (kJ/kg)
Cast iron	19
Carbon steel	44
Alloy steel	100
Wood (beech)	130
Kevlar	1700
S-glass	1900
Graphite	8900

Table 1.3 Comparison of typical flywheel energy storage capabilities [2]

Material	**Density** 10^3 kg/m^3	**Useful Energy** 10^3 J/kg	**Mass of the flywheel** 10^3 kg
Wood birch	0.55	21.0	1720
Mild steel	7.80	29.5	1220
S-Glass	1.90	70.5	509
Maraging steel	8.00	86.4	417
Carbon 60% fibre	1.55	185.4	194
Kevlar 60% fibre	1.4	274.3	131

1.2 Shipboard Power System

The U.S. Navy is looking at methods to maximize the survivability of its combat ships during battle situations [3]. A typical shipboard power system is radial with bus tiebreakers to reconfigure it. There are usually three to four generators. Steam turbines, gas turbines, or diesel engines are used as prime movers for these generators. The generated 450V, 60Hz three-phase AC generator output is distributed throughout the ship over distances up to a few hundred meters. A number of three-phase step down transformers are used at the load centers to provide different voltage levels.

For survivability reasons, the primary and secondary windings of these transformers are connected in delta giving the system a floating neutral. This is done so that a single line to ground fault due to battle damage doesn't result in large currents flowing in the system since there is no path for the zero sequence current to flow (zero sequence impedance is very high). This blocks the protection devices from acting and hence prevents interruptions to critical loads. Another advantage of using this delta configuration is that an open circuit in the distribution line, or a loss of one leg of transformer, will still allow balanced power to be supplied at reduced levels. The main disadvantage of using this configuration is that a single line to ground fault will increase the phase to ground voltages on the unfaulted phases to 1.732 times. This can result in insulation failure and possibly cause interruptions to more loads. As a result, research being done on different grounding options for shipboard power system and how they impact the critical loads [3]. One option is to implement a solidly grounded system with fast reconfiguration during faults.

Since shipboard power systems are isolated and stiff (short electrical distances to loads), system transients can penetrate deep into the system. Critical loads such as computers, emergency lighting and communications, fire pumps, search radars, pumps and weapon systems are sensitive to these system transients. Keeping these loads operational plays a vital role in maximizing survivability of a combat ship during battle situations. These loads require continuous quality power for proper operation. System transients such as voltage sags, which arise due to

faults, can cause interruptions to critical loads. So isolating these critical loads from these transients is key to maximizing survivability.

In this thesis investigation, the shipboard power system is assumed to be a solidly grounded. The primary effort is on sag correction using a flywheel energy storage system. Whether grounded or ungrounded, three phase voltage sags seen by the critical loads are the same, so the correction of a balanced voltage sag was considered as a common test case. A similar argument can be made for phase to phase faults. SLG faults in an ungrounded system don't cause sags.

1.3. Voltage Sags

A voltage sag is a short duration phenomenon at power system frequency resulting in a decrease in the RMS voltage magnitude from 10% to 90% [4]. It typically lasts about half a cycle to a minute. Loads such as adjustable speed drives, process control equipment and computers are sensitive to these voltage sags. These loads may trip or misoperate even for voltage sag of 10% and lasting two cycles. Process industry applications such as paper mills and semiconductor fabrication plants take a lot of time to restart when tripped. Since they are production oriented, the impact of the voltage sag is enormous.

Voltage sags are quite common in modern power systems and generally caused by motor starting, transformer energizing, pulsed load switching and electrical faults. They are power quality problems. And the depth of the sag depends on the electrical distance to the point of cause.

The starting current of a large induction machine is typically 6-12 (starter compensators reduce it to 3-6) times the rated current when line started. The voltage drop caused by this starting current is the same in the three phases causing a balanced voltage sag. The voltage drops suddenly and recovers gradually as the machine reaches its rated speed. The same behavior occurs for large synchronous motors since most of them are started as induction machines before synchronization.

The inrush current due to the energization of a large transformer is typically 5 times the rated current. The voltage drops are different in each phase, resulting in an unbalanced sag. The voltage recovers gradually as the transformer reaches its rated flux.

However, the majority of voltage sags are due to electrical faults. Unlike the starting of large machines, voltage sags due to electrical faults are unpredictable. When a fault occurs in a power system, loads connected to the feeders that contribute current to the fault experience a voltage sag. In addition, loads down-stream from the fault, or from junctions to the faulted feeder, also experience a

voltage sag. This makes voltage sag a global phenomenon, compared to interruption where the isolation of faulted feeder causes a local disruption. The severity of the sag depends on the amount of fault current available at that feeder. In other words, the number of loads affected by voltage sags depends on the source impedance.

A voltage sag is generally characterized by depth and duration. The depth of the sag depends on the system impedance, fault distance, system characteristics (grounded or ungrounded) and fault resistance. The duration of the sag depends on the time taken by the circuit protection to clear the fault. High speed tripping is desired to limit the duration of sags.

Consider an example system with a source, a bus and two loads. One is a sensitive load, which is connected directly to the bus. The other is a distant load connected to the same bus through a distribution line. The characteristics of voltage sags were studied using this test setup for a number of different system configurations, different faults at the distance load.

The following test cases use a solidly grounded system with a three-phase fault at a distant load. The source is stiff as seen by the sensitive load. A three-phase fault occurs at the distant load terminals, which is cleared by the protection in five cycles.

Fig. 1.1 shows the trip signal for clearing the fault. Fig. 1.2 shows balanced voltage sag of 82% seen at the sensitive load due to this fault. Fig. 1.3 shows the RMS voltage measured at the sensitive load and at the distant load. Since it is a balanced fault, the negative and zero sequence (a little seen at t = 0.6 sec) currents from the feeder are zero (except during the transient state as seen in Fig. 1.4).

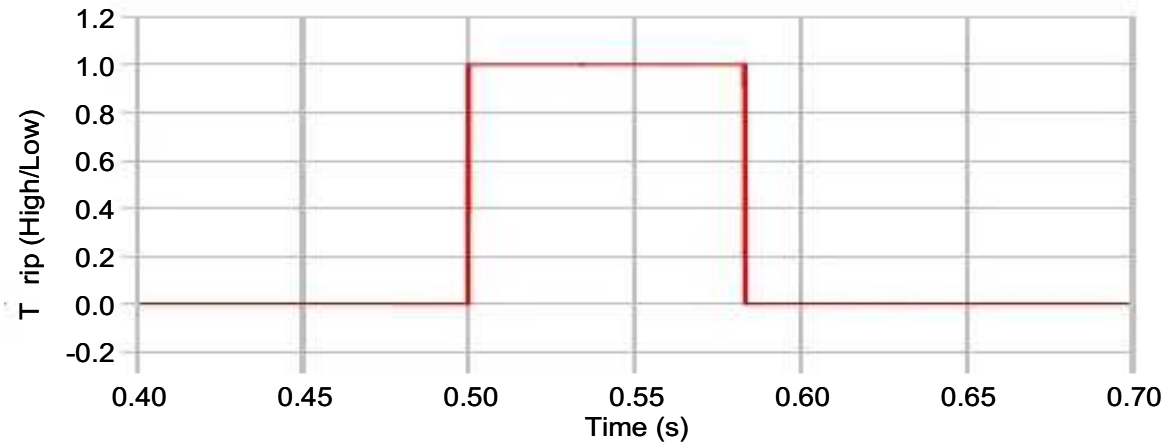

Fig. 1.1. Trip signal from circuit protection

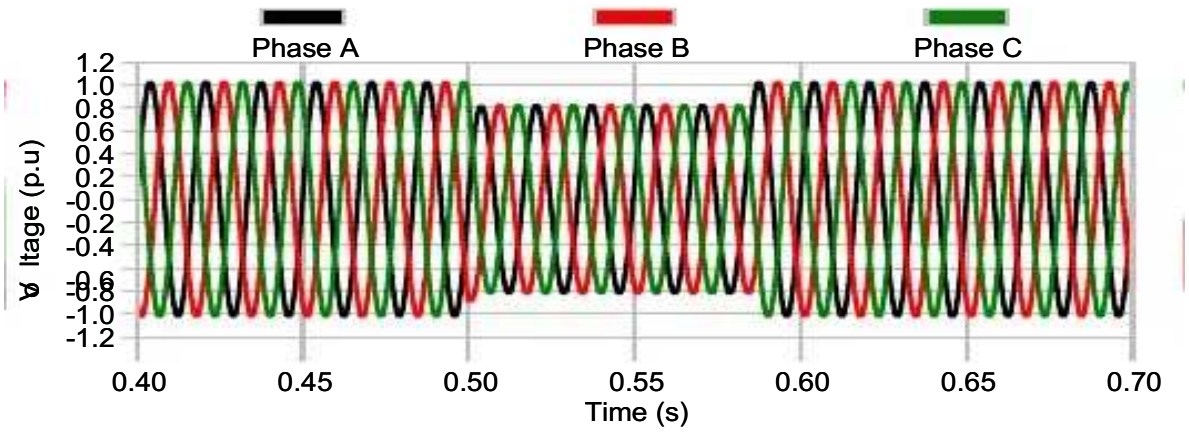

Fig. 1.2. Phase to ground voltages at the sensitive load

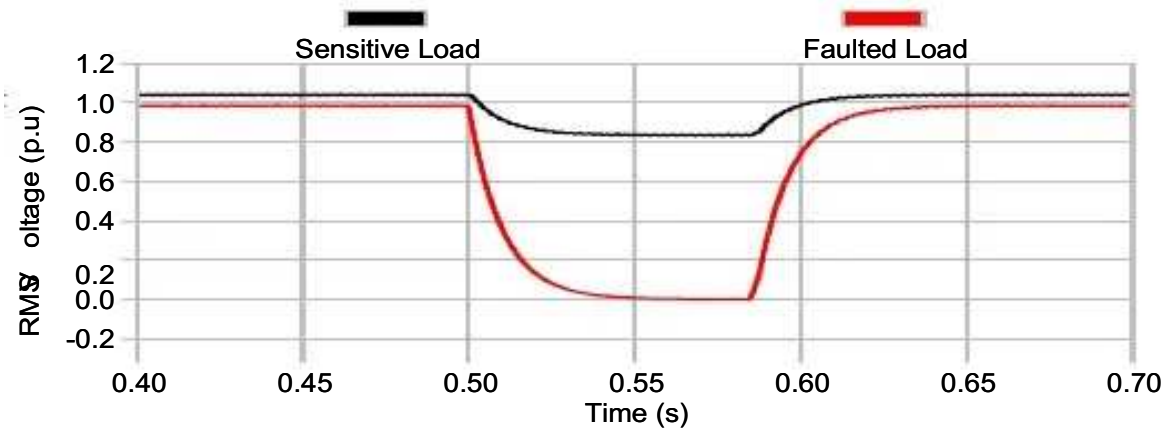

Fig. 1.3. RMS voltages at the sensitive load and faulted load

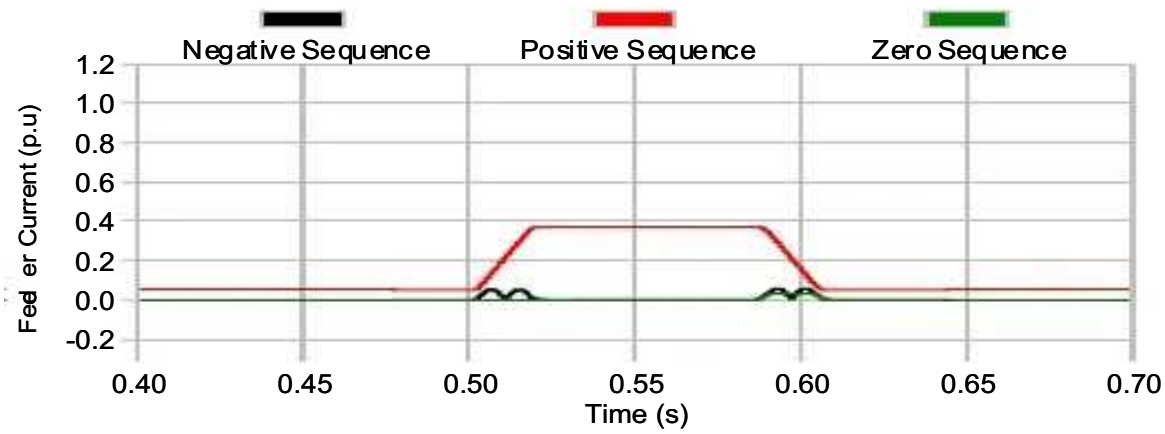

Fig. 1.4. Sequence currents from the feeder

The following waveforms use a weak source with the same three-phase fault applied at the distant load terminals. Fig. 1.5 shows a balanced voltage sag of 65% at the sensitive load due to this fault. With a weak source, the sensitive load is more affected than with a strong source due to increased voltage drop across the source impedance. Fig. 1.6 shows the RMS voltage measured at the sensitive load and at the distant load. Fig. 1.7 shows that the positive sequence current is reduced with the weaker source due to the increased source impedance.

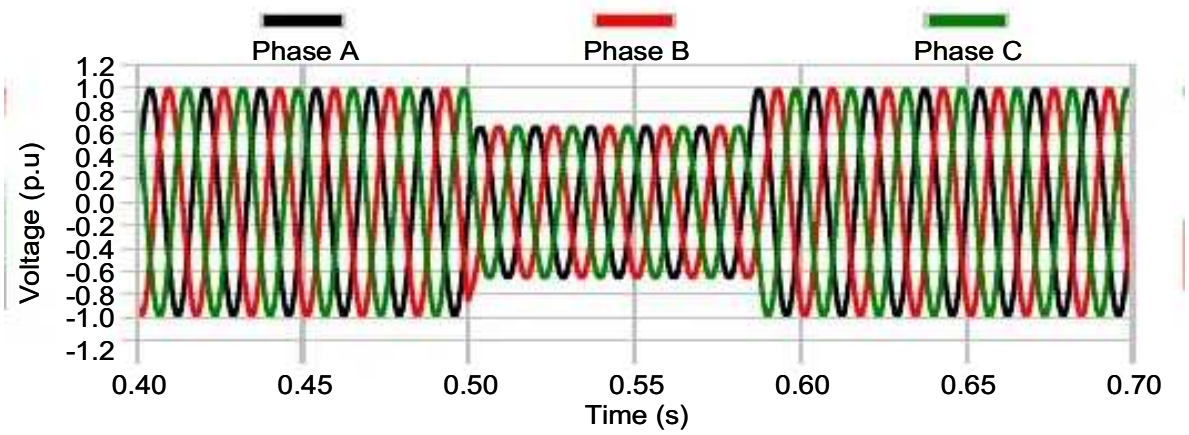

Fig. 1.5. Phase to ground voltages at the sensitive load

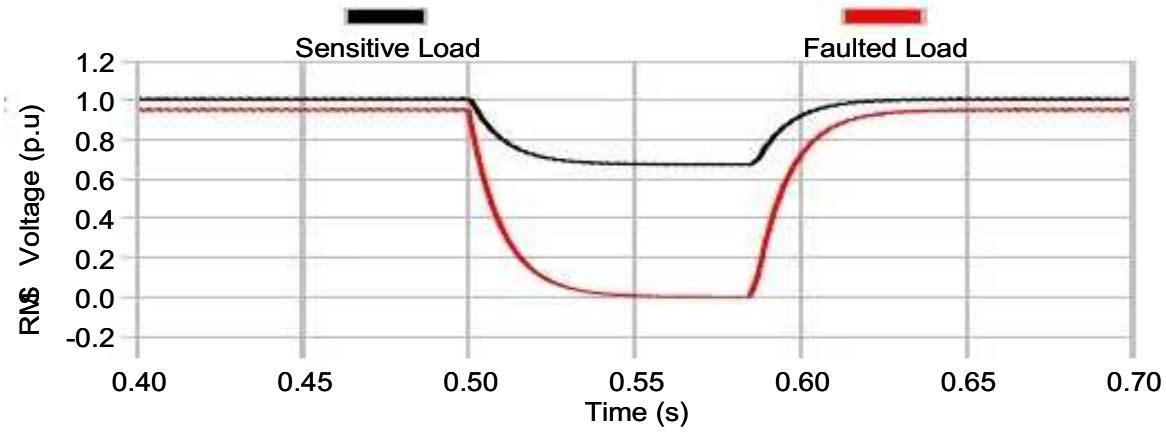

Fig. 1.6. RMS voltages at the sensitive load and faulted load

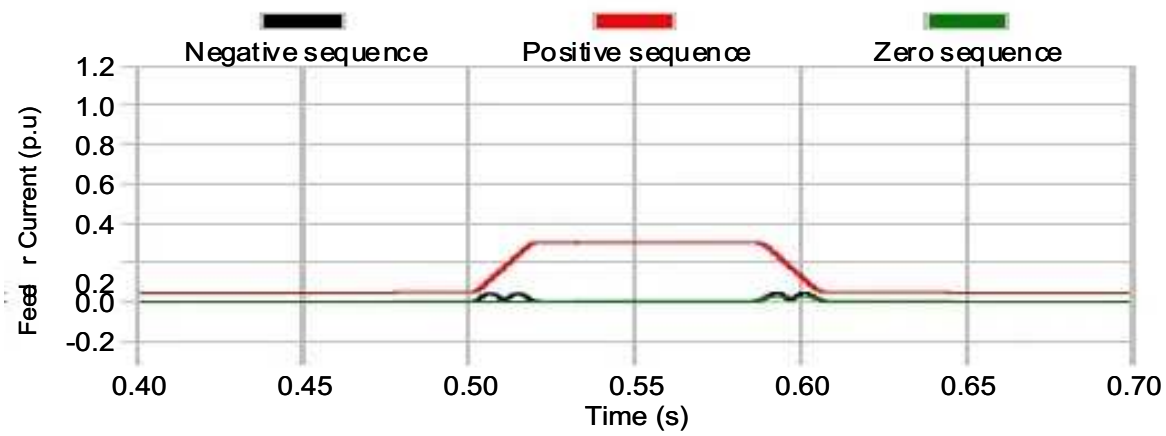

Fig. 1.7. Sequence currents from the feeder

The following cases again use with a weak source, but now a three-phase fault is applied at the middle of the transmission line. Fig. 1.8 shows a balanced voltage sag of 50% at the sensitive load due to this fault. The electrical distance from the sensitive load to the fault point determines the severity of the sag.

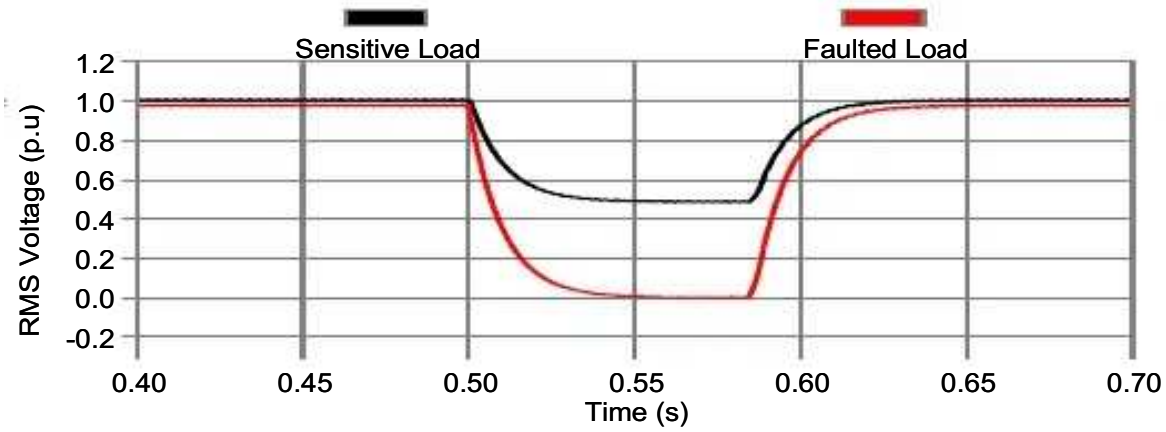

Fig. 1.8. Phase to ground voltages at the sensitive load

The following cases are with the same three-phase fault applied to an ungrounded system at the distant load. The source is weak as seen from the sensitive load. Fig. 1.9 shows the same balanced voltage sag of 65% as was seen with the grounded system, since a three phase fault doesn't involve ground. An overvoltage is seen at the end of transient due to the fault current interruption at the current zero crossing and redistribution of fault currents. Fig. 1.10 shows the RMS voltage measured at the sensitive load and at the distant load. Since it is a balanced fault, the negative sequence currents from the feeder are zero (except during the transient state as seen in Fig. 1.11). Since the system is ungrounded the zero sequence current is zero.

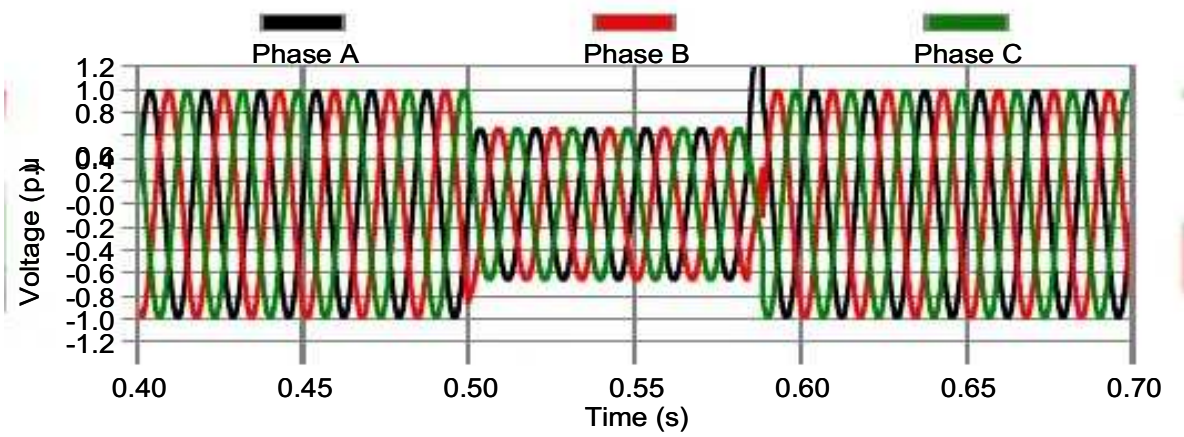

Fig. 1.9. Phase to ground voltages at the sensitive load

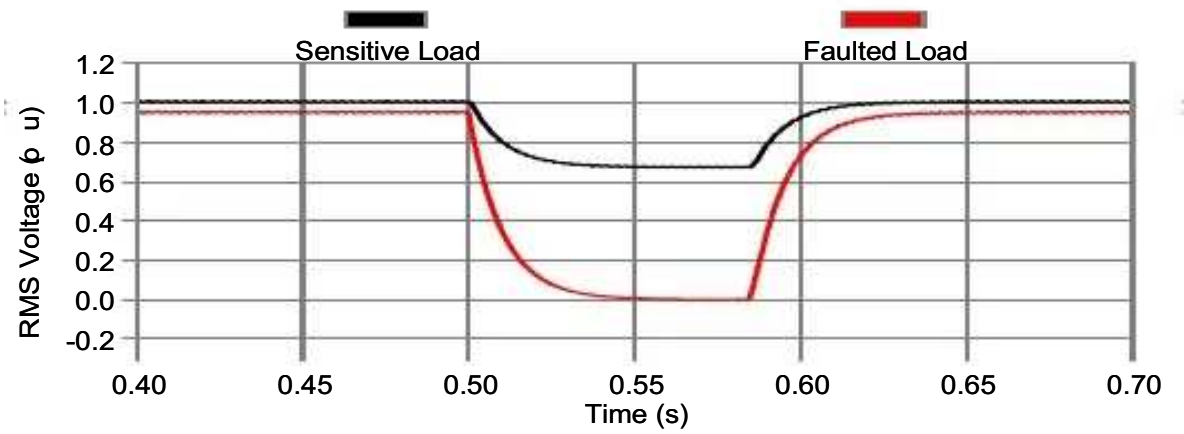

Fig. 1.10. RMS Voltages at the sensitive load and faulted load

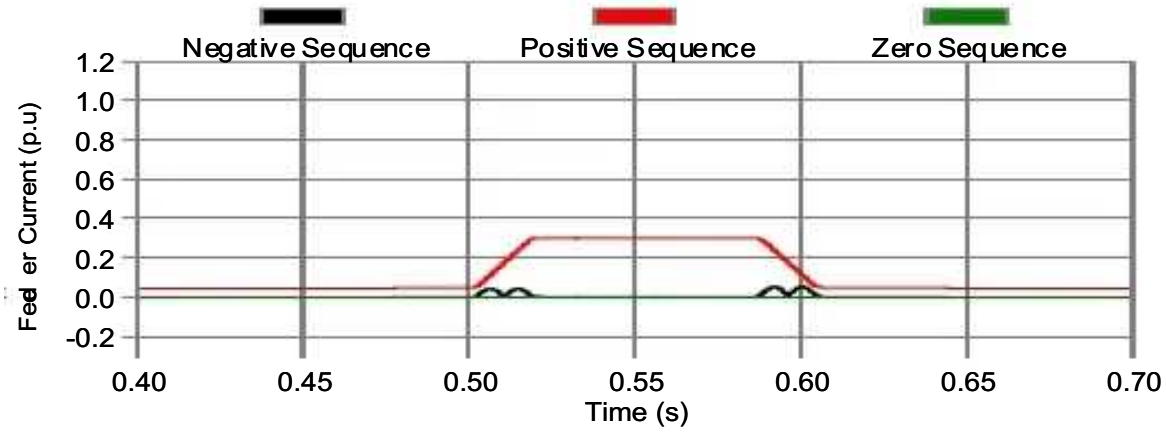

Fig. 1.11. Sequence currents from the feeder

The following cases use a solidly grounded system with a single-phase A to ground fault at the distant load. The source is weak as seen from the sensitive load. Fig. 1.12 shows an unbalanced voltage sag on phase A. The other two phases are unaffected since the system is solidly grounded. Fig. 1.13 shows a ripple in the RMS voltage measured at the sensitive load and at the distant load. The RMS voltage measurements used here involve averaging all the three phase voltages and assumes them to be balanced. The ripple depends on the smoothing constant of the filter used for RMS measurement. The negative and zero sequence currents distribution from the feeder during this fault is shown in Fig. 1.14.

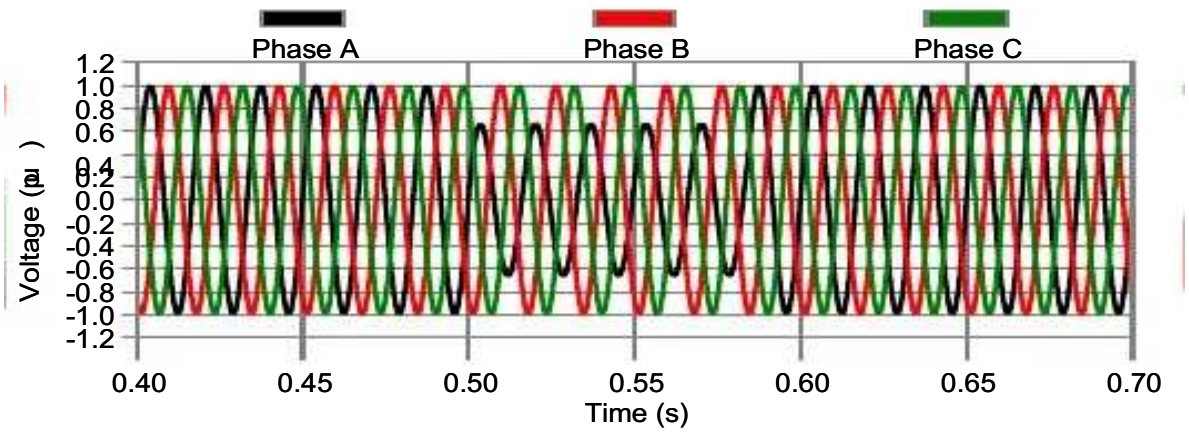

Fig. 1.12. Phase to ground voltages at the sensitive load

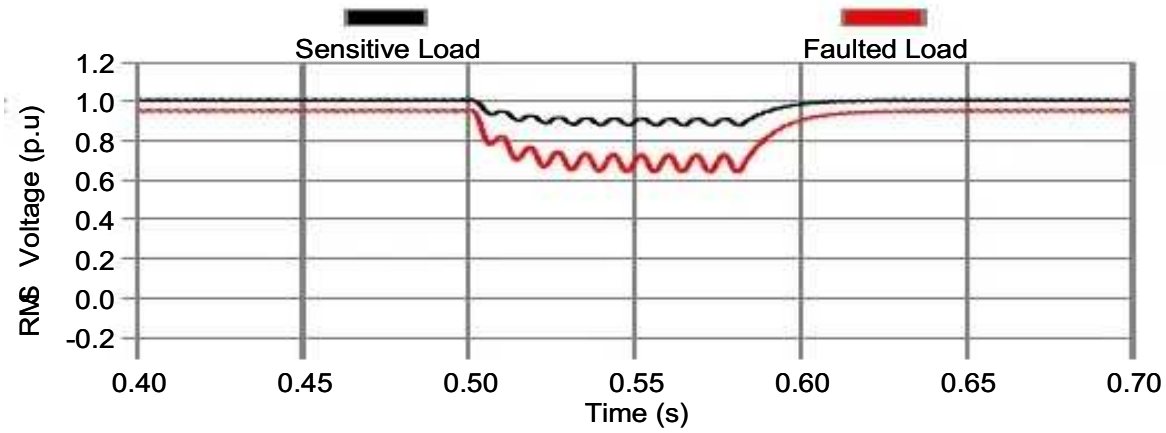

Fig. 1.13. RMS Voltages at the sensitive load and faulted load

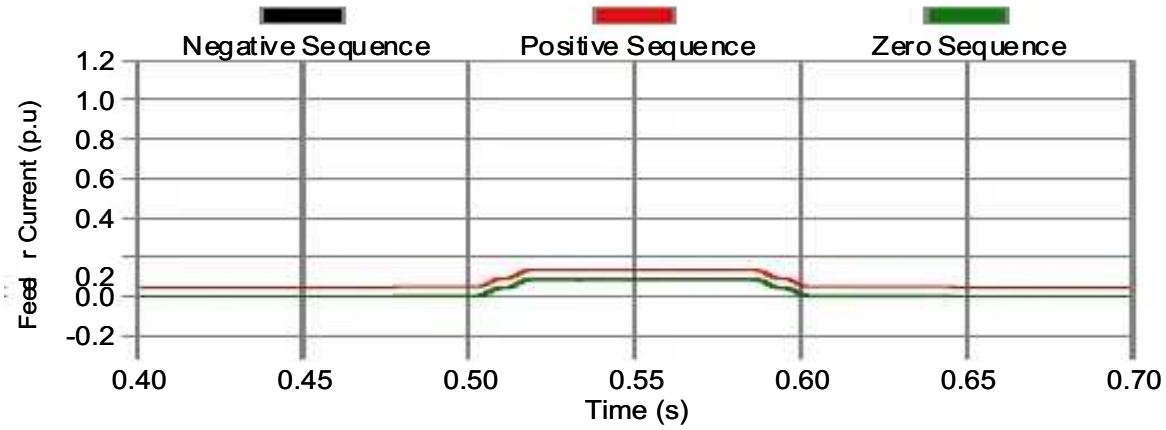

Fig. 1.14. Sequence currents from the feeder

The following waveforms apply the same single-phase fault to an ungrounded system at the distant load. The source is weak as seen from the sensitive load. Fig. 1.15 shows unbalanced voltages seen by the sensitive load. The phase A voltage goes to zero but the voltages on the other two phases swell by 1.732 times the rated. For a single phase to ground fault there is no path in the circuit for the zero sequence current to flow, resulting in a shift of the neutral point to faulted potential. In some cases the transients can increase this further. Fig 1.16 shows the RMS voltage measured at the sensitive load and at the distant load. No sag is seen, as it is a phase-to-phase voltage measurement. As a result, the loads in an ungrounded system are connected phase to phase to maintain continuity of service during single line to ground faults. Fig. 1.17 shows the zero sequence current magnitude to be zero. In real systems, very small zero sequence currents flow through the parasitic capacitances, limiting the swell somewhat less than 1.732 per unit.

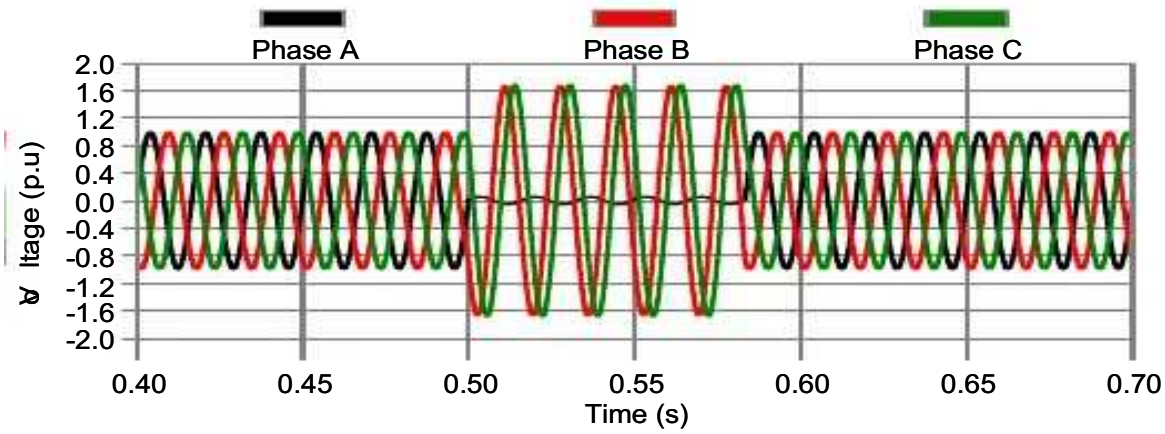

Fig. 1.15. Phase to ground voltages at the sensitive load

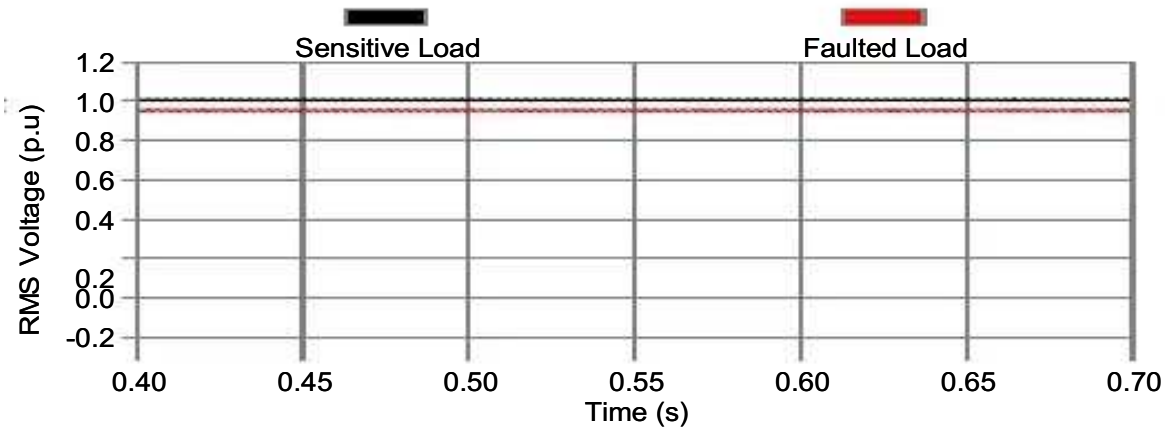

Fig. 1.16. RMS voltages at the sensitive load and faulted load

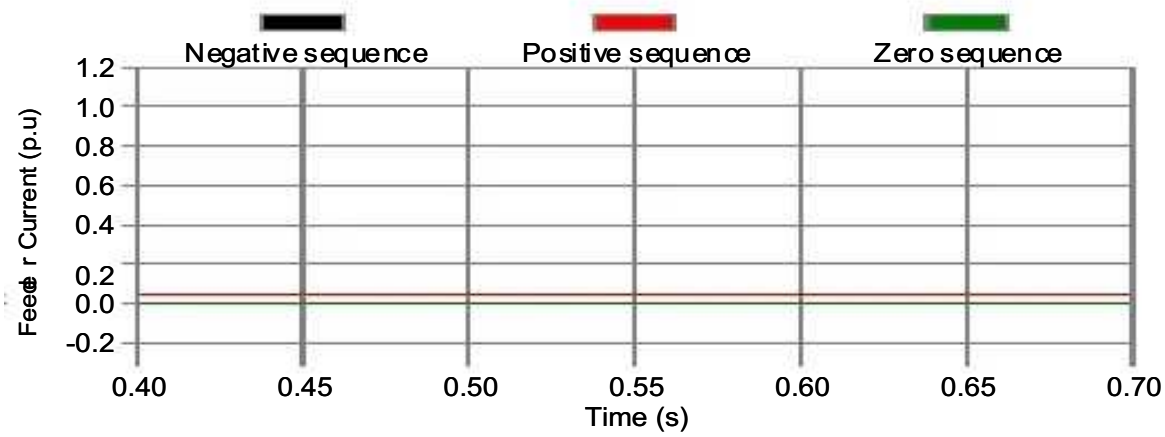

Fig. 1.17. Sequence currents from the feeder

1.4. Energy Storage and Topologies

This section discusses different energy storage technologies available for this project and the reason for using flywheel energy storage.

1.4.1 Available energy storage technologies

Energy can neither be created nor destroyed. But it can be transformed from one form to another. Electrical energy is the form of energy that can be transmitted efficiently and easily transformed to other forms of energy. The main disadvantages with electrical energy involve storing it economically and efficiently. Electrical energy can be converted and stored in different forms:

- Electrochemical Energy
- Electrostatic Energy
- Electromagnetic Energy
- Electromechanical Energy

1.4.1.1 Electrochemical energy storage

In this type of storage, electrical energy is converted and stored in the form of chemical energy. There are two main categories: batteries and fuel cells [2]. Batteries use internal chemical components for energy conversion and storage whereas fuel cells use synthetic fuel (for example Hydrogen, methanol or hydrazine) supplied and stored externally. Both use two electrodes, an anode and a cathode, that exchange ions through an electrolyte internally and exchange electrons through an electric circuit externally. The Lead-acid battery, discovered by Plante in 1859, is the most widely used battery. The battery consists of pairs of lead electrode plates immersed in a dilute sulphuric acid that acts as an electrolyte. Every alternate lead plate is coated with lead dioxide. Discharging results in the conversion of both of the electrodes to lead sulphate. Charging restores the plates to lead and lead dioxide. The physical changes in electrodes during charging and discharging deteriorates the

electrodes and hence reducing their life. The main advantages are they have a well-established technology. The main drawbacks with batteries are:

- Slow response during energy release
- Limited number of charge discharge cycles
- Relatively short life time
- High internal resistance
- Low energy density
- Maintenance requirements for some types
- Environmental hazards

W. R. Grove demonstrated the first hydrogen-oxygen fuel cell in 1839. The byproduct of a Hydrogen fuel cell is water. By electrochemical decomposition of water into hydrogen and oxygen and holding them apart, hydrogen fuel cells store electrical energy. During discharge, the hydrogen is combined with oxygen, converting the chemical energy to electrical energy. The main advantages are environment friendly. The main drawbacks with fuel cells as energy storage elements are:

- Slow response during energy release
- Temperature dependence
- Corrosion problems
- Hydrogen storage
- Ineficient transfer of electrical energy to chemical energy

1.4.1.2 Electrostatic energy storage

Electric energy can be converted and stored in the form of electrostatic field between the parallel plates of a charged capacitor. The amount of energy stored is proportional to square of the voltage across the parallel plates and to its capacitance. For a fixed voltage, the volume energy density for a parallel plate capacitor is proportional to capacitance, which is proportional to the permittivity of the insulator between the parallel plates. Most of the insulators have relative permittivity in the range of 1 to 10. Due to the small capacitance, ordinary capacitors can store very limited amount of energy. Ultracapacitors use electrochemical material for improving permittivity and hence energy density. They require less maintenance and have much longer lifetimes compared to batteries. They have high energy density and does not having moving parts. The main drawbacks with capacitors are:

- Cost
- Temperature dependence
- Not rugged

1.4.1.3 Electromagnetic energy storage

Electric energy can be converted and stored in the form of an electromagnetic field.

A Superconducting magnetic energy storage (SMES) coil consists of a superconducting coil carrying large DC currents. The amount of energy stored is proportional to the square of the DC current flowing through the coil and to its inductance. The volume energy density is proportional to the permeability of the material used for the coil. In order to keep the temperature of the superconductor below its critical temperature, a cryogenic cooling system is required. Increasing the DC current increases the amount of energy stored. Once the current in the coil reaches its maximum value, the voltage across it is zero and the SMES is fully charged. This storage scheme has very low losses due to negligible resistance in

the coil. Also SMES coils can be built for larger energy and power. The main drawbacks with SMES are:

- Cost
- Reliability in maintaining cryogenic cooling
- Compensation of external stray fields
- Electromagnetic forces on the conductors
- Bulk/volume

1.4.1.4 Electromechanical energy storage

Electrical energy can be converted and stored in the form of kinetic energy in a flywheel. Motor/generator sets, DC machines and induction machines are used for energy conversion. The amount of energy stored in a flywheel is proportional to the square of angular velocity and to its inertia for a given design stress.

The energy storage technologies discussed above have their own advantages and disadvantages but the following advantages make flywheels a viable alternative to other energy storage systems:

- Low cost
- High power density
- Ruggedness
- Greater number of charge discharge cycles
- Longer life
- Less maintenance
- Environmental friendly
- Fast response during energy release

Flywheels can be designed for low speed or high-speed operation. A low speed flywheel has advantages of lower cost and the use of proven technologies when compared to a high-speed flywheel system.

The main disadvantages are:

- less energy stored per volume
- higher losses
- increased volume and mass

1.5 Problem Statement and Proposed Solution

A shipboard power system is a stiff, isolated power system. Power is generated locally and distributed over short distances. As a result, any system transients impact the entire system. Critical loads such as computers, radar systems, water pumps and weapon systems play an important role in the survival of a combat ship during battle conditions. Power quality problems, such as voltage sags [4], which arise due to a fault or a pulsed load, can cause interruptions of critical loads. These interruptions can be a serious concern for the survivability of a combat ship. The US Navy is looking for methods to maximize the survivability of its combat ship [5]. An effective way to mitigate voltage sags is by the use of series voltage compensation with energy storage [6]. Series voltage compensation provides the flexibility to inject voltage at any angle with energy storage.

A low speed flywheel coupled to an induction machine is the option explored in this thesis. The induction machine is used for bi-directional transfer of energy to the flywheel. A voltage-sourced converter is used to interface the induction machine with the energy storage system. Indirect field oriented control with space vector PWM is used to control the induction machine.

A voltage source converter-based static series compensator is interfaced with the SPS for voltage sag correction. Sinusoidal PWM is used for controlling the static series compensator. The two voltage sourced converters share a common DC link. The power electronic interface is used for the bi-directional flow of energy for charging and discharging the flywheel through the induction machine with DC link as medium. An outer control system detects voltage sag and controls the energy flow during sag correction. An inner control system is used to generate gate pulses for each converter.

This thesis presents the modeling, simulation and analysis of a flywheel energy storage system (FESS) based static series compensator for voltage sag correction. The basic circuit and operation is explained in Chapter 2. Modeling was done using PSCAD/EMTDC [7] and MATLAB as is explained in Chapters 3, 4 and 5. The control system for sag detection, sag correction and energy flow is presented in

Chapter 6. The simulated performance of the flywheel energy storage system in mitigating balanced voltage sag is analyzed in Chapter 7.

The future work will include a detailed analysis of a flywheel energy storage system for unbalanced voltage sags and validating the simulation model with a laboratory flywheel interfaced to an analog model power system.

2.0 BASIC CIRCUIT AND OPERATION

The basic circuit consists of an energy storage system, power electronic interface and a series transformer as shown in Fig. 2.1. The energy storage system in this case is a flywheel coupled to an induction machine. The induction machine is used for energy conversion. The power electronic interface consists of two voltage-sourced converters connected through a common DC link. One voltage source converter interfaces with the energy conversion and storage system and the other with the shipboard power system.

The flywheel energy storage system has three modes of operation:

- Charge mode
- Stand-by mode
- Discharge mode

During charge mode, the VSC interfacing the shipboard power system runs as a rectifier and the other as an inverter, with the transferred energy accelerating the flywheel to its rated speed. In this mode, energy is stored in the flywheel in the form of kinetic energy. The energy flow is from shipboard power system to flywheel with induction machine as energy converter.

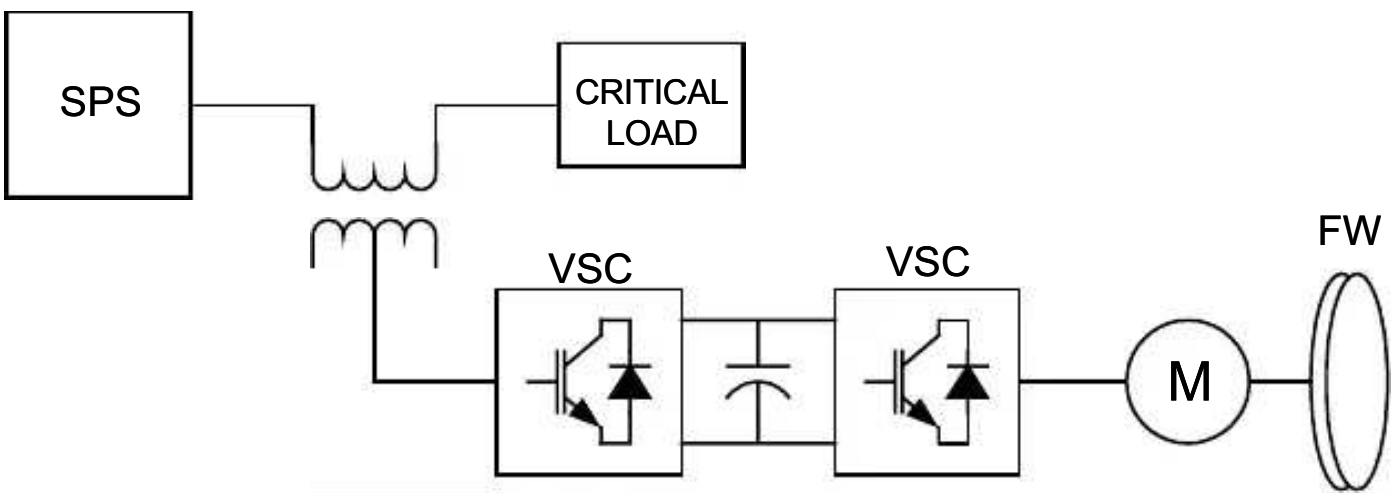

Fig. 2.1. Basic circuit of flywheel energy storage system

Once the flywheel reaches its charge speed, the storage system is in stand-by mode and is ready to discharge when the critical load sees a voltage sag. In this mode a little energy from the shipboard power system is used for meeting the converter and machine losses.

During discharge mode, the VSC interfacing the shipboard power system runs as an inverter injecting the required voltage in series with the line to correct the voltage sag. The flywheel VSC runs as a rectifier. The flywheel slows as it discharges. In this mode, the stored energy is used for sag correction and energy flow is from the flywheel to shipboard power system.

Fig. 2.2 shows a simplified diagram that shows the series connection of flywheel energy storage system.

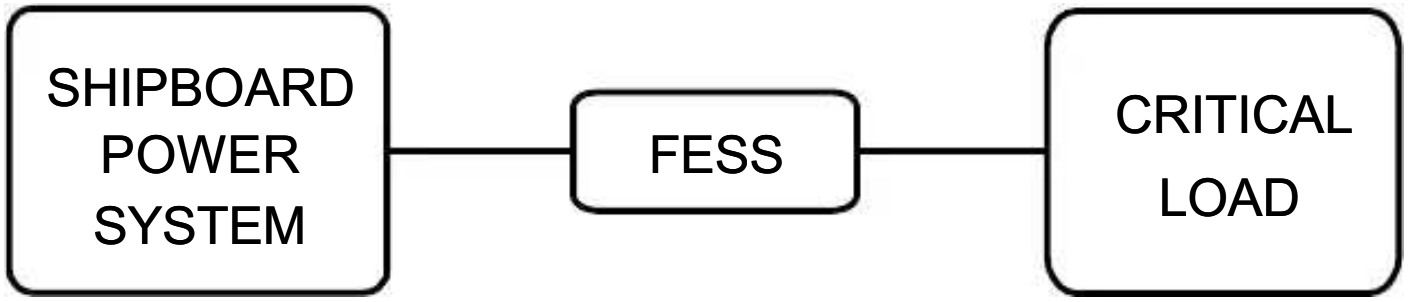

Fig. 2.2. Basic diagram showing series connection

3.0 MODELING STRATEGY

The flywheel energy storage system was modeled using PSCAD/EMTDC [7] with an interface to MATLAB. This section gives an introduction to the software and modeling strategy adopted to simplify the complexity involved in modeling the flywheel energy storage system.

3.1 Software background

Power system simulation involves solving a set of complex time dependent equations. PSCAD/EMTDC was developed by Manitoba HVDC Research center in the early 90's. EMTDC is a transient simulator that can model power system components, complex power electronic devices and controls whereas PSCAD is a graphical user interface for visualizing the complex behavior of power system. PSCAD/EMTDC is a powerful tool for simulating electromagnetic transients of electrical systems. The PSCAD graphical user interface enhances the power of EMTDC. A user can draw the circuit, run the simulation, and capture the results in a completely graphical environment. A master library is available consisting all the basic power system components such as resistors, capacitors, inductors, power electronic devices, transformers, transmission lines and machines.

EMTDC uses interpolation with an instantaneous switch algorithm to give accurate simulation results for power electronic simulations with larger time steps. New components can be designed using a graphical component design tool. With the proper FORTRAN compiler, EMTDC can interface with MATLAB. This is very useful in simulations which involve complicated control algorithms.

3.2 Module breakup

A Flywheel energy storage system consists of the following components that need to be modeled in PSCAD/EMTDC:

- Shipboard power system
- Two voltage sourced converters
- Induction machine
- Flywheel
- Firing schemes for the converters
- Control system

Fig. 3.1 shows a single line diagram of a flywheel energy storage system. To simplify modeling and testing, it is broken into two sub models. Each sub model is separately modeled, tested and integrated to make it a complete model. The sub models are:

- Field oriented control AC drive model
- Static series compensator model

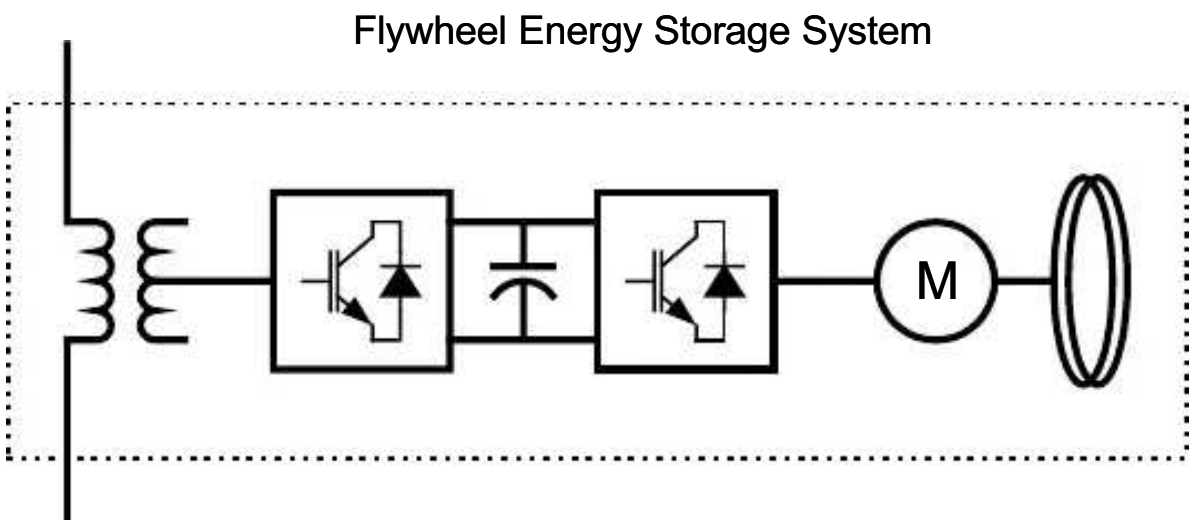

Fig. 3.1. Single line diagram of a flywheel energy storage system

3.2.1 Field oriented control AC drive model

Fig. 3.2 shows the outline of the field oriented control AC drive that was modeled in EMTDC. It has the following sub models:

- Full transient induction machine model
- Indirect field oriented controller model
- Space vector PWM pulse generator model
- Self commutated voltage sourced converter

The induction machine model available in PSCAD/EMTDC library is a steady state model. In order to study the behavior of energy storage system, a full transient induction machine model (a new component built in EMTDC as part of the thesis) was used. An indirect field oriented controller was modeled for controlling the induction machine. A space vector PWM pulse generator was modeled for controlling the gate pulses of machine side voltage sourced converter. The modeling procedure is explained in more detail in Chapter 4. The space vector PWM generator model uses the MATLAB interface for computing the switching times for the converter.

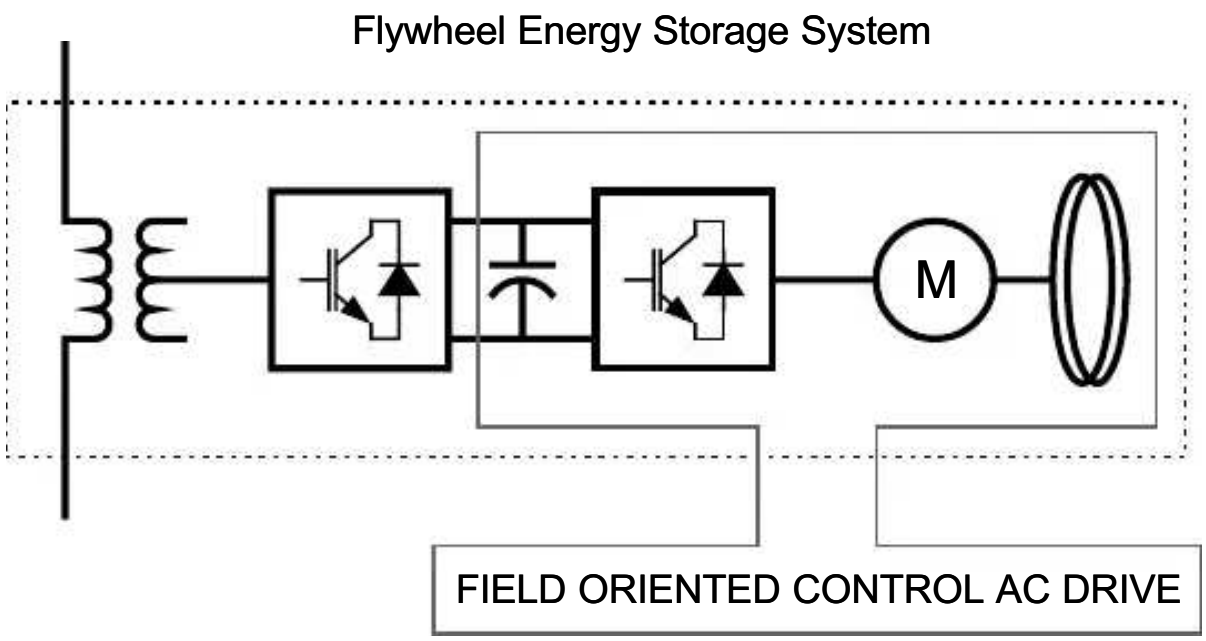

Fig. 3.2. Field oriented control AC drive model breakup

3.2.2 Static series compensator model

Fig. 3.3 shows the outline of a static series compensator as it was modeled in EMTDC. It has the following sub models:

- Shipboard power system model
- Series transformer and filters
- Sinusoidal PWM pulse generator model
- Self commutated voltage sourced converter

A sinusoidal PWM pulse generator was modeled for controlling the gate pulses to the shipboard power system side voltage sourced converter. The Shipboard power system was modeled as a simple radial system. The modeling procedure is explained in Chapter 5.

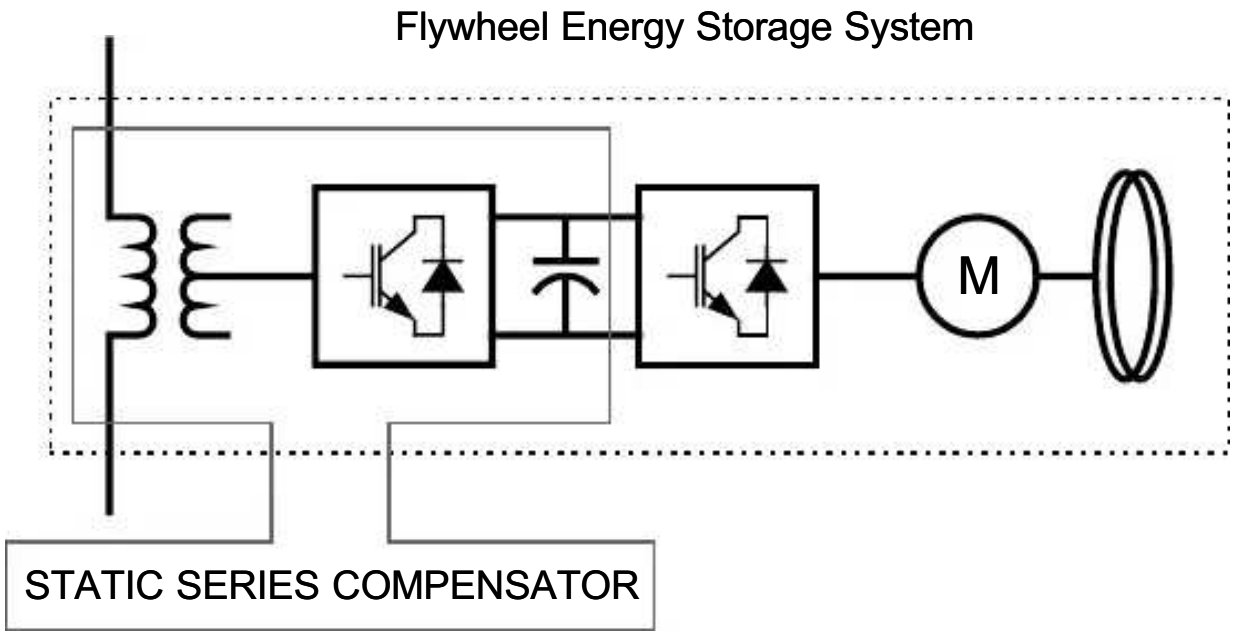

Fig. 3.3. Static series compensator model breakup

3.2.3 Control system

The control system was modeled in EMTDC. It has the following sub models:

- Sag detector
- Sag corrector
- Energy control system

The modeling procedure is explained in Chapter 6.

The field oriented control AC drive model and static series compensator share a common DC link. Initially static series compensator was modeled separately by replacing the field oriented control AC drive with an equivalent current source. Similarly field oriented control AC drive was initially modeled by replacing static series compensator with an equivalent voltage source. Then they were integrated to make a complete FESS model with control system.

4.0 FIELD ORIENTED CONTROL AC DRIVE MODEL

The field oriented control AC drive consists of the following custom models built in the DQ domain:

- Full transient induction machine model
- Indirect field oriented controller model
- Space vector PWM pulse generator
- Self commutated voltage sourced converter

The following sections describe how these custom models were built and how they are integrated to make a field oriented control AC drive model.

4.1 Machine modeling

An induction machine can be seen as a transformer with a moving secondary where the mutual inductances change continuously with the rotor position [8]. An induction machine modeled in abc reference frame is complex, consisting of six differential equations with time varying mutual inductances (see Appendix A Section 10.1). The inherent complexity in dealing with the induction machine voltage equations resulting from the time varying mutual inductances between stator and rotor circuits led to the concept of using alternative reference frames.

A complex space vector is defined as $S_s=(2/3)(S_A+\underline{a}S_B+\underline{a}^2S_C)$ where S_A, S_B and S_C are three phase instantaneous machine variables such as voltage, current or flux and $\underline{a}$ is a 120^0 phase shift operator [9]. The space vector can be projected onto a set of direct and quadrature axes, with quadrature axis fixed along the axis of the A phase stator winding. For motor convention, the direct axis lags the quadrature axis by 90^0. As a result, an ungrounded three phase induction machine can be represented as a two phase induction machine as shown in Fig 4.1, where d^s - q^s correspond to stator direct and quadrature axes, and $d^r - q^r$ correspond to rotor

direct and quadrature axes. This projection reduces the number of voltage equations to four but time varying inductances still remain.

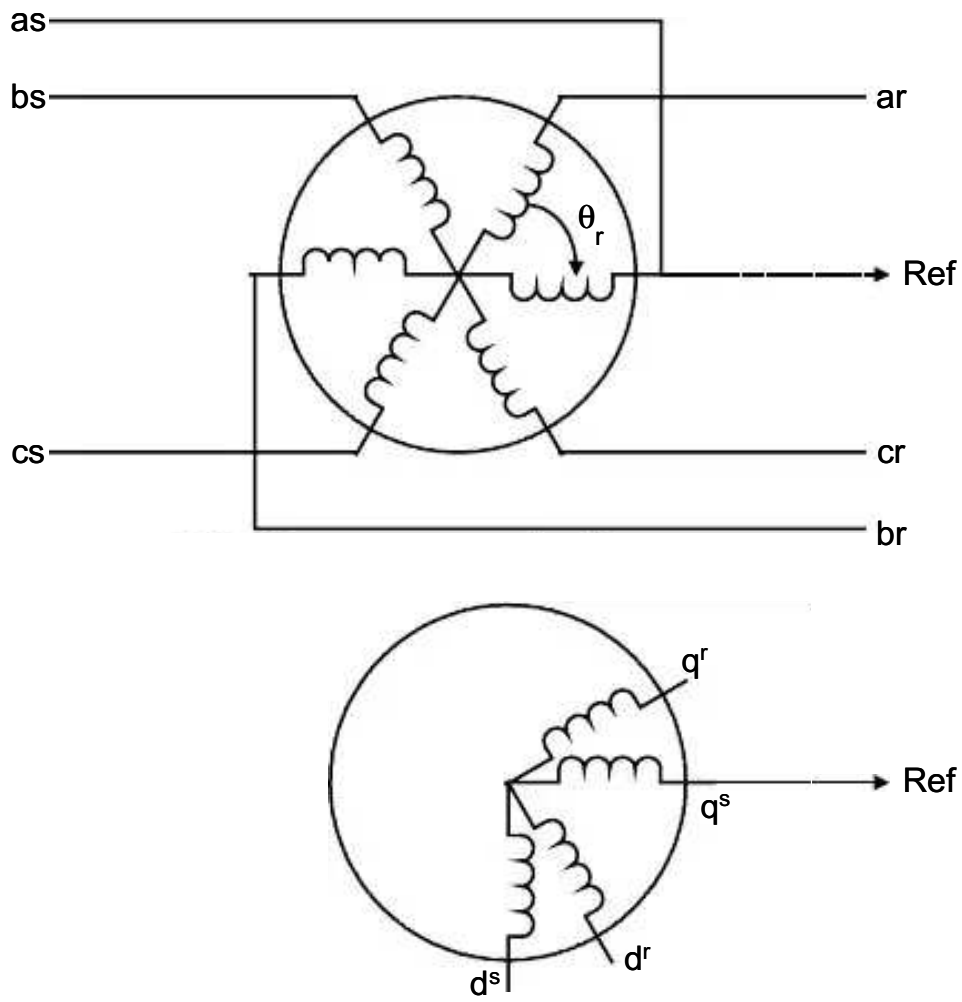

Fig. 4.1. Two phase equivalent representation of induction machine

G. Kron proposed a transformation that eliminates time variant inductances by projecting the stator and rotor variables onto a synchronously rotating reference frame (with the quadrature axis fixed in synchronism with the rotating magnetic field). Later Krause and Thomas generalized Kron transformation to show that the time varying inductances can always be removed by projecting the stator and rotor variables onto a common rotating reference frame which is not necessarily at synchronous speed. The common reference frame can also be non-rotating in which case it is fixed in the stator and is called stationary reference frame. This change of variables decreases the complexity in modeling and control of a three phase symmetrical induction machine.

4.1.1 d-q axes transformation

Fig. 4.2 shows a symmetrical induction machine with stationary as-bs-cs axes, 120^0 apart where s implies a stator quantity. The three phase stationary reference variables (as-bs-cs) are transformed to a two phase synchronously rotating reference frame ($d^e - q^e$) variables in two steps. The first step is to transform the three phase variables to a two phase stationary reference variables ($d^s - q^s$) and the second step is to transform the two phase stationary variables to a two phase synchronously rotating reference frame variables.

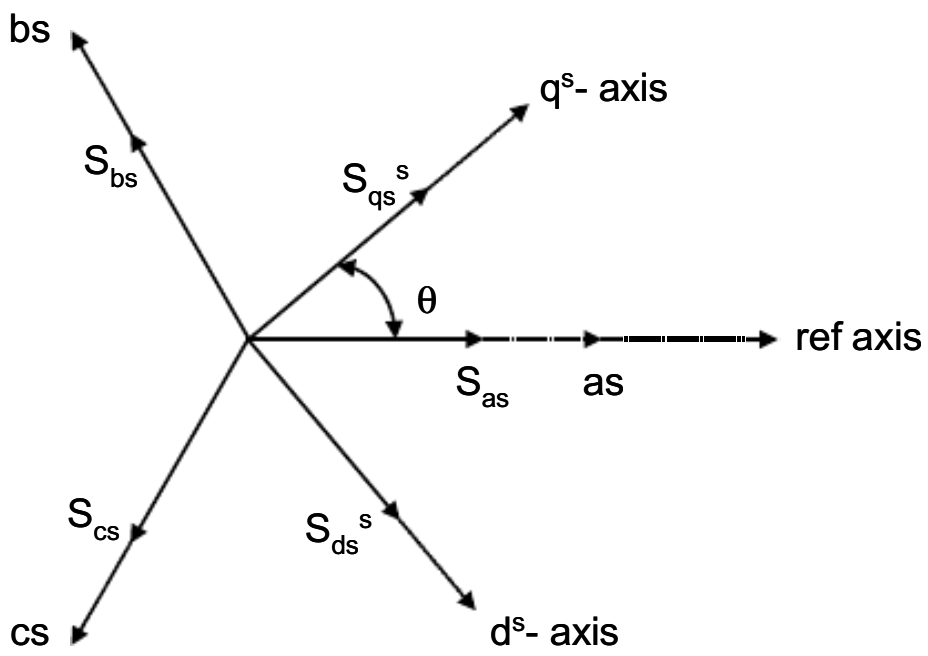

Fig. 4.2. Three phase to two phase stationary transformation

A matrix representation for converting three phase variables to two phase stationary variables is given by:

$$\begin{pmatrix} S_{qs}{}^s \\ S_{ds}{}^s \\ S_{0s}{}^s \end{pmatrix} = \frac{2}{3} \cdot \begin{pmatrix} \cos(\theta) & \cos(\theta - 120^o) & \cos(\theta + 120^o) \\ \sin(\theta) & \sin(\theta - 120^o) & \sin(\theta + 120^o) \\ 0.5 & 0.5 & 0.5 \end{pmatrix} \cdot \begin{pmatrix} S_{as} \\ S_{bs} \\ S_{cs} \end{pmatrix} \quad (4.1)$$

where θ is the orientation angle of d^s – q^s axes relative to reference axis (Phase A's).

$S_{0s}{}^s$ is a zero sequence component, which is always zero in the case of a balanced induction machine with no neutral connection. For convenience, the q^s axis is fixed along the as axis to make θ equal zero. So the transformation relations simplify to:

$$S_{qs}{}^s = \frac{2}{3}\cdot S_{as} - \frac{1}{3}\cdot S_{bs} - \frac{1}{3}\cdot S_{cs} = S_{as} \tag{4.2}$$

$$S_{ds}{}^s = -\frac{1}{\sqrt{3}}\cdot S_{bs} + \frac{1}{\sqrt{3}}\cdot S_{cs} \tag{4.3}$$

Inversely, the relation for converting two phase stationary variables to three phase variables is given by:

$$S_{as} = S_{qs}{}^s \tag{4.4}$$

$$S_{bs} = -\frac{1}{2}\cdot S_{qs}{}^s - \frac{\sqrt{3}}{2}\cdot S_{ds}{}^s \tag{4.5}$$

$$S_{cs} = -\frac{1}{2}\cdot S_{qs}{}^s + \frac{\sqrt{3}}{2}\cdot S_{ds}{}^s \tag{4.6}$$

Fig. 4.3 shows a synchronously rotating d^e – q^e axes at synchronous speed ω_e with respect to the d^s – q^s axes at an angle θ_e (angular reference for rotating magnetic field) where $\theta_e=\omega_e t$. The d^s - q^s variables can be converted to d^e – q^e variables as follows:

$$S_{qs} = S_{qs}^{s} \cdot \cos(\theta_e) - S_{ds}^{s} \cdot \sin(\theta_e) \tag{4.7}$$

$$S_{ds} = S_{qs}^{s} \cdot \sin(\theta_e) + S_{ds}^{s} \cdot \cos(\theta_e) \tag{4.8}$$

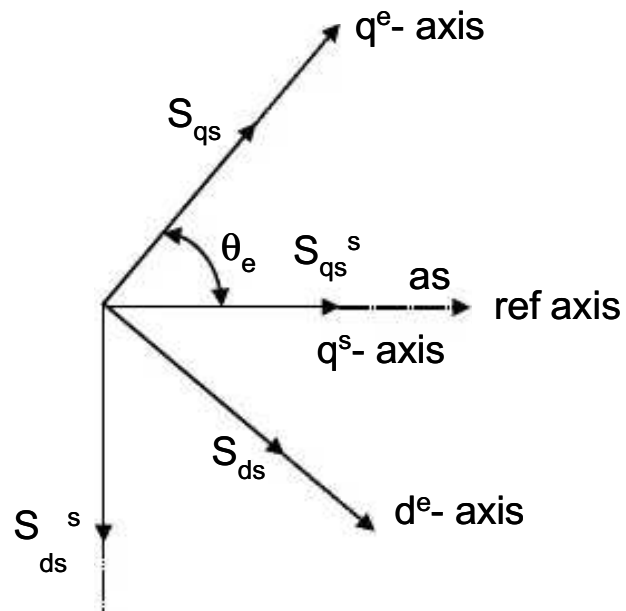

Fig. 4.3. Stationary to synchronous frame transformation

The prefix ‘e’ for representing as synchronous rotating reference variables has been omitted for simplified representation. Similarly a reverse transformation from the synchronous frame to stationary frame is given by:

$$S_{qs}^{s} = S_{qs} \cdot \cos(\theta_e) + S_{ds} \cdot \sin(\theta_e) \tag{4.9}$$

$$S_{ds}^{s} = -S_{qs} \cdot \sin(\theta_e) + S_{ds} \cdot \cos(\theta_e) \tag{4.10}$$

Consider the following example to demonstrate the main advantage of choosing the synchronous reference frame. Let us start with a three phase stator voltages given by:

$$v_{as}(t) = V_{pk}\cdot\cos\left(\omega_e\cdot t + \phi\right) \tag{4.11}$$

$$v_{bs}(t) = V_{pk}\cdot\cos\left(\omega_e\cdot t - \frac{2\cdot\pi}{3} + \phi\right) \tag{4.12}$$

$$v_{cs}(t) = V_{pk}\cdot\cos\left(\omega_e\cdot t + \frac{2\cdot\pi}{3} + \phi\right) \tag{4.13}$$

Substituting equations (4.11)-(4.13) in (4.2)-(4.3) and simplifying gives the stationary reference frame values:

$$v_{qs}^{s} = V_{pk}\cdot\cos\left(\omega_e\cdot t + \phi\right) \tag{4.14}$$

$$v_{ds}^{s} = -V_{pk}\cdot\sin\left(\omega_e\cdot t + \phi\right) \tag{4.15}$$

Substituting equations (4.14)-(4.15) in (4.7)-(4.8) and simplifying gives the synchronous reference frame values:

$$v_{qs} = V_{pk}\cdot\cos\left(\phi\right) \tag{4.16}$$

$$v_{ds} = -V_{pk}\cdot\sin\left(\phi\right) \tag{4.17}$$

Equations (4.16)-(4.17) are important results. The time varying quantities in stationary reference frame appear as DC quantities in synchronous reference frame. This makes the control system less difficult.

The stationary and synchronous reference stator voltage variables can be represented as complex space vectors as follows:

$$v_{qds}^{\ s} = v_{qs}^{\ s} - j \cdot v_{ds}^{\ s} \tag{4.18}$$

$$v_{qds} = \left(v_{qs}^{\ s} - j \cdot v_{ds}^{\ s} \right) \cdot e^{-j \cdot \theta_e} \tag{4.19}$$

Equation 4.19 is direct result obtained using eulers rule ($e^{j\theta}=\cos\theta+j\sin\theta$, where $j=\sqrt{-1}$ and $\theta=\theta_e=\omega_e t$).

4.1.2 Full transient induction machine model

The induction machine can be mathematically modeled in a synchronously rotating dq reference frame using the state space flux equations (4.20) – (4.24), where p is a derivative operator with respect to time (see Appendix A Sections 10.4 and 10.5 for the derivation of these equations).

$$p\cdot\lambda_{qds} = V_{qds} + \left(\lambda_{qds}\cdot L_r - \lambda_{qdr}\cdot L_m\right)\cdot\frac{R_s}{L_s\cdot L_r\cdot\sigma} - j\cdot\lambda_{qds}\cdot\omega_e \tag{4.20}$$

$$p\cdot\lambda_{qdr} = -\left[\left(\lambda_{qdr}\cdot L_s - \lambda_{qds}\cdot L_m\right)\cdot\frac{R_r}{L_s\cdot L_r\cdot\sigma}\right] - j\cdot\lambda_{qdr}\cdot\left(\omega_e - \omega_r\right) \tag{4.21}$$

$$i_{qds} = \left(\lambda_{qds} - \frac{L_m}{L_r}\cdot\lambda_{qdr}\right)\cdot\frac{1}{L_s\cdot\sigma} \tag{4.22}$$

$$T_e = \frac{3}{2}\cdot\left(\frac{P}{2}\right)\cdot\left(\lambda_{ds}\cdot i_{qs} - \lambda_{qs}\cdot i_{ds}\right) \tag{4.23}$$

$$p\cdot\omega_r = \frac{P}{2.J}\cdot\left(T_e - T_L\right) \tag{4.24}$$

The mathematical model, with V_{qds}, ω_e and T_L as inputs, calculates the currents (i_{qds}), rotor speed (ω_r) and electromagnetic torque (T_e) in the synchronous dq reference frame. The outputs are stator currents in synchronous reference frame, the rotor angular velocity and the electromagnetic torque. A built in dq to abc transformation component in EMTDC is used for converting the output stator currents to abc reference frame.

The induction machine appears as current source to the voltage sourced converter so the electrical model is represented as three dependent current sources driven by

the currents computed by the mathematical model. The voltages at the converter terminals are transformed to synchronous dq reference frame and are inputs to the mathematical model.

Figs. 4.4-4.7 shows the start up performance of the full transient induction machine model for a negative load torque (for simplicity the converter is initially replaced with a three phase voltage source). A negative torque of –11.74 N-m was applied to the induction machine model. Fig. 4.4 shows the full transient output synchronous dq reference frame stator currents. Fig. 4.5 shows the actual currents seen in the electrical model. Fig. 4.6 shows the electromagnetic torque output which settles to -11.74 N-m after 0.5 sec. Fig. 4.7 shows the rotor angular velocity variation in the transient and steady state period.

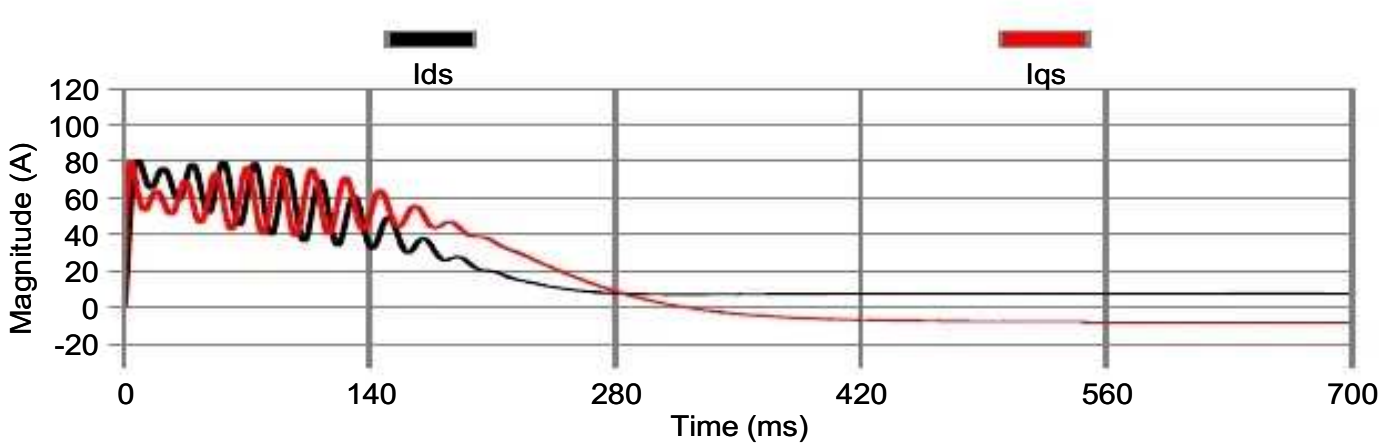

Fig. 4.4. Stator currents in synchronous reference frame

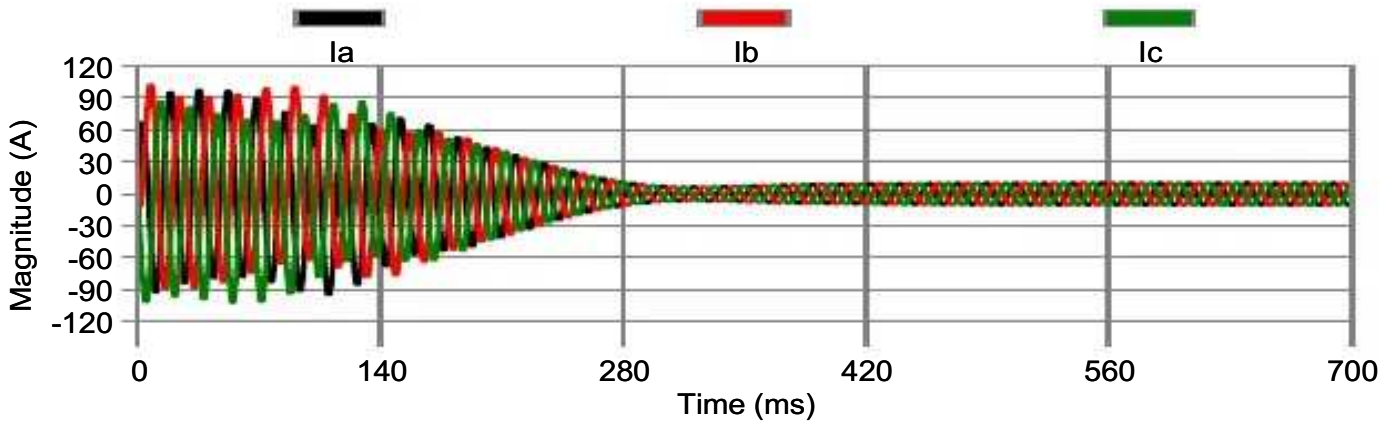

Fig. 4.5. Stator currents in as-bs-cs reference frame

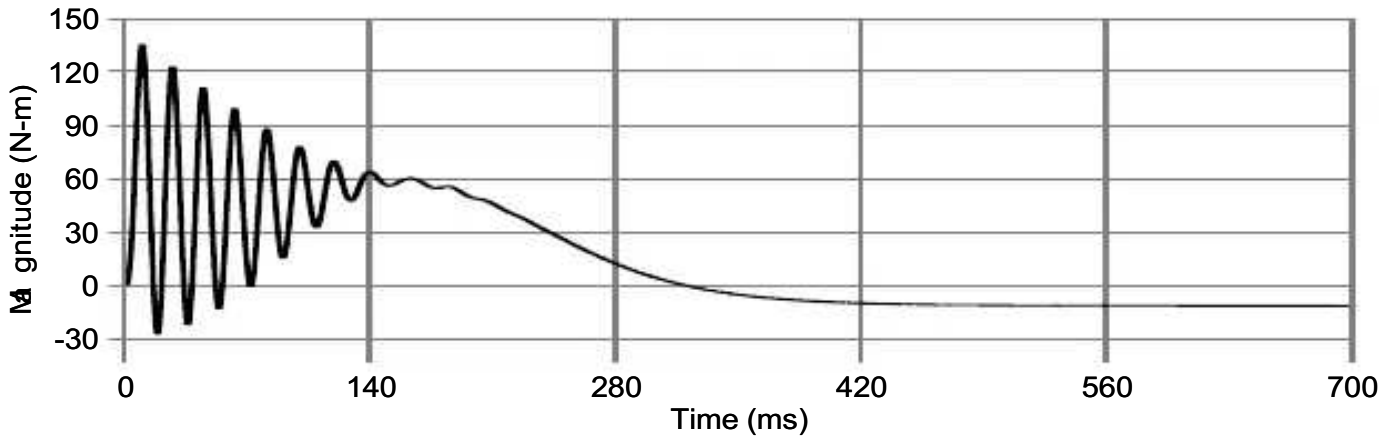

Fig. 4.6. Electromagnetic torque, T_e

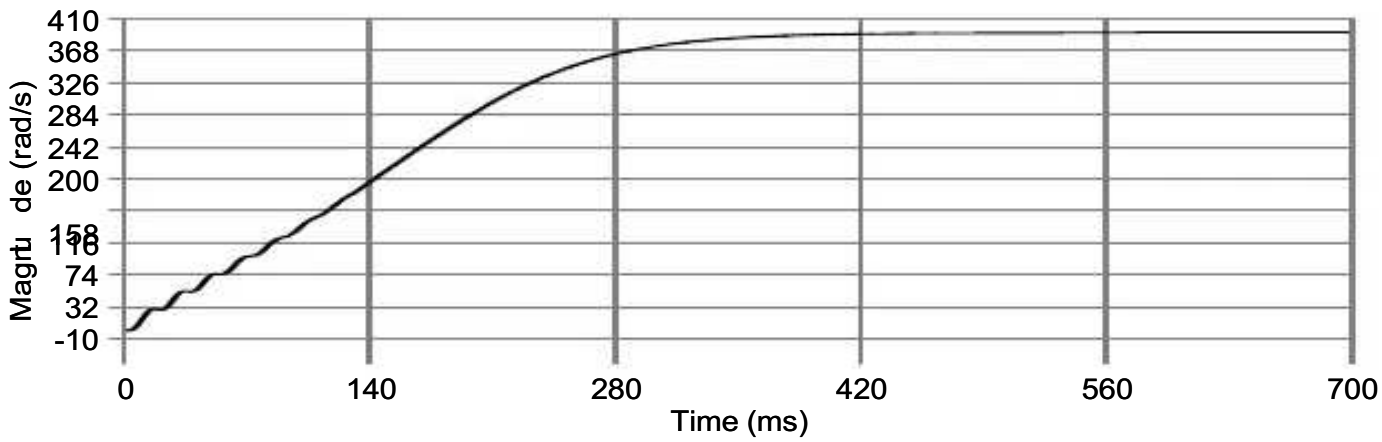

Fig. 4.7. Rotor angular velocity, ω_r

4.2 Field oriented controller

The control of the magnitude and phase of the AC excitation to the induction machine resulting in a controlled spatial orientation of the electromagnetic fields is termed as vector control or field oriented control [10]. The basic concept of field orientation is to align the rotor flux space vector along the d-axis so that the q-axis component of the flux is zero at all times. With this alignment, torque and flux of the machine can be controlled instantaneously and independently as in a separately excited DC machine. The rotor flux angle can be obtained either by directly computing it from the flux measurement using Hall effect sensors (called direct field oriented control) and the other by indirectly computing it from the measured rotor position and slip relation (called indirect field oriented control).

Indirect field orientation using voltage as control variable is modeled in EMTDC for this investigation (see Appendix A 10.4 for the EMTDC implementation). Fig. 4.8 shows the basic layout of the controller. The controller uses flux and torque commands as inputs with a compensated flux response for correctly handling flux variations. The torque command comes from the energy control system (see chapter 6). The flux is kept constant. The outputs, synchronous reference stator voltages and rotating magnetic field angular velocity, are input commands to space vector PWM pulse generator model.

The main disadvantage of the indirect field oriented controller is that it is sensitive to parameter variations, especially rotor resistance. This can be rectified by the use of flux observers [11]. In the future a flux observer will be added to make the field oriented controller more robust.

The flywheel is modeled as an added inertia on the rotor of the induction machine.

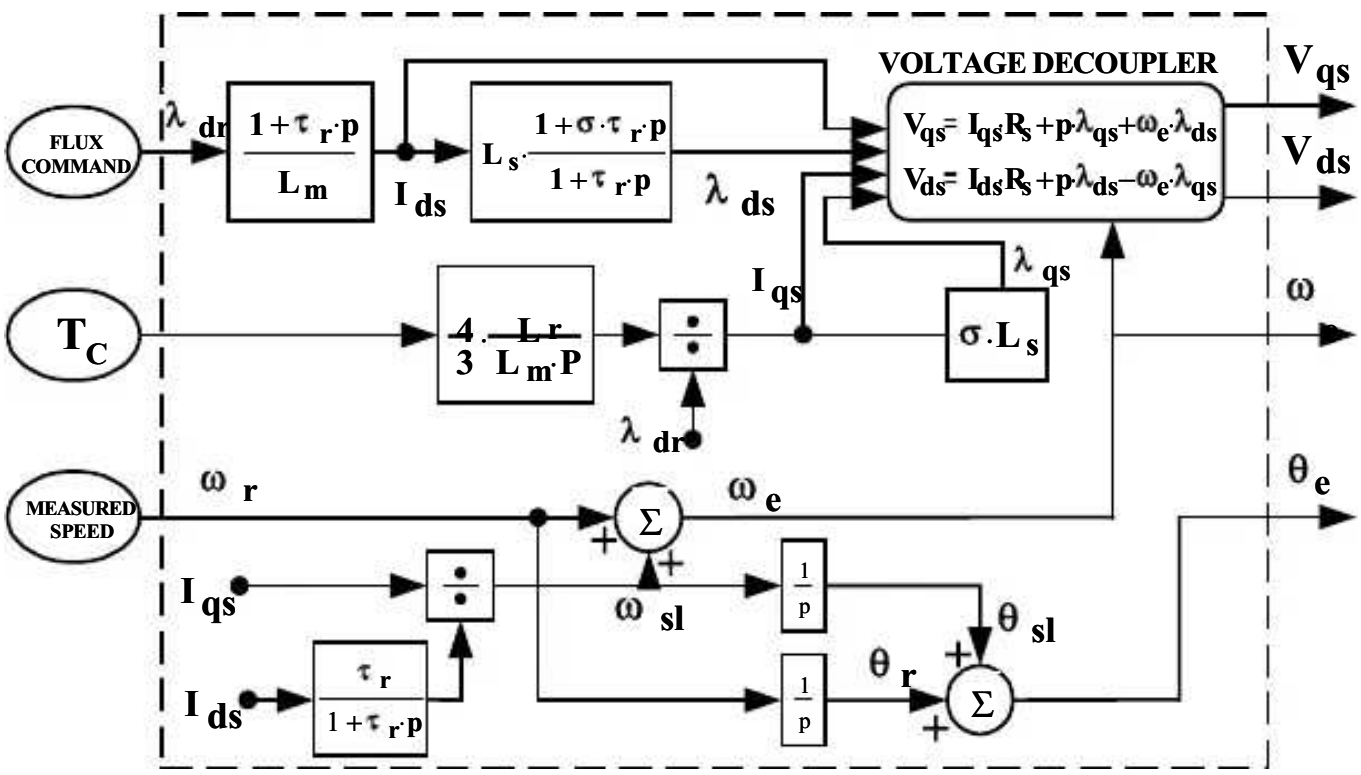

Fig. 4.8. Basic layout of Indirect field oriented controller model

4.3 Space vector PWM pulse generator model

The space vector PWM technique is used for controlling the switching of the machine side converter. Advantages of this method include higher modulation index, simpler control system, lower switching losses and less harmonic distortion compared to sinusoidal PWM [12].

A three-phase bridge converter has eight possible switching states with the constraint that no two switches in the same phase leg are both ON (or OFF) at the same time as shown in Fig. 4.9. Each state impresses a voltage across the wye connected machine windings, which can be represented by a voltage space vector.

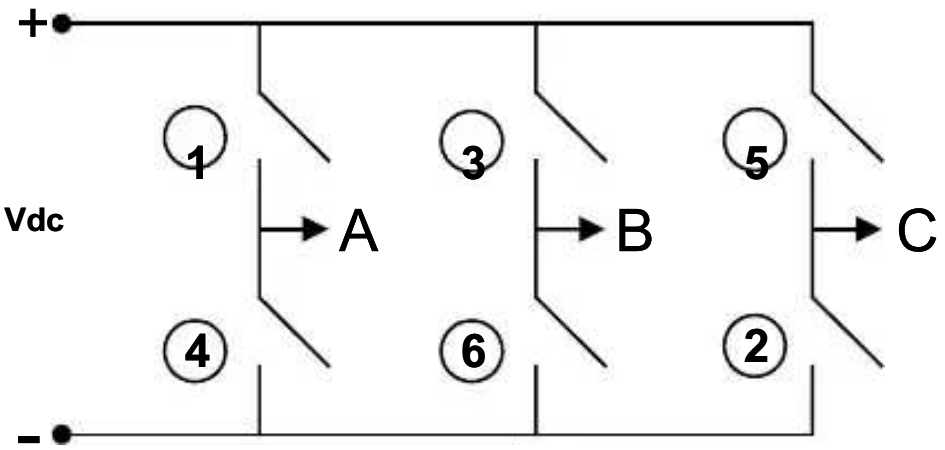

State	Switch	Vector
I	6-1-2	V1
II	1-2-3	V2
III	2-3-4	V3
IV	3-4-5	V4
V	4-5-6	V5
VI	5-6-1	V6
VII	1-3-5	V7
VIII	4-6-2	V8

Fig. 4.9. Bridge converter switching states

This results in six active vectors and two zero vectors as shown in Fig.4.10. The six active vectors divide the plane into six sectors each 60° apart with the other two zero vectors remain at the origin [12].

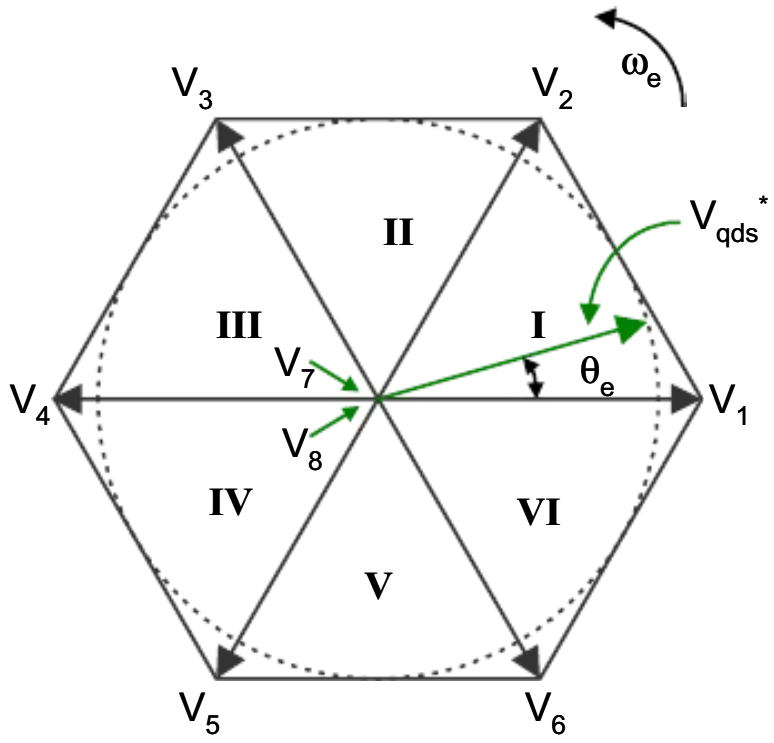

Fig. 4.10. Vector representation of switching states

The commanded voltage space vector (V_{qds}^*) can be constructed by the time distribution of the eight vectors over the switching interval (T_Z). To minimize the number of switching actions and thereby switching losses, only the two adjacent active vectors and the two zero vectors are used in a sector [12]. The time distribution of the two active vectors (T_a and T_b) and the zero vectors ($T_0/2$ and $T_0/2$) in each sector are computed using equations (4.25)-(4.27) where α is the active vector angle with reference to stationary reference frame q-axis.

$$T_a = \sqrt{3}\cdot\left(\frac{V_s}{V_{dc}}\right)\cdot T_Z\cdot\sin\left(\frac{\pi}{3}+\alpha-\theta_e\right) \tag{4.25}$$

$$T_b = \sqrt{3}\cdot\left(\frac{V_s}{V_{dc}}\right)\cdot T_Z\cdot\sin\left(\theta_e-\alpha\right) \tag{4.26}$$

$$T_0 = T_Z-\left(T_a+T_b\right) \tag{4.27}$$

A space vector pulse width modulator has been modeled in EMTDC. Fig. 4.11 shows the basic layout of the modulator model. The modulator fabricates the space vector PWM pulses with the commanded V_{ds} and V_{qs} voltages from IDFOC model, output frequency (ω_e), switching frequency and DC bus voltage (V_{DC}). It has the following sub-models:

- Time computer
- Asynchronous timer
- Sector pulse generator
- Variable Sample and hold circuit
- Pulse fabricator

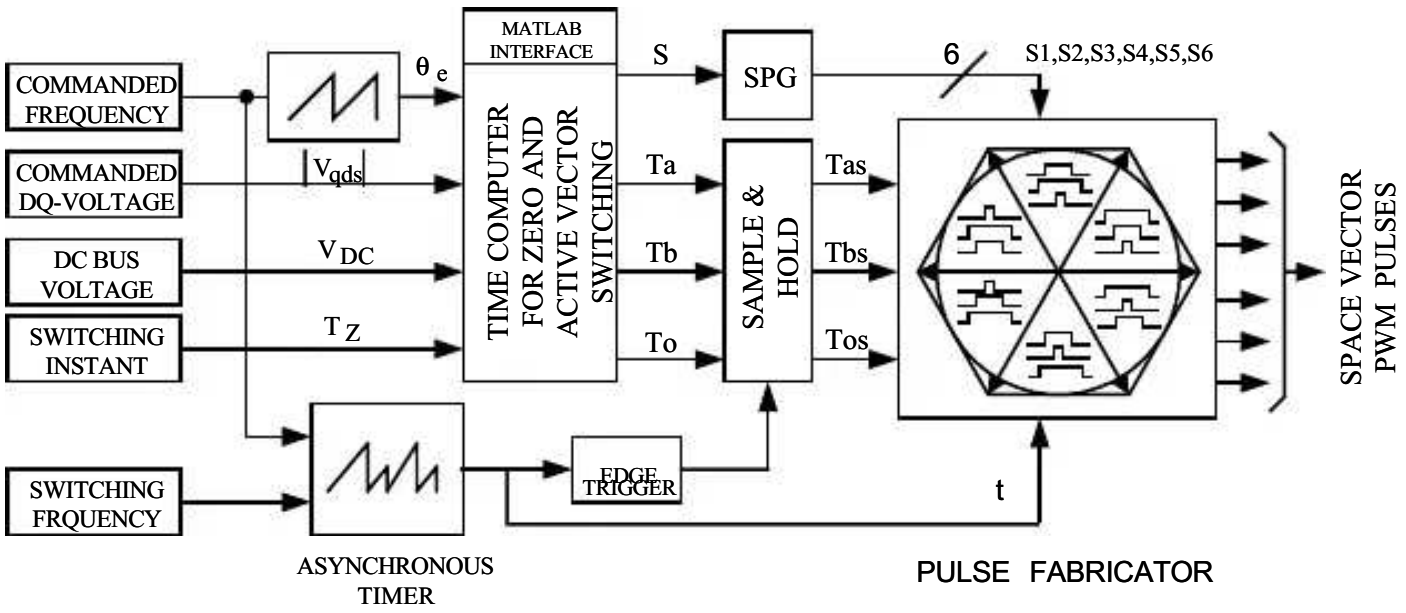

Fig. 4.11. Basic layout of space vector PWM pulse generator model

The distribution of the time the two active vectors and the zero vectors spend in each sector is computationally intensive. A time computer is modeled using a MATLAB script interfaced to EMTDC (see Appendix B 11.9 and 11.10). The script outputs the active and zero switching times (T_a, T_b and T_0) and sector reference (S). The inputs to the time computer are the commanded V_{ds} and V_{qs} voltages from

IDFOC model, angle reference (θ_e), the switching frequency and the DC bus voltage (V_{DC}). The angle reference, θ_e, is obtained using a Voltage Controlled Oscillator (VCO) component in EMTDC. The output is shown in Fig. 4.12.

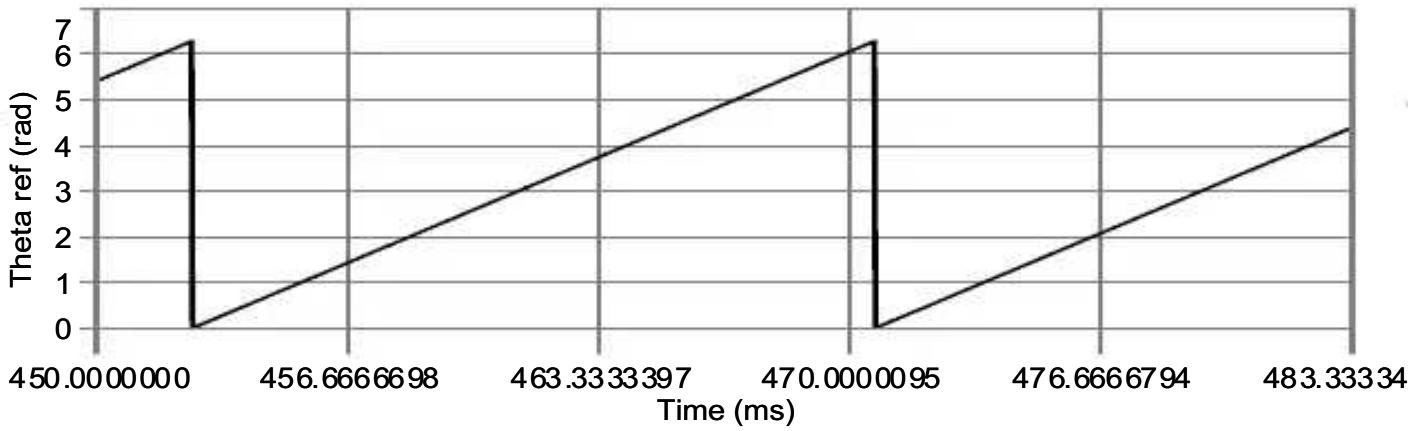

Fig. 4.12. Angle reference, θ_e, Time computer input

A sector pulse generator (SPG) generates pulses for the sector reference. It has one input (S) and six outputs (S1-S6). Fig. 4.13 shows the output 'S'. Depending on the sector the commanded space vector is in, only one of the six outputs are going to stay high as shown in Fig. 4.14.

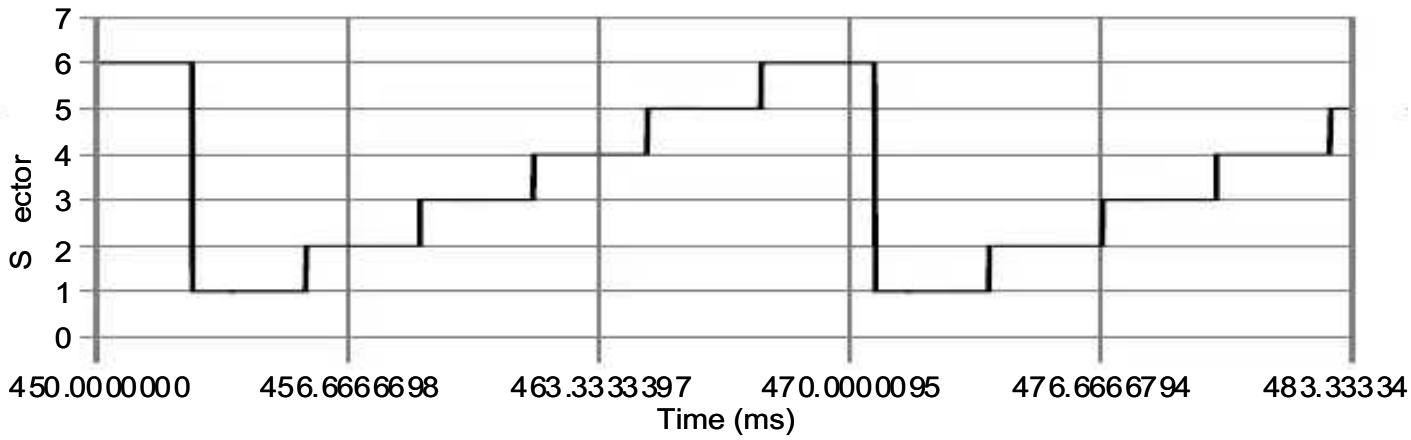

Fig. 4.13. Sector, S, Time computer output

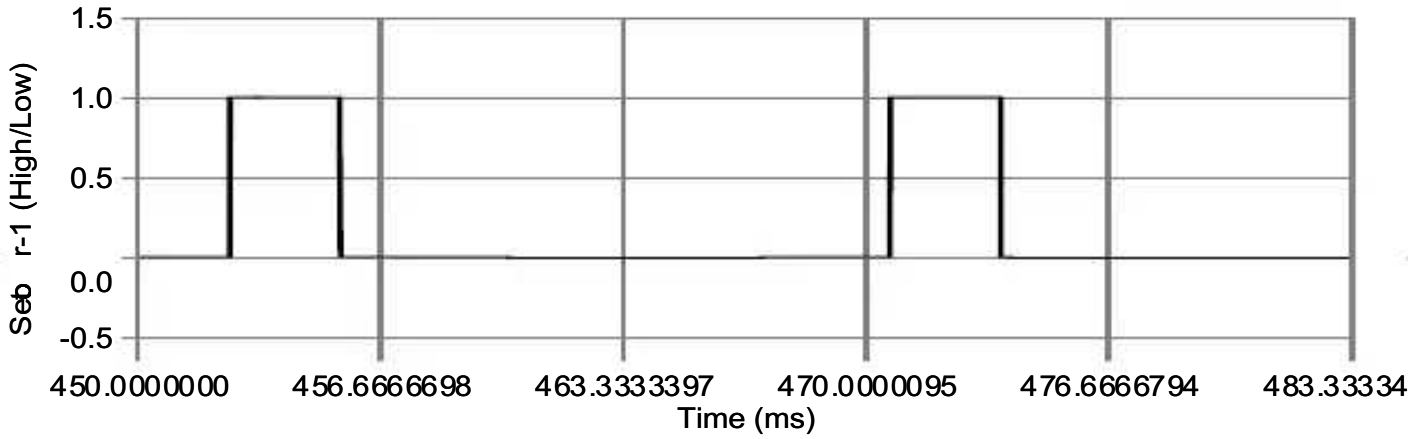
1.5
1.0
0.5
0.0
-0.5
Sector-1 (High/Low)
450.0000000
456.6666698
463.3333397
470.0000095
476.6666794
483.33334
Time (ms)

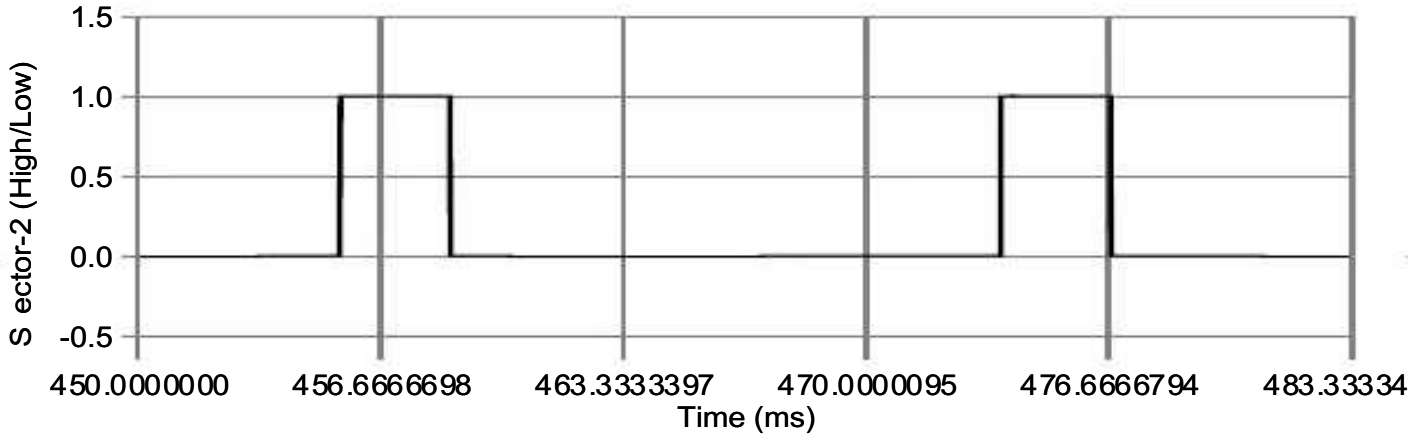
1.5
1.0
0.5
0.0
-0.5
Sector-2 (High/Low)
450.0000000
456.6666698
463.3333397
470.0000095
476.6666794
483.33334
Time (ms)

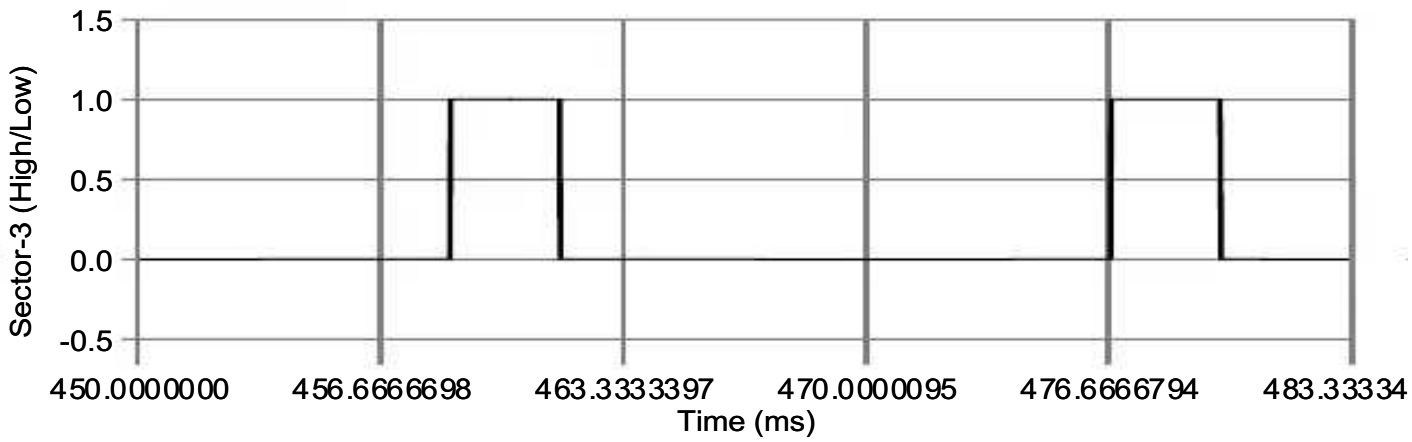
1.5
1.0
0.5
0.0
-0.5
Sector-3 (High/Low)
450.0000000
456.6666698
463.3333397
470.0000095
476.6666794
483.33334
Time (ms)

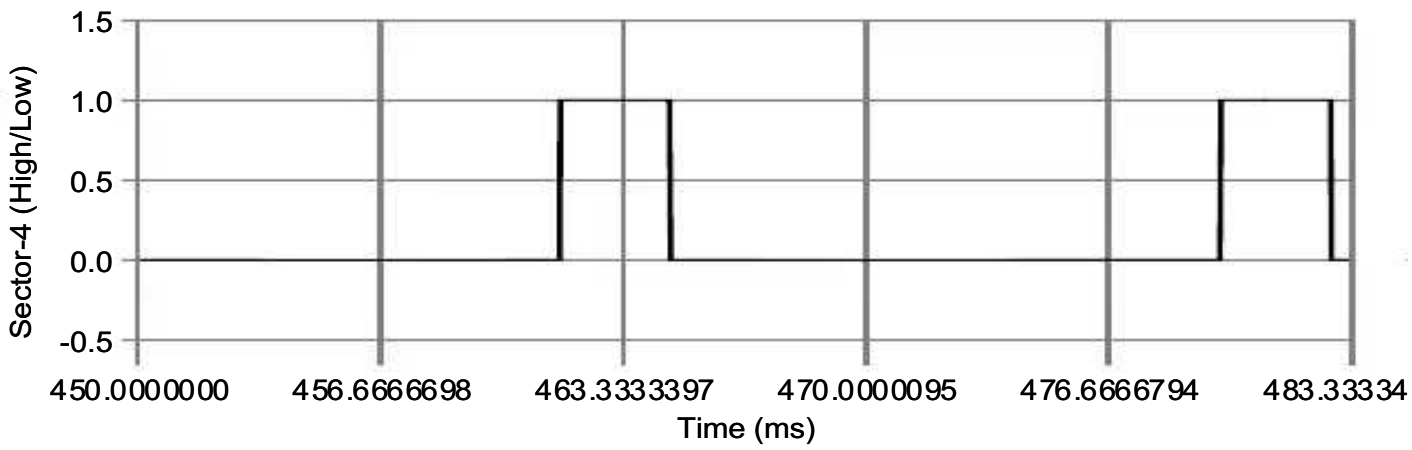
1.5
1.0
0.5
0.0
-0.5
Sector-4 (High/Low)
450.0000000
456.6666698
463.3333397
470.0000095
476.6666794
483.33334
Time (ms)

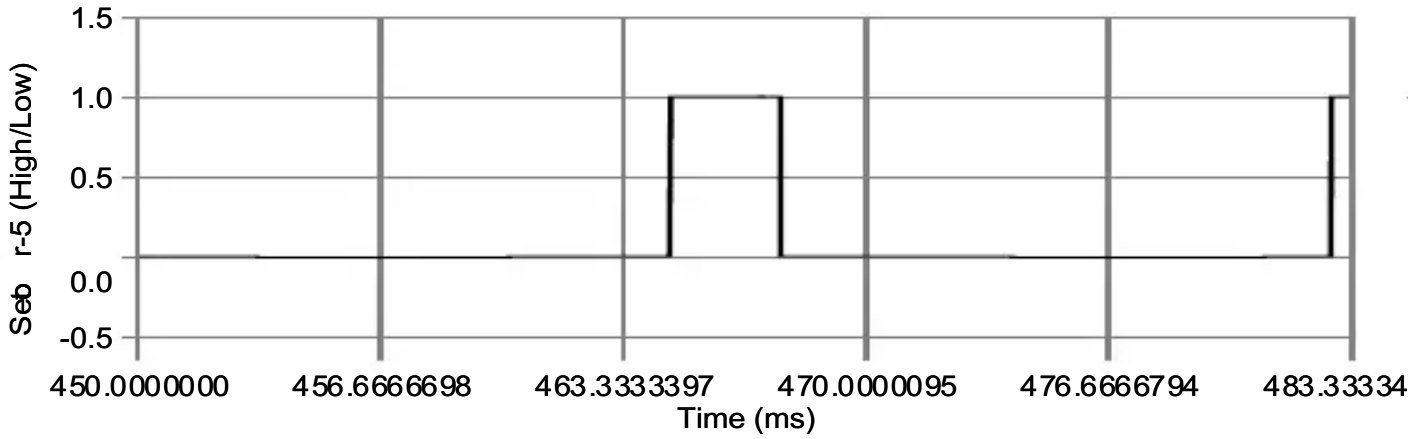

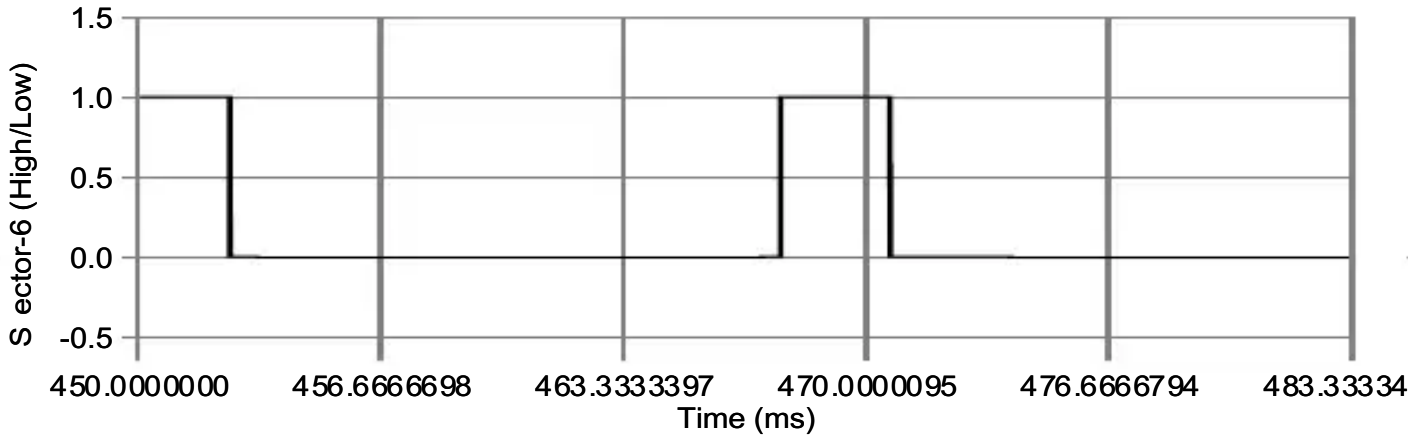

Fig. 4.14. Sector reference, S1-S6, Sector pulse generator output

An asynchronous timer acts as a time reference for sampling and pulse fabrication. The inputs to this timer are the commanded frequency and the switching frequency. The output is a switching time in seconds that resets every time a switching occurs. Since the time computer calculates the zero and active switching times in a particular sector, the timer needs to be forcefully reset whenever there is a sector transition.

For a switching frequency of 1kHz (the switching time is 1ms) and commanded frequency of 60Hz, (the sector time is 2.778ms ≈ 3ms), the asynchronous timer output resets three times (3ms/1ms) as shown in Fig. 4.15. A forced reset is not necessary in this case. Now consider for the same case but different switching frequency of 1.2kHz (the switching time is 0.83ms). The asynchronous timer output now resets 3.33 times (2.778ms/0.83ms=3.33). Now a forceful reset is necessary as shown in Fig. 4.16. A similar case results if the switching frequency stays the same and the commanded frequency changes. The

reset feature was added to make the space vector PWM pulse generator more flexible and reliable. A reset feature was added to the VCO component in EMTDC, the output of which is shown as Forced reset in Fig. 4.15 and Fig. 4.16.

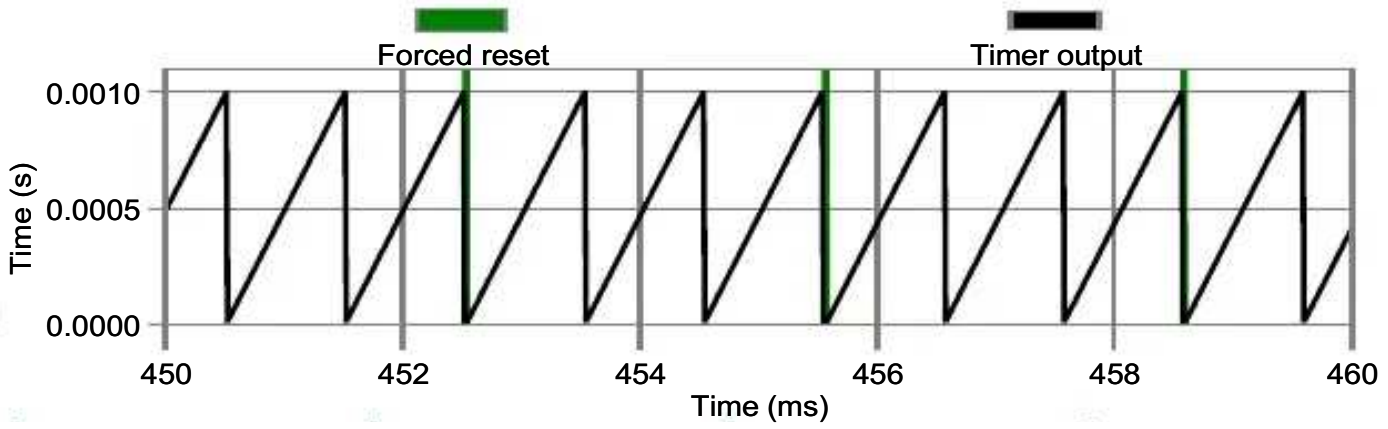

Fig. 4.15. Asynchronous timer output for 1.0kHz

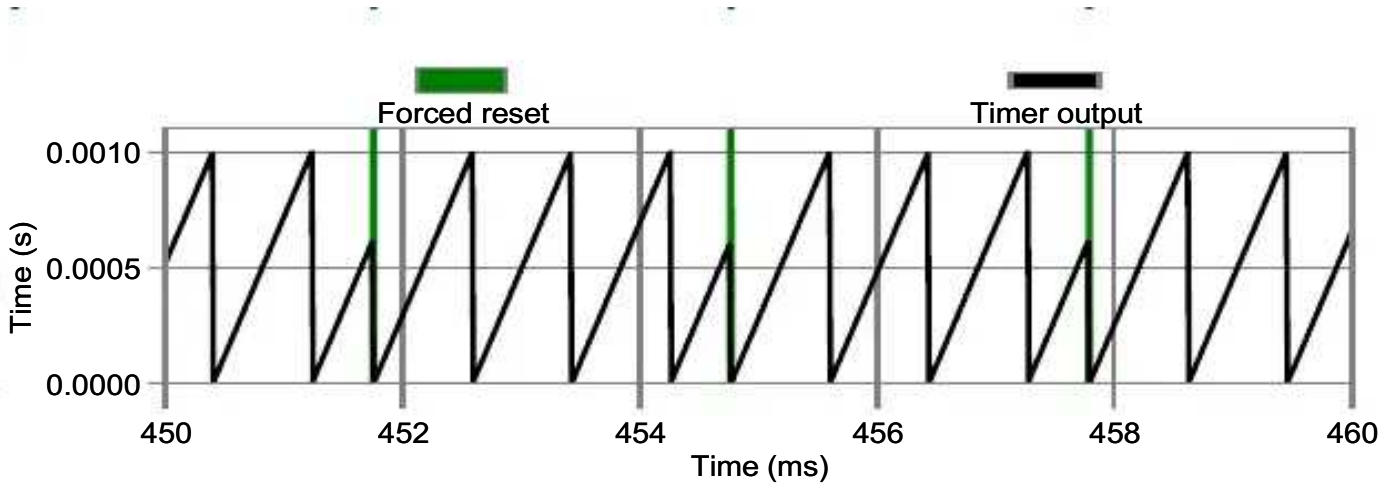

Fig. 4.16. Asynchronous timer output for 1.2kHz

The active and zero switching times calculated by the time computer are continuously varying with reference angle θ_e. They need to be constant during switching interval, so a sampler component in EMTDC is used. The sampling rate is dependent on the pulse train obtained from the edge triggered asynchronous timer.

Using the time reference, the sampled active and zero switching times, and sector reference, the pulse fabricator generates space vector PWM pulses. Table 4.1 shows the time distribution of the eight vectors in the sectors. The 1-3-5 indicates switches on the upper leg of the converter. The corresponding rows indicate the logic state of the switches H-High and L-Low. Note that only a single switch changes its state in a sector (to minimize switching losses). Also note that at the end of every sector the switches are back to their starting state.

Table 4.1 Time distributions of eight vectors in the sectors.

Sector	Tos/2	Tas	Tbs	Tos	Tbs	Tas	Tos/2
I	8	1	2	7	2	1	8
1-3-5	L-L-L	H-L-L	H-H-L	H-H-H	H-H-L	H-L-L	L-L-L
II	8	3	2	7	2	3	8
1-3-5	L-L-L	L-H-L	H-H-L	H-H-H	H-H-L	L-H-L	L-L-L
III	8	3	4	7	4	3	8
1-3-5	L-L-L	L-H-L	L-H-H	H-H-H	L-H-H	L-H-L	L-L-L
IV	8	5	4	7	4	5	8
1-3-5	L-L-L	L-L-H	L-H-H	H-H-H	L-H-H	L-L-H	L-L-L
V	8	5	6	7	6	5	8
1-3-5	L-L-L	L-L-H	H-L-H	H-H-H	H-L-H	L-L-H	L-L-L
VI	8	1	6	7	6	1	8
1-3-5	L-L-L	H-L-L	H-L-H	H-H-H	H-L-H	H-L-L	L-L-L

A common sequence for time distribution is hidden in Table 4.1 which is shown in Table 4.2. They are named X, Y and Z.

Table 4.2 Common sequence for time distributions.

Sequence	Tos/2	Tas	Tbs	Tos	Tbs	Tas	Tos/2
X	L	H	H	H	H	H	L
Y	L	L	H	H	H	L	L
Z	L	L	L	H	L	L	L

The pulse fabricator generates pulses that are high for the Tas, Tbs and Tos times using comparators. These pulses need to be distributed according to the sequence shown in Table 4.3. This was done by using an array of AND gates (see Appendix-A). The outputs are OR'ed output of each sequence column in Table 4.3, which are the gate pulses to 1-3-5 of the converter. Fig. 4.17 shows the space vector

PWM pulse generator output pulses for the top three IGBT's (1-3-5) of the converter. The gate pulses to 2-4-6 are the inverted 1-3-5 gate pulses.

Table 4.3 Sequence for time distributions in each sector.

Sector	Sequence
I	X-Y-Z
II	Y-X-Z
III	Z-X-Y
IV	Z-Y-X
V	Y-Z-X
VI	X-Z-Y

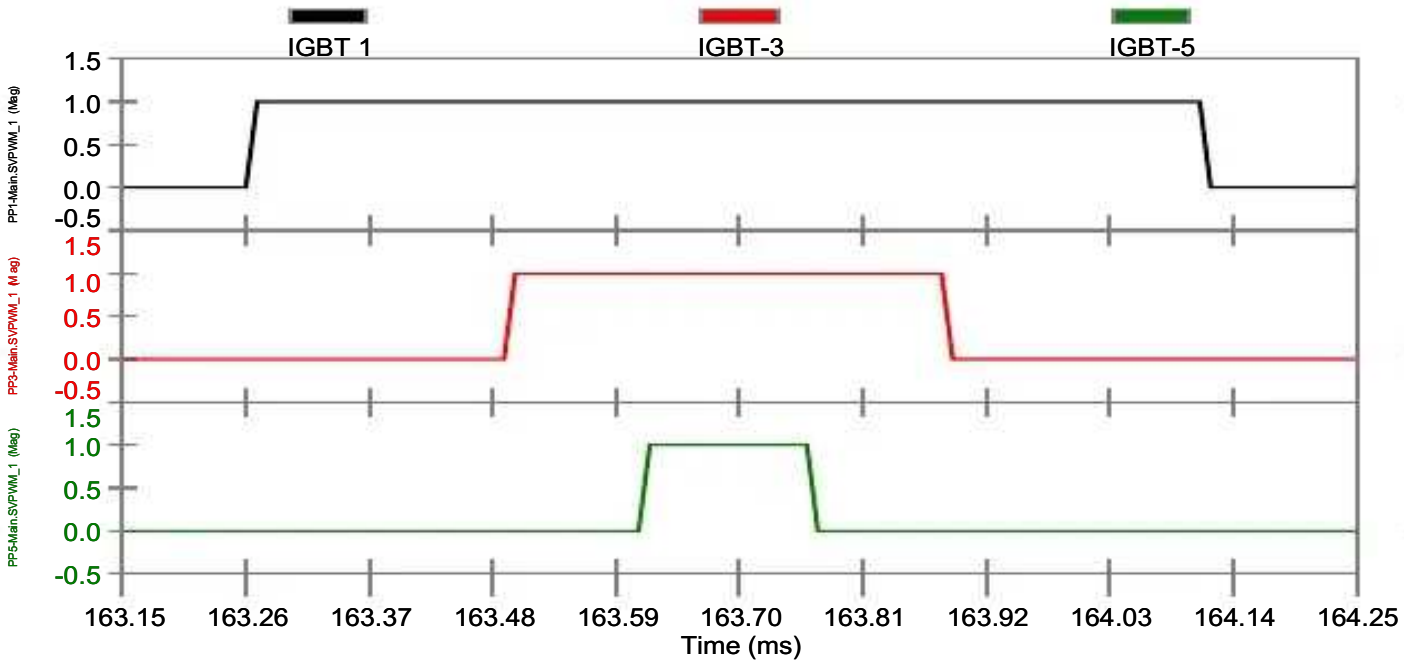

Fig. 4.17. Space vector PWM output pulses in sector 1

The software layout of a field oriented control AC drive is shown in Fig. 4.18. It consists of all of the custom models that were discussed in this chapter integrated into a field oriented controlled AC drive.

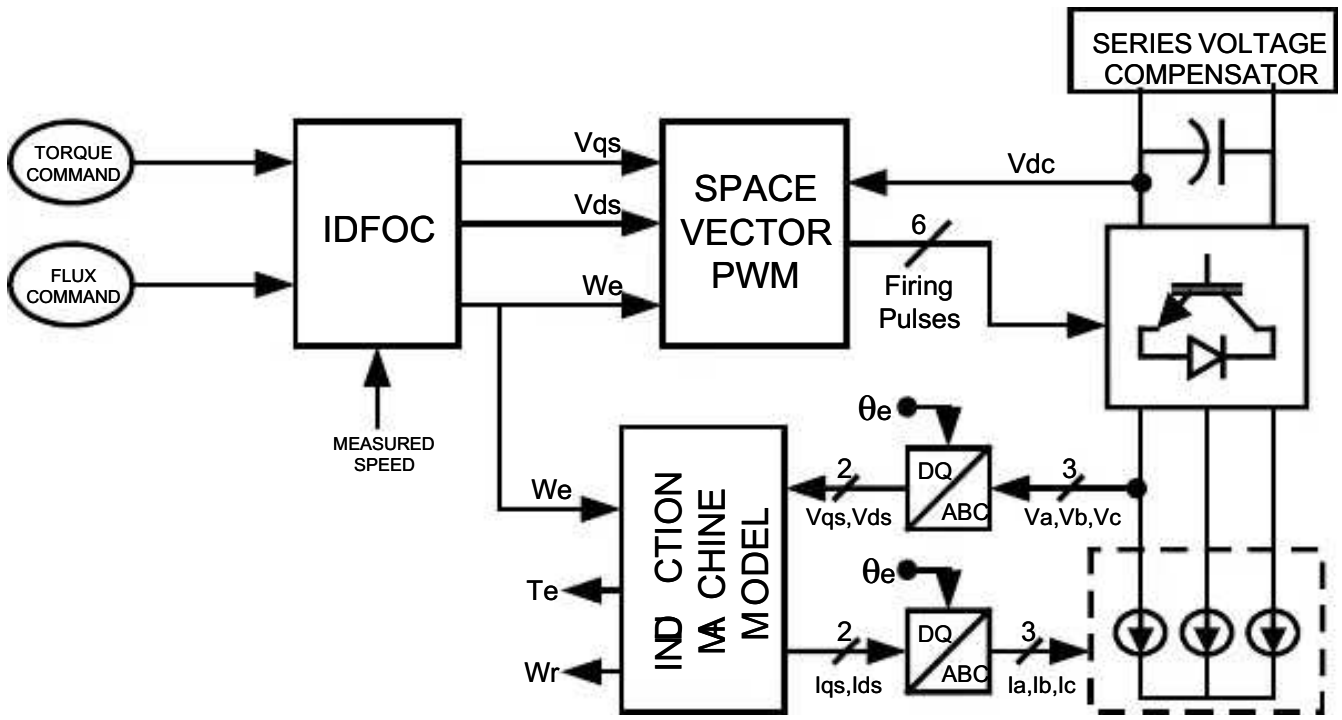

Fig. 4.18. Software layout of a field oriented AC control drive

5.0 STATIC SERIES COMPENSATOR MODEL

A static series compensator injects three AC voltages of variable amplitude and phase angle into the line for voltage sag correction. Without energy storage, the compensator can only inject voltages in quadrature with the load current and hence larger voltage injection is required to mitigate the voltage sag. In addition, purely reactive static series sag compensator is only effective for small voltage sags. With energy storage, the static series compensator has flexibility to inject voltage at any phase angle and can compensate for deeper and longer voltage sags.

Fig. 5.1 shows the basic layout of the static series compensator, modeled in EMTDC (see Appendix B). It consists of a shipboard power system model, series transformer, LC filters, VSC and a sinusoidal PWM pulse generator for controlling the SPS side VSC.

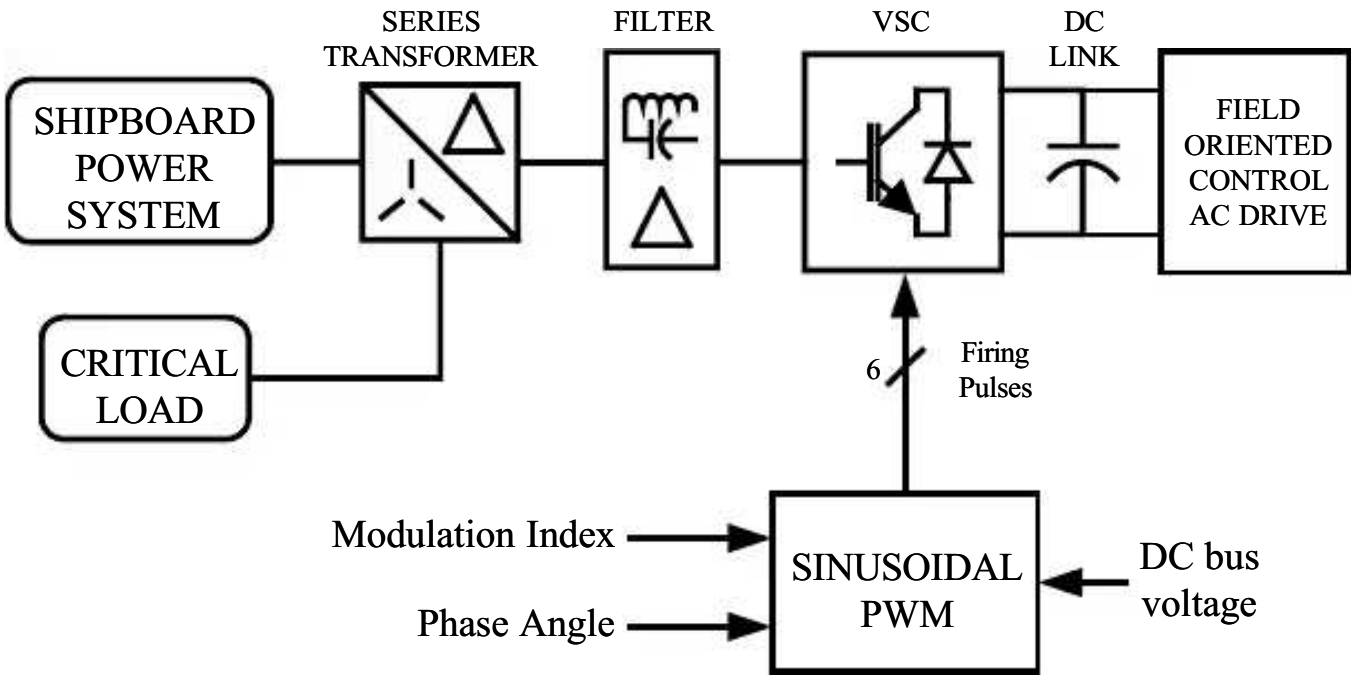

Fig. 5.1. Basic layout of a static series compensator

5.1 Shipboard power system model

The shipboard power system is modeled as a simple radial system with a source, a bus and two loads as shown in Fig. 5.2. One is a sensitive load to which the flywheel energy storage system is connected in series. The other load is connected to the same bus through a distribution line. When a fault occurs at this load, the sensitive load experiences voltage sag. Faults are created using a three phase fault component. The duration of the fault is controlled by a timed fault logic component. The depth of the sag can be changed by varying the length of the distribution line or source impedance.

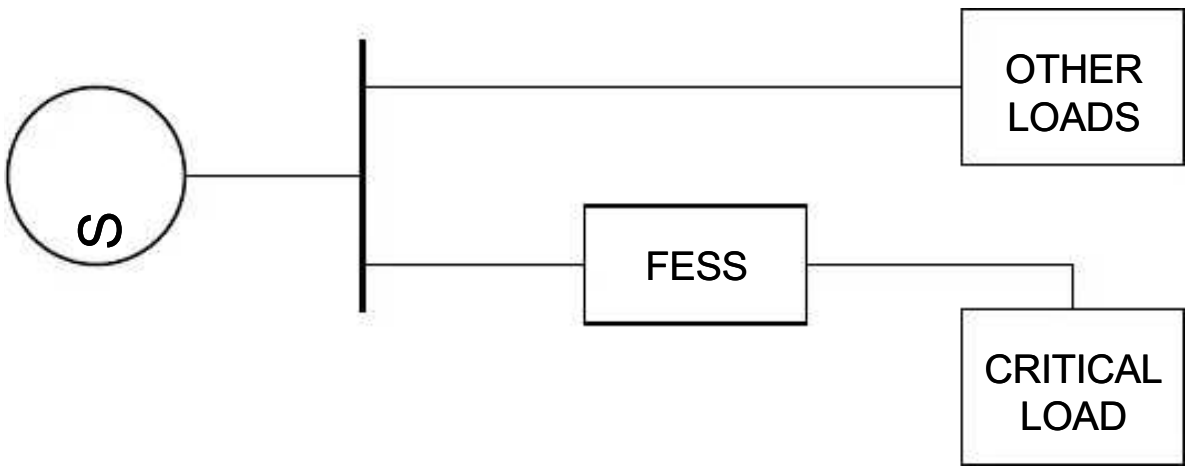

Fig. 5.2. Shipboard power system model

5.2 Series transformer and filters

The series injection transformer can be connected in two ways, either wye/open winding or delta/open winding. Delta/open winding is used since it prevents the third harmonic and zero sequence currents from entering the system and also maximizes the use of the DC link compared to wye/open winding. A delta connected LC filter bank is used to smooth the injected voltage. Filters delay the response of the energy storage system to voltage sags.

5.3 Sinusoidal PWM pulse generator model

A sinusoidal pulse width modulator is modeled in EMTDC to control the switching of the VSC on the SPS side. For a given amplitude modulation index, phase angle reference, AC system frequency and DC bus voltage, it generates firing pulses for the converter. The switching frequency is 10.8kHz. The amplitude is fixed at 1.0 and phase angle is controlled such that during standby mode the injected voltage and line current are in quadrature. During the discharge mode a proportional integral feedback error between the per unit magnitude of the measured critical load voltage space vector and the reference value (0.95) is computed such that the phase angle reference remains the same as the pre sag value. During the charge mode the speed and DC bus controllers allow the energy to flow into the flywheel and when the flywheel reaches its rated speed it is again in standby mode with the line current in quadrature to the injected voltage.

The models were integrated and tested by replacing the machine side with an equivalent current source before integrating it with the field oriented control AC drive model (see Appendix B).

6.0 CONTROL SYSTEM

The control system consists of two main parts, an inner control system and an outer control system. The inner control system consists of the two firing schemes for controlling the two voltage sourced converters. A sinusoidal PWM scheme is used for static series compensator, and a space vector PWM scheme is used for the field oriented controlled AC drive. The control system can be viewed as having two levels. The outer control system responds to the external system. The inner control system generates the gate pulses for the devices in the converters based on inputs from the outer control system. The inputs to the sinusoidal PWM are controlled directly by the outer control system. The inputs to the space vector PWM are indirectly controlled by the outer control system with a field oriented controller. The outer control system consists of a sag detector, sag corrector and an energy control system. The basic layout is shown in Fig. 6.1.

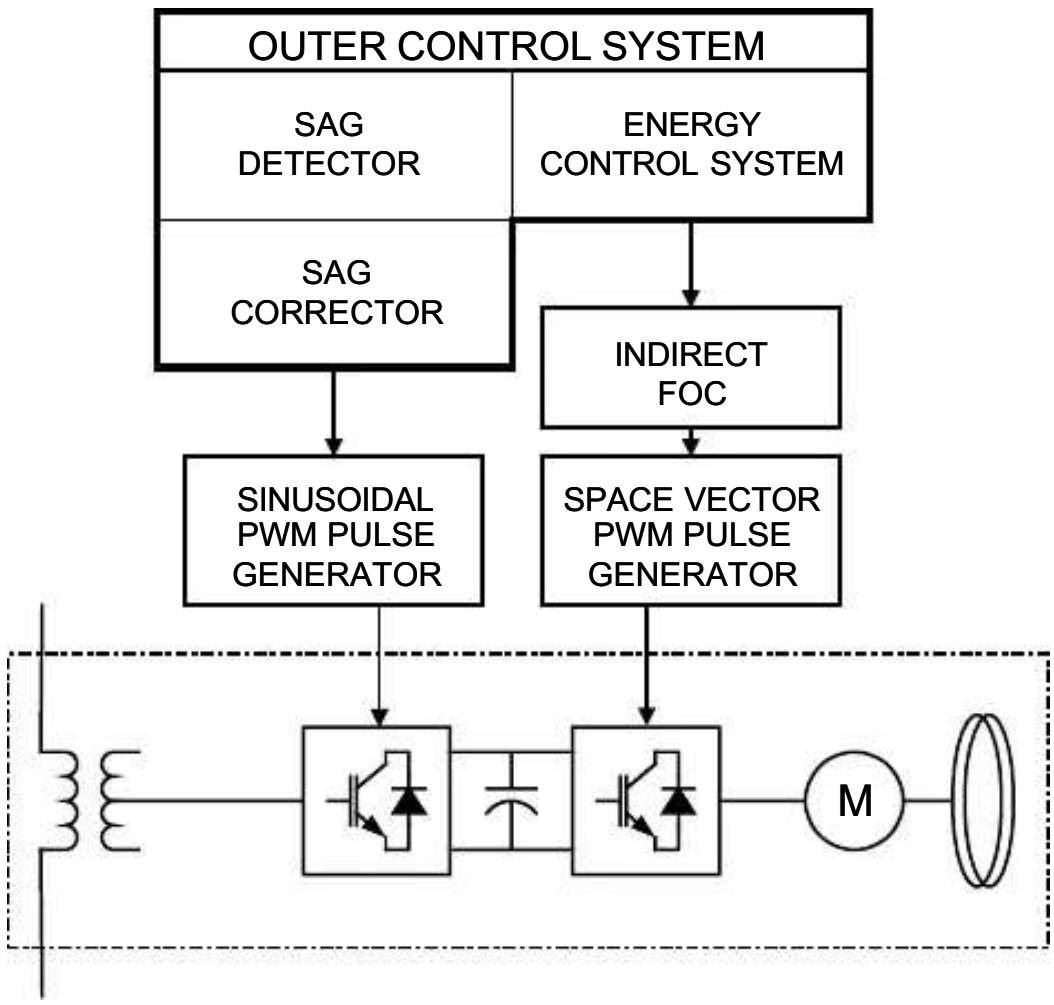

Fig. 6.1. Control System Layout

The outer control system determines the energy to flow in to and out of the system according to the sag correction and flywheel recharging needs. The outputs of this control system are a torque command, modulation index and phase angle, which are inputs to the inner control system.

6.1 Sag Detector and Corrector

6.1.1 Sag Detector

The sag detector detects the presence of voltage sag and activates the control system for sag correction. The layout of the sag detector is shown in Fig. 6.2. The output, SD, is a pulse that is active as long as the voltage is out of tolerance during the sag. The inputs are the voltages measured on the SPS side of the series transformer. The measured voltages are converted to D-Q space vectors in a synchronously rotating reference frame. The per unit magnitude of this space vector is compared to a reference value of 0.98. Theoretically, the reference value could be set to 1.0, but that makes the energy storage system overly sensitive resulting in incorrect compensation of transients at the end of sag. A transient of 1% reduction is seen at the end of the voltage sag, so the reference value is set to 0.98 to prevent sag detector detecting it. It can be set to any value from 0.91 to 1.0 depending on the maximum transient that may occur after a voltage sag.

The sag detector provides an accurate result for balanced voltage sags. The energy storage response is based on how fast the sag is detected and how reliably it is detected.

The advantage of using synchronous reference frame is that the inputs are DC and hence control system is simpler. Also, compared to RMS based sag detectors, the D-Q based sag detectors have faster response time as they are based on instantaneous quantities. RMS based sag detectors have slow response time since they are based on half cycle or full cycle of instantaneous data [4].

6.1.2 Sag Corrector

A proportional feedback controller for voltage sag correction is shown in Fig. 6.2. The output, T_{SAG}, is a negative torque command to the energy control system. T_{SAG}, is a scaled error of the difference between the per unit magnitude of the SPS voltage space vector measured and the reference value (1.0 p.u). T_{SAG} value is limited by the amount of energy available for discharge and stability conditions of the energy storage system. A detailed analysis of this will be a future topic. A simple hard limiter was used for limiting the maximum and minimum value of the negative torque output.

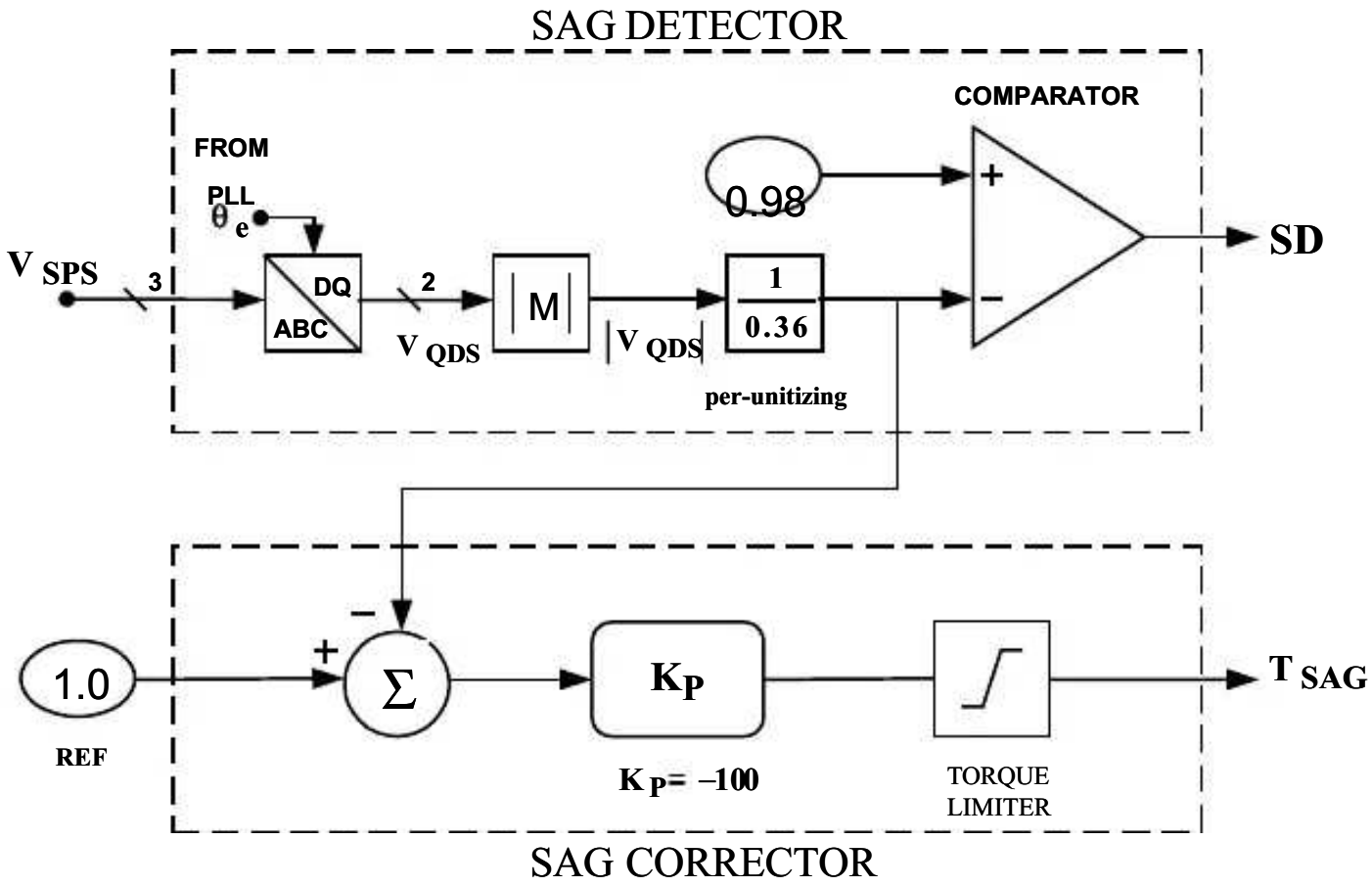

Fig. 6.2. Sag detector and sag corrector layout

6.2 Energy Control System

Fig. 6.3 shows the basic layout of the energy control system. The output is a net torque command to the Indirect FOC, which is the sum of outputs from three main control blocks: DC voltage control, speed control and sag correction control. The torque command, T_C, is an input to the Indirect FOC in Fig. 4.8.

A proportional integral feedback controller is used for controlling rotor speed and DC bus voltage. Speed control, the slowest controller, is used for charging the flywheel to its rated speed when the sag is cleared. If the sag detector detects a sag, SD goes high. This results in bypassing the speed and DC bus voltage controllers (as shown with the inverters), such that T_C equals T_{SAG}, and improves the response time. Once the sag is cleared, SD goes low, reactivating the speed and DC bus voltage controllers. The speed controller is intentionally made slower to prevent sag due to charging the flywheel and thereby improving stability of the energy storage system.

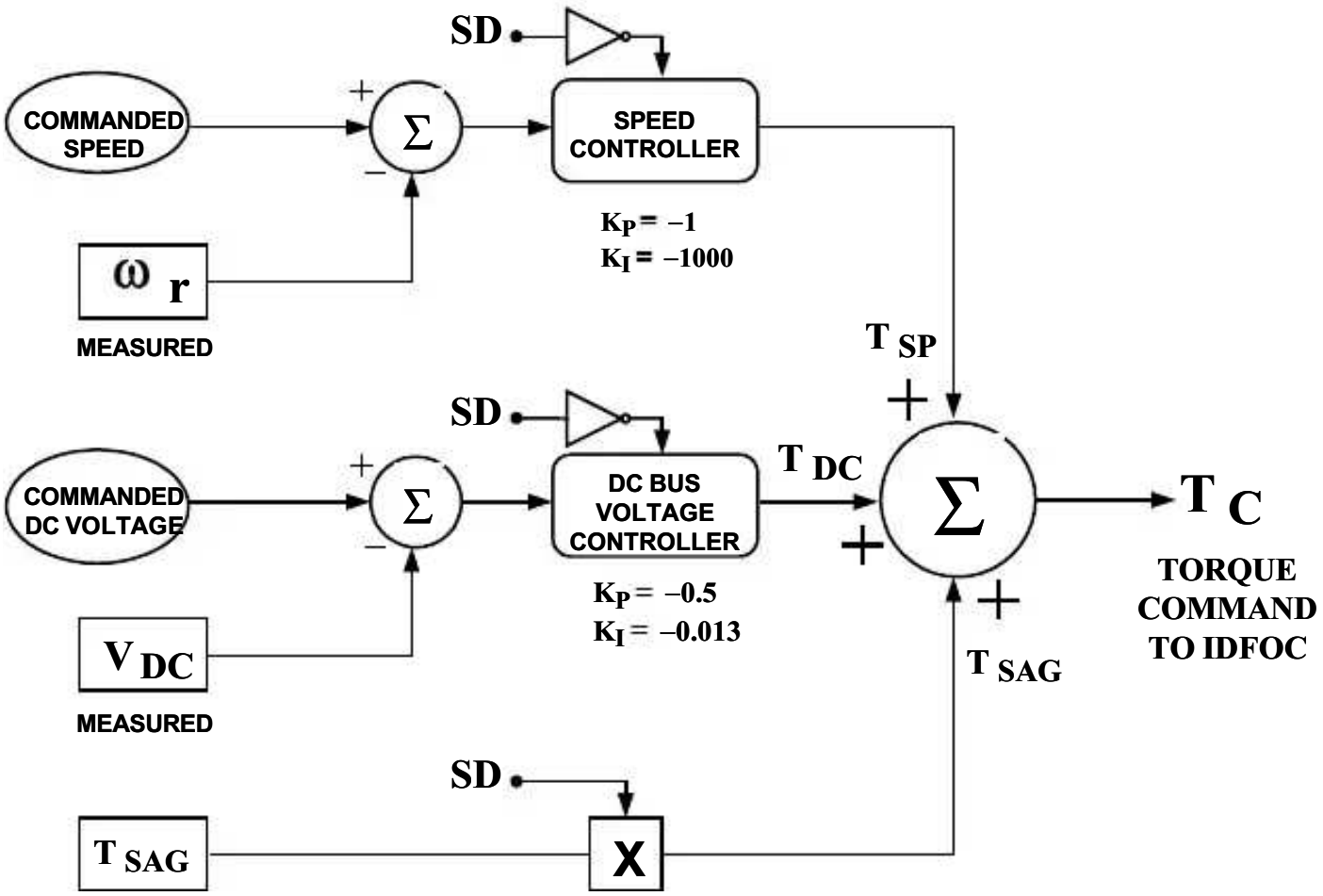

Fig. 6.3. Energy control system layout

7.0 RESULTS

The models discussed in Chapters 4 through 6 are integrated with a flywheel energy storage system model and a test case was created to analyze its performance. Appendix B provides more detail on how these models were integrated.

7.1 Test case

The flywheel energy storage system performance is analyzed by creating a three phase fault at the location shown in Fig. 7.1, resulting in a balanced voltage sag of 63% on the SPS side of the series transformer. The depth of the voltage sag depends on this distance of the fault from the bus. The fault occurs at 1.5sec in to the simulation time frame, and has duration of 20 cycles (60Hz). The simulation time step is 10 microseconds.

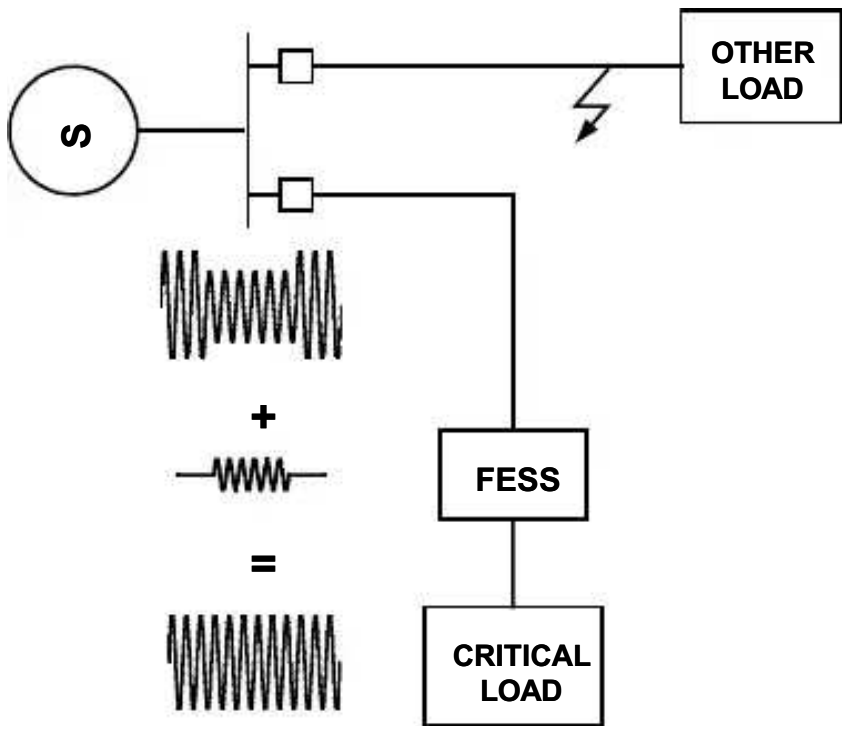

Fig. 7.1. Test case for analyzing FESS performance

7.2 Analysis of simulation results

Fig. 7.2 shows the detection of the voltage sag by the sag detector. SD is zero until the fault is detected and then goes high (logic value 1.0) when the SPS voltage is out of tolerance. The output VdqSPS is the per unit magnitude of SPS side voltage space vector and VabcSPS is the per unit RMS voltage. Note that the space vector voltage magnitude changes much more quickly, since it is based on instantaneous quantities, and not averaged over a cycle as the RMS voltages are. Therefore, a RMS voltage reference based sag detector will react more slowly, and hurt the response of the system. The space vector based DQ voltage is used to provide faster, more accurate detection of the voltage sag.

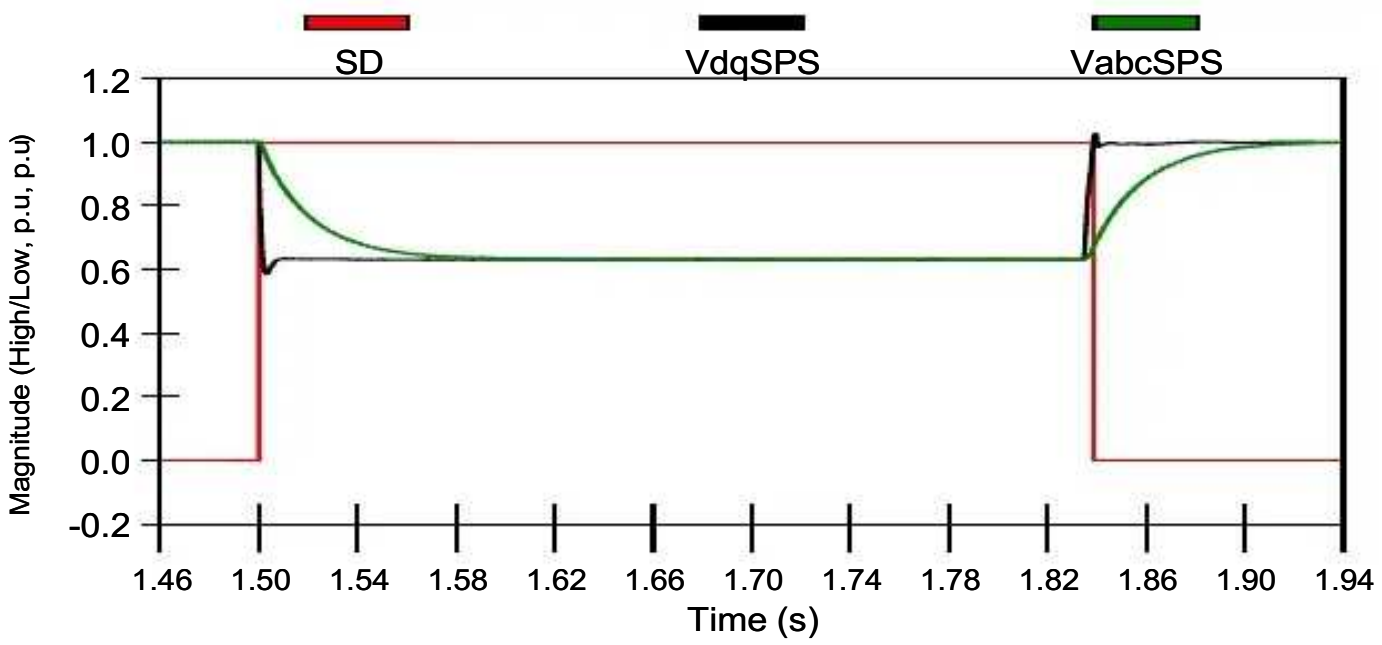

Fig. 7.2. Sag detector response

When SD goes high, as shown in Fig. 7.2, the sag corrector is activated and the speed and DC bus controllers are bypassed. The sag corrector commands a negative torque, T_{SAG}, to the IDFOC, for energy conversion. The flywheel was in standby mode, running at 346 rad/s, until t=1.5sec when SD goes high.

Fig. 7.3 shows the flywheel slowing down due to the negative torque command from 346 rad/s to 318 rad/s. Fig. 7.4 shows the DC bus voltage variation from rated (340V) during energy reversal.

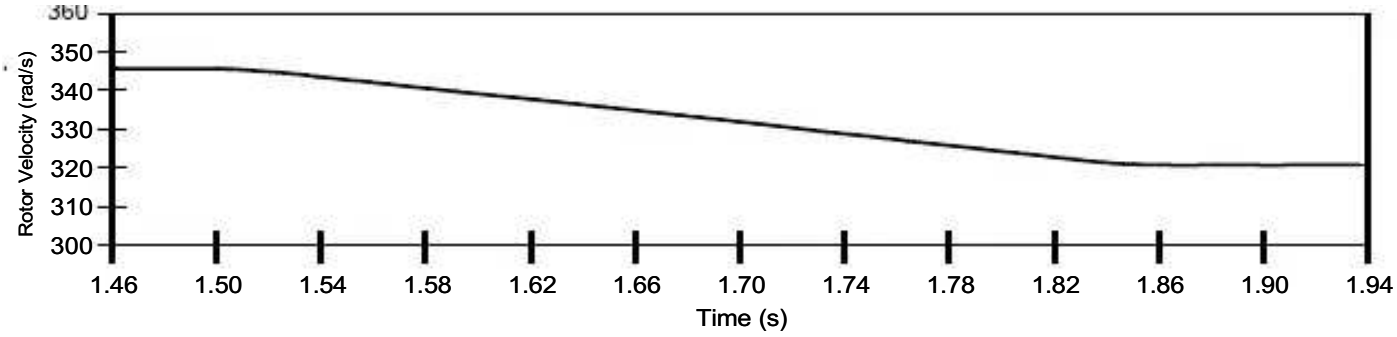

Fig. 7.3. Rotor angular velocity variation

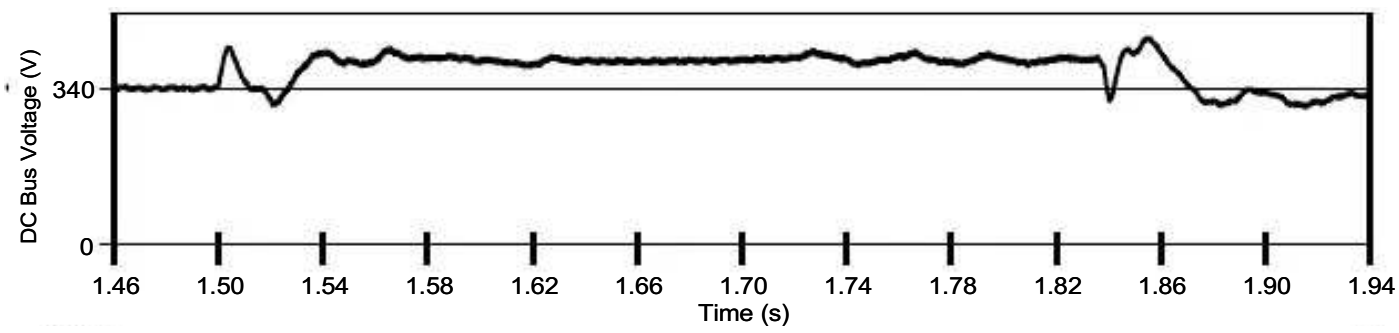

Fig. 7.4. DC bus voltage variation

Fig. 7.5 shows the power flow measured into the machine terminals and into the secondary of the series transformer. It shows the response of the power electronic interface during energy reversal.

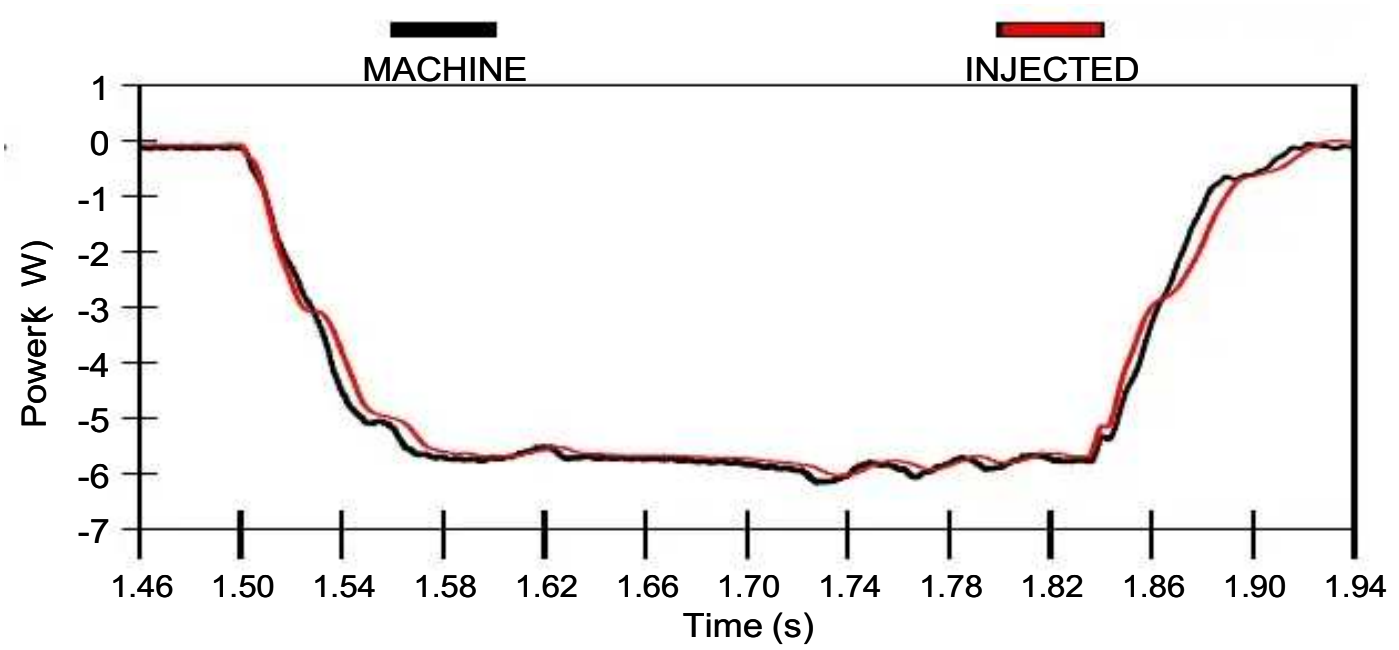

Fig. 7.5. Power flow into the machine and static series compensator

Fig. 7.6 shows the per-unit RMS voltage on the critical load side and the SPS side. The RMS voltage on the SPS side was initially at 1.0p.u. A voltage sag of 63% is seen lasting for 20 cycles (60Hz). The RMS voltage on the critical load side was

corrected to 0.95p.u (5% less from pre-sag voltage). An over voltage of 1.1p.u is seen at the end of the sag.

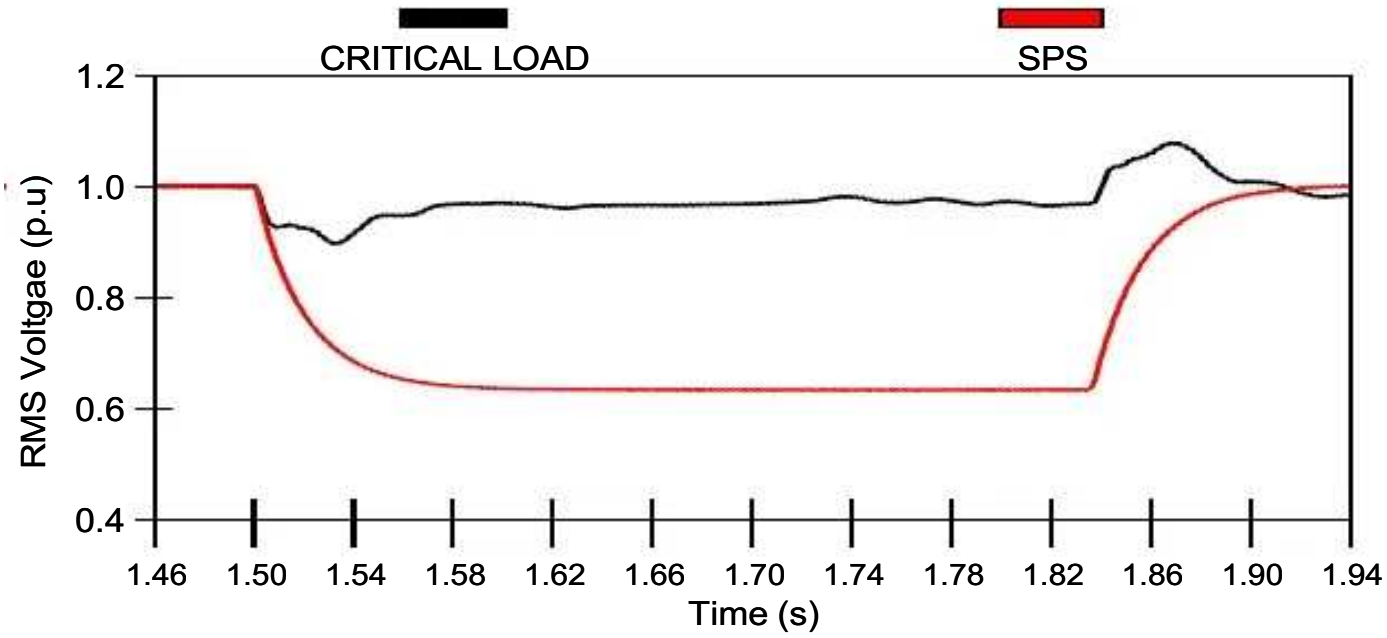

Fig. 7.6. RMS voltages measured at the critical load side and SPS side

Fig. 7.7 and Fig. 7.8 show the phase-to-ground voltages on the SPS side and critical load side of the FESS. The FESS responded within 2 cycles to keep the critical load voltage within the 5% tolerance (i.e. the sag is corrected to 0.95 per unit, not to 1.0 per unit).

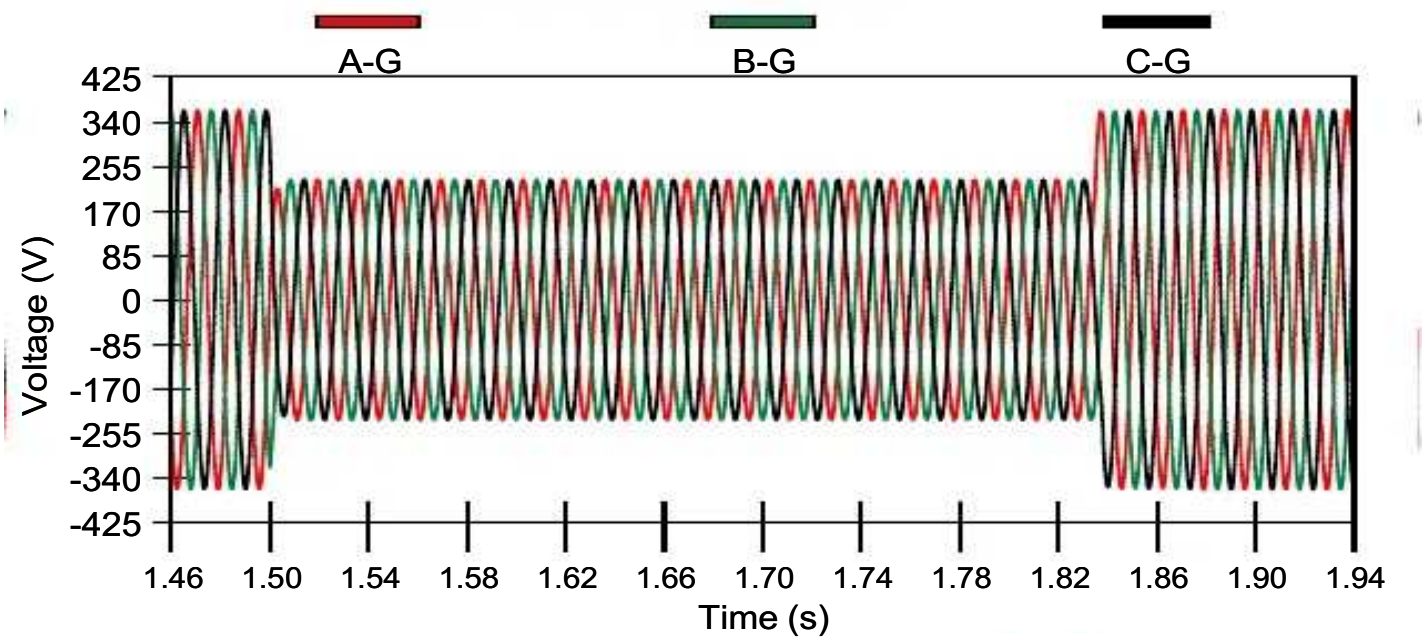

Fig. 7.7. Phase to ground voltages on the SPS side

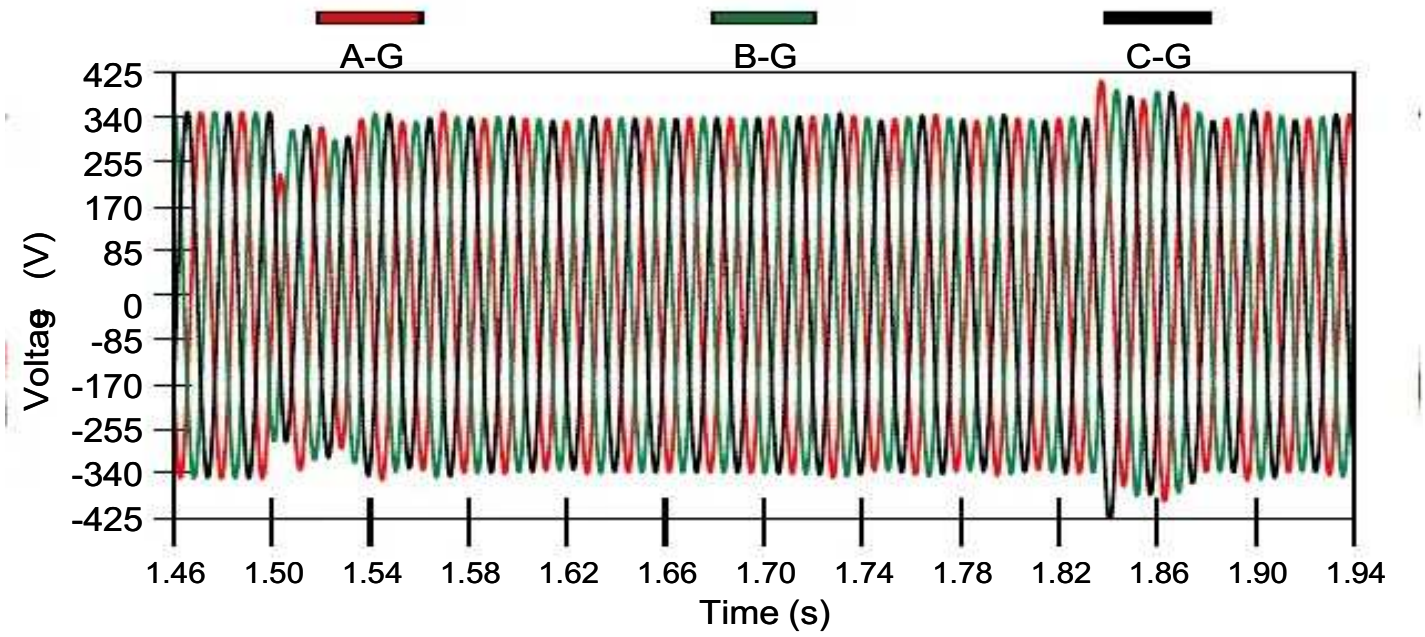

Fig. 7.8. Phase to ground voltages on the critical load side

The sag correction can be done for 0% tolerance, but it will result in larger overvoltages at the end of the sag, with the potential to cause insulation damage. In this case, the critical load voltage was regulated below 5% of the nominal.

Fig. 7.9 shows the phase relationship between series injected voltage by the VSC on the SPS side and the load current to the critical load. There is no power injection initially since the injected voltage is in quadrature with line current. During voltage sag correction the phase angle is almost in phase thereby allowing energy to flow into the shipboard power system.

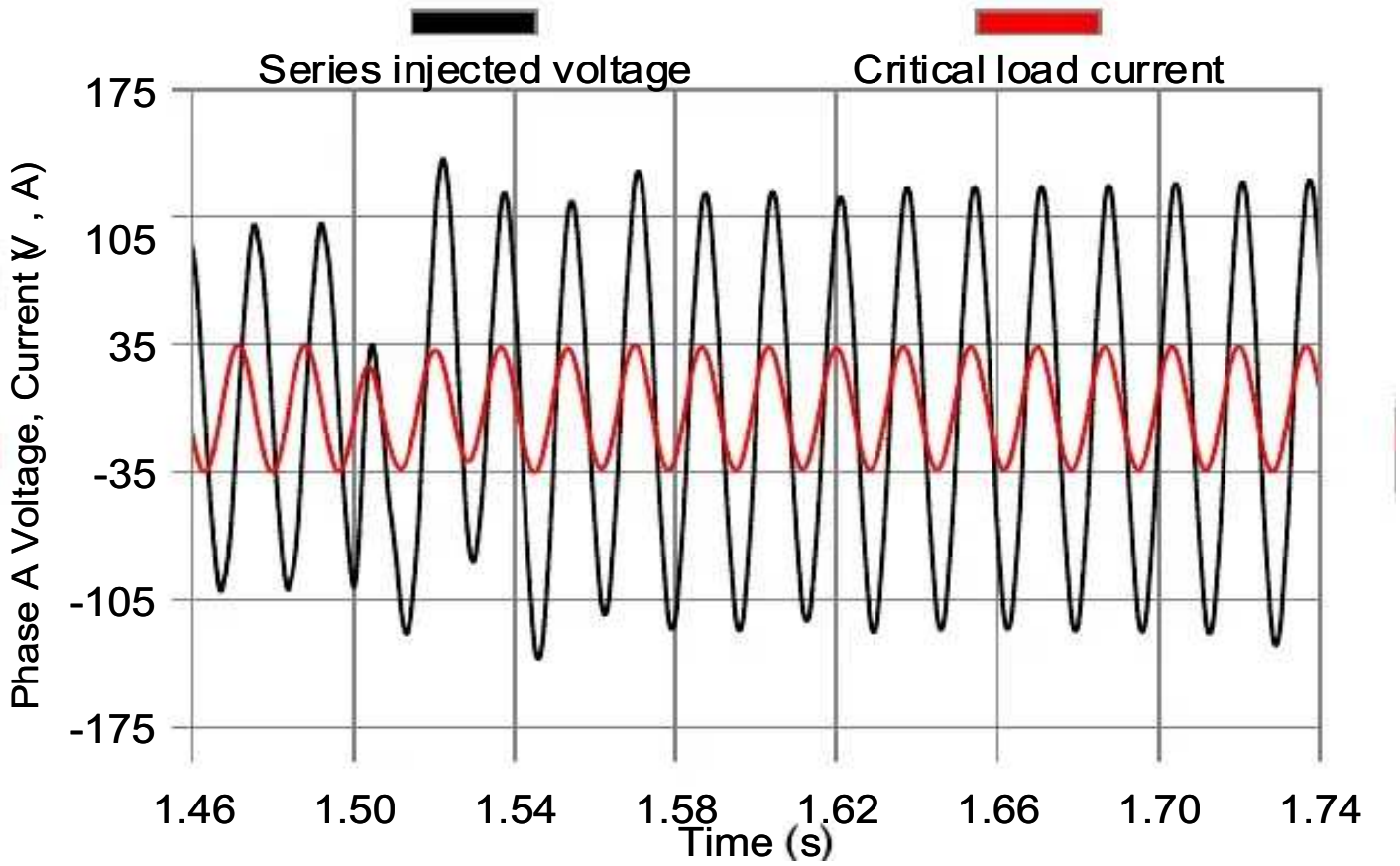

Fig. 7.9. Phase A-Ground voltage at the critical load and SPS, injected voltage and Phase A line current

8.0 CONCLUSIONS AND FUTUREWORK

8.1 Conclusions

The modeling and analysis of a flywheel energy storage system for voltage sag correction on a shipboard power system has been presented. A control scheme has been proposed for voltage sag correction and energy control. The sag correction is based on negative torque command, which is a scaled error of the difference between shipboard power system side of the synchronously rotating reference dq voltage and its reference. An energy control system that regulates the DC bus voltage and charges the flywheel has been described. A dq space vector based sag detector has been modeled for sag detection. A feed forward control by the sag detector output which disables the speed and DC bus voltage controller improves the energy storage system performance in mitigating voltage sags.

The shipboard power system and the power converters were modeled using EMTDC, along with the full transient synchronous reference based dq induction machine and flywheel model. An indirect field oriented controller for the control of flywheel induction machine was also modeled in EMTDC. The space vector PWM pulse generator model to generate firing pulses for the flywheel converter was modeled in MATLAB and interfaced to the switching device models in EMTDC. The overall energy management scheme, the sag detector, and the sag corrector were all modeled in EMTDC, along with the control scheme for the shipboard power system side VSC.

The response of the energy storage system to a balanced voltage sag was presented. The advantage of a dq space vector based sag detector over RMS based sag detector has been shown. The instantaneous voltages are compensated within 2 cycles to keep the voltage tolerance within 5% of rated voltage. The main advantage of this FESS is high power density. It can mitigate long duration voltage sags efficiently.

8.2 Future work

The future work should include more detailed analysis of the control scheme for energy storage system for unbalanced sags and comparison of its performance with a laboratory flywheel interfaced to an analog model power system (AMPS). The same approach done for modeling the energy storage system in EMTDC can be applied to build a laboratory model.

The following figures shows the lab setup that is going to be used in future. Fig. 8.1 shows the analog model power system on the right and flywheel coupled induction machines on the left.

Fig. 8.1. Analog model power system

(From left to right Amit Somani, Ganesh Balasubramanian, Mangapathi Mynam, Dr.Johnson and Satish Samineni)

Fig. 8.2 shows an induction machine, flywheel and DC machine connected to the same shaft. The DC machine is used for supplying energy storage system losses.

Fig. 8.2. Flywheel coupled induction machine

The practical approach is to build and test two separate models: a static series compensator and a field oriented control AC drive, the same strategy that was followed in EMTDC modeling. A static series compensator can be built and tested by replacing the field oriented control AC drive with a DC source. Similarly a field oriented control AC drive can be built by replacing the static series compensator with a DC source. Upon successful completion of this testing, they can be integrated and tested with the proposed outer control system. The laboratory results will be compared with the simulation results and the flywheel energy storage system performance can be analyzed.

There are several challenges that might arise during practical implementation, especially software coding for controlling the power converters, parameter dependancy of indirect field oriented controller and designing tests for obtaining induction machine parameters, filter design and series transformer design.

The EMTDC models developed in this thesis could be used as a starting point to investigate the following:

- Flywheel energy storage system performance with a flux observer in the indirect field oriented controller. A flux observer eliminates the parameter dependancy of indirect field oriented controller thus improving the performance of the control system.

- Performance analysis of a flywheel energy storage system for voltage swell correction on ungrounded systems. The energy storage system can be used for mitigating swells in a fashion similar to that for mitigating voltage sags by simply adding a swell detector.

- An adaptive flywheel energy storage system that can switch from static series compensator during sag/swell corrections to static shunt compensator for mitigating interruptions. The static shunt compensator with energy storage system then acts as a UPS. This adaptive energy storage system is an efficient way for mitigating sags, swells and interruptions as it uses the combined advantages of static series compensator and static shunt compensator.

- The static series compensator can act as an active filter for mitigating voltage harmonics. An analysis should be performed on the tradeoffs between sag correction and harmonic correction.

- Modeling and analysis of a Static Synchronous Series Compensator (SSSC) for power flow applications. SSSC is used for controlling the transmission line loading, thereby improving the transmission capacity. In other words it can make a line look shorter or longer thereby increasing or decreasing the real power transfer capability. With energy storage, a SSSC can be used for improving transient stability and damping power oscillations.

- Implementation of a dynamically varying torque limiter in the proposed sag corrector that limits the T_{SAG} value depending on the amount of energy available for discharge and stability of the storage system.

BIBILIOGRAPHY

[1] G. Genta, *Kinetic Energy Storage*, University Press, Cambridge, 1985.

[2] A. Ter-Gazarian, *Energy Storage Systems For Power Systems*, IEE Power and Energy Series, 1994.

[3] J. G. Ciezki, R. W. Ashton, "Selection and stability issues associated with a Navy shipboard DC Zonal electric distribution system," *IEEE Transactions on Power Delivery*, Vol. 15, No. 2, pp. 665-669, April 2000.

[4] Math. H. J. Bollen, *Understanding Power Quality Problems*, IEEE Press, 2000.

[5] A. T. Adediran, H. Xiao and K.L. Butler, "Fault Studies of an U.S. Naval Shipboard Power System," NAPS, Univerity of Waterloo, Canada, pp 1-18 to 1-25, October 2000.

[6] R. S. Weissbach, G. G. Karady and R. G. Farmer, "Dynamic Voltage Compensation on Distribution Feeders using Flywheel Energy Storage," *IEEE Transactions on Power Delivery*, Vol.14, No.2, pp. 465-471, April 1999.

[7] *PSCAD/EMTDC User's Manual*, Manitoba HVDC Research Center, Manitoba, Canada.

[8] B. K. Bose, *Modern Power Electronics and AC Drives*, Prentice Hall PTR, 2002.

[9] *Field Oriented Control of 3 phase AC Motors*, BPRA073, Texas Instruments Europe, 1998.

[10] D. W. Novotny and T. A. Lipo, *Vector Control and Dynamics of AC Drives*, Oxford Science Publications, 1997.

[11] P. L. Jansen and R. D. Lorenz, "A Physically Insightful Approach to the Design and Accuracy Assessment of Flux Observers for Field Oriented Induction Machine Drives," *IEEE Transactions on Industry Applications,* Vol 30, No. 1, pp. 101-110, Jan/ Feb., 1994.

[12] H. W. Van Der Broeck, H. C. Skudelny and G. V. Stanke, "Analysis and Realization of a Pulsewidth Modulator Based on Voltage Space Vectors," *IEEE Transactions on Industry Applications*, Vol.24, No.1, pp. 142-150, January/February 1988.

APPENDIX A

10.1 Three phase variable representation of induction machine voltage equations

The stator and rotor circuit voltage equations of an induction machine can be conveniently written in matrix form:

$$v_{abcs} = r_s \cdot i_{abcs} + p \cdot \lambda_{abcs} \tag{10.1}$$

$$0 = r_r \cdot i_{abcr} + p \cdot \lambda_{abcr} \tag{10.2}$$

where p is d/dt and v_{abcs}, i_{abcs} and λ_{abcs} (stator voltage, stator current and stator flux in abc reference) are 3X1 vectors defined by:

$$v_{abcs} = \begin{pmatrix} v_{as} \\ v_{bs} \\ v_{cs} \end{pmatrix} \qquad i_{abcs} = \begin{pmatrix} i_{as} \\ i_{bs} \\ i_{cs} \end{pmatrix} \qquad \lambda_{abcs} = \begin{pmatrix} \lambda_{as} \\ \lambda_{bs} \\ \lambda_{cs} \end{pmatrix} \tag{10.3}$$

The rotor variables i_{abcr} and λ_{abcr} are similar.

The stator and rotor circuits have inductive coupling, so the flux linkages can be written in terms of machine currents as follows:

$$\lambda_{abcs} = \lambda_{ss} + \lambda_{sr} \tag{10.4}$$

$$\lambda_{abcr} = \lambda_{rs} + \lambda_{rr} \tag{10.5}$$

where:

$$\lambda_{ss} = \begin{pmatrix} L_{as} & L_{abs} & L_{acs} \\ L_{abs} & L_{bs} & L_{bcs} \\ L_{acs} & L_{bcs} & L_{cs} \end{pmatrix} \cdot i_{abcs} \tag{10.6}$$

$$\lambda_{sr} = \begin{pmatrix} L_{asar} & L_{asbr} & L_{ascr} \\ L_{bsar} & L_{bsbr} & L_{bscr} \\ L_{csar} & L_{csbr} & L_{cscr} \end{pmatrix} \cdot i_{abcr} \tag{10.7}$$

$$\lambda_{rs} = \begin{pmatrix} L_{as} & L_{abs} & L_{acs} \\ L_{abs} & L_{bs} & L_{bcs} \\ L_{acs} & L_{bcs} & L_{cs} \end{pmatrix} \cdot i_{abcs} \tag{10.8}$$

$$\lambda_{rr} = \begin{pmatrix} L_{ar} & L_{abr} & L_{acr} \\ L_{abr} & L_{br} & L_{bcr} \\ L_{acr} & L_{bcr} & L_{cr} \end{pmatrix} \cdot i_{abcr} \tag{10.9}$$

Note, the mutual inductances between stator and rotor windings are dependent on the rotor position θ_r, so λ_{sr} and λ_{rs} are functions of θ_r.

10.2 Space vector representation of induction machine voltage equations

The stator and rotor circuit equations of an induction machine can be conveniently written in space vector form as:

$$v_{abcs} = r_s \cdot i_{abcs} + p \cdot \lambda_{abcs} \tag{10.10}$$

$$0 = r_r \cdot i_{abcr} + p \cdot \lambda_{abcr} \tag{10.11}$$

where

$$v_{abcs} = \frac{2}{3} \cdot \left(v_{as} + \alpha \cdot v_{bs} + \alpha^2 \cdot v_{cs} \right) \tag{10.12}$$

0 j120deg

and α is a 120 operator (1.0e) . Similarly for i^{abcs}, v^{abcr} and i^{abcr}.

This approach helps in representing the induction machine voltage equations in a compact form. However the mutual inductances between stator and rotor windings are still dependent on the rotor position θ_r, so λ_{sr} and λ_{rs} are still functions of θ_r.

10.3 Stationary DQ reference frame representation of induction machine voltage equations

The stator and rotor circuit equations of an induction machine can be conveniently written as stationary DQ reference variables in the form:

$$v_{qds}^{s} = r_s \cdot i_{qds}^{s} + p \cdot \lambda_{qds}^{s} \tag{10.13}$$

$$0 = r_r \cdot i_{qdr}^{s} + p \cdot \lambda_{qdr}^{s} - j \cdot \omega_r \cdot \lambda_{qdr}^{s} \tag{10.14}$$

where

$$v_{qds}^{s} = v_{qs}^{s} - j \cdot v_{ds}^{s}$$

$$iqds^{s} = iqs^{s} - j.ids^{s}$$

$$\lambda_{qds}^{s} = \lambda_{qs}^{s} - j \cdot \lambda_{ds}^{s}$$

(10.15)

$$i_{qdr}^{s} = i_{qr}^{s} - j \cdot i_{dr}^{s}$$

$$\lambda_{qdr}^{s} = \lambda_{qr}^{s} - j \cdot \lambda_{dr}^{s}$$

This assumes that v_{qdr}^{s} is zero (secondary short circuited).

The electromagnetic torque can be calculated using:

$$T_e = \frac{3}{2} \cdot \left(\frac{P}{2}\right) \cdot \mathrm{Im}\left(i_{qdr}^{s} \cdot \overline{\lambda_{qdr}^{s}}\right) \qquad (10.16)$$

where P is the number of stator poles.

The torque can be calculated from a combination of any of the variables discussed above. Equation (10.16) is one possible form.

Then the rotor angular velocity, ω_r can be calculated using:

$$T_e = T_L + \frac{2}{P} J \cdot p \cdot \omega_r \qquad (10.17)$$

where T_L is the load torque, J is the inertia of the rotor.

10.4 Synchronous DQ reference frame representation of induction machine voltage equations

The stator and rotor circuit equations of an induction machine can be conveniently written in stationary DQ reference variables form:

$$v_{qds} = r_s \cdot i_{qds} + p \cdot \lambda_{qds} + j \cdot \omega_e \cdot \lambda_{qds} \tag{10.18}$$

$$0 = r_r \cdot i_{qdr} + p \cdot \lambda_{qdr} + j \cdot \left(\omega_e - \omega_r\right) \cdot \lambda_{qdr} \tag{10.19}$$

and

$$\lambda_{qds} = L_s \cdot i_{qds} + L_m \cdot i_{qdr} \tag{10.20}$$

$$\lambda_{qdr} = L_r \cdot i_{qdr} + L_m \cdot i_{qds} \tag{10.21}$$

$$\lambda_{qdm} = L_m \cdot \left(i_{qds} + i_{qdr}\right) \tag{10.22}$$

L_s and L_r are given by:

$$L_s \quad L_{ls} + L_m \qquad L_r \quad L_{lr} + L_m \tag{10.23}$$

where L_{ls} and L_{lr} are leakage reactances of stator and rotor respectively and L_m is magnetizing inductance. Then the electromagnetic torque can be calculated using:

$$T_e = \frac{3}{2} \cdot \left(\frac{P}{2}\right) \cdot L_m \cdot \mathrm{Im}\left(i_{qds} \cdot \overline{i_{qdr}}\right)$$

$$T_e = \frac{3}{2} \cdot \left(\frac{P}{2}\right) \cdot \frac{L_m}{L_r} \cdot \mathrm{Im}\left(i_{qds} \cdot \overline{\lambda_{qdr}}\right) \tag{10.24}$$

10.5 State space flux equations for modeling induction machine

The following procedure gives an introduction for deriving state space flux equations useful for modeling induction machines.

Consider a Q-axis based form of equation (10.18)

$$v_{qs} = r_s \cdot i_{qs} + p \cdot \lambda_{qs} + \omega_e \cdot \lambda_{qs} \tag{10.25}$$

Consider a Q-axis based form of equations (10.20) and (10.21)

$$\lambda_{qs} = L_s \cdot i_{qs} + L_m \cdot i_{qr} \tag{10.26}$$

$$\lambda_{qr} = L_r \cdot i_{qr} + L_m \cdot i_{qs} \tag{10.27}$$

Rearranging equations (10.26) and (10.27) for i_{qs}, i_{qr} results in:

$$i_{qs} = \frac{\lambda_{qs} - L_m \cdot i_{qr}}{L_s} \tag{10.28}$$

$$i_{qr} = \frac{\lambda_{qr} - L_m \cdot i_{qs}}{L_r} \tag{10.29}$$

Substituting equation (10.29) in (10.28) and rearranging:

$$i_{qs} = \frac{\lambda_{qs} - L_m \cdot \left(\frac{\lambda_{qr} - L_m \cdot i_{qs}}{L_r} \right)}{L_s} = \frac{\lambda_{qs} - L_m \cdot \frac{\lambda_{qr}}{L_r} + \frac{L_m^2}{L_r} \cdot i_{qs}}{L_s}$$

$$i_{qs} \cdot \sigma = \frac{\lambda_{qs}}{L_s} - \frac{L_m}{L_s \cdot L_r} \cdot \lambda_{qr} \tag{10.30}$$

$$i_{qs} = \frac{\lambda_{qs}}{\sigma \cdot L_s} - \frac{L_m}{L_s \cdot L_r \cdot \sigma} \cdot \lambda_{qr} = \left(L_r \cdot \lambda_{qs} - L_m \cdot \lambda_{qr} \right) \cdot \frac{1}{L_s \cdot L_r \cdot \sigma}$$

where

$$\sigma = 1 - \frac{L_m^2}{L_s \cdot L_r} \tag{10.31}$$

substituting the simplified form of (10.30) in (10.25), results in:

$$p \cdot \lambda_{qs} = v_{qs} + \left(L_r \cdot \lambda_{qs} - L_m \cdot \lambda_{qr} \right) \cdot \frac{r_s}{L_s \cdot L_r \cdot \sigma} - \omega_e \cdot \lambda_{ds} \tag{10.32}$$

The same procedure can be applied for deriving state space flux equations for λ_{ds}, λ_{qr} and λ_{dr}.

10.6 Indirect field oriented controller equations

The objective for field oriented control is to zero out the flux linkage along the q-axis, so:

$$\lambda_{qr} = 0 \tag{10.33}$$

Substituting equation (10.33) in equations (10.19) and separating it in q and d forms results in:

$$0 = r_r \cdot i_{qr} + \left(\omega_e - \omega_r\right) \cdot \lambda_{dr} \tag{10.34}$$

$$0 = r_r \cdot i_{dr} + p \cdot \lambda_{dr} \tag{10.35}$$

Similarly substituting equation (10.33) in equation (10.21) and writing it in q form separately:

$$\lambda_{qr} = L_m \cdot i_{qs} + L_r \cdot i_{qr} = 0 \tag{10.36}$$

Similarly substituting equation (10.33) in flux linkage form for torque in equation (10.24):

$$Te = \frac{3}{2} \cdot \left(\frac{P}{2}\right) \cdot \frac{L_m}{L_r} \cdot \left(iqs \cdot \lambda dr\right) \tag{10.37}$$

Using equations (10.34) and (10.36) for slip angular velocity expression:

$$i_{qr} = -\frac{L_m}{L_r} \cdot i_{qs} \tag{10.38}$$

$$\omega_e - \omega_r = S \cdot \omega_e = \omega_{sl} = -\frac{r_r \cdot i_{qr}}{\lambda_{dr}} \tag{10.39}$$

$$\omega_{sl} = \frac{r_r \cdot L_m \cdot i_{qs}}{L_r \cdot \lambda_{dr}} \tag{10.40}$$

Using the d form of equation (10.21) and simplifying:

$$\lambda_{dr} = L_r \cdot i_{dr} + L_m \cdot i_{ds} \tag{10.38}$$

$$\lambda_{dr} = L_r \cdot \left(-\frac{p \cdot \lambda_{dr}}{r_r} \right) + L_m \cdot i_{ds} \tag{10.39}$$

$$\lambda_{dr} \quad \frac{L_m \cdot i_{ds}}{1 + \tau_r \cdot p} \tag{10.40}$$

where

$$\tau_r = \frac{L_r}{r_r} \tag{10.41}$$

Using the q form of equation (10.20) and simplifying:

$$\lambda_{qs} = L_s \cdot i_{qs} + L_m \cdot i_{qr} = L_s \left(1 - \frac{L_m^{\,2}}{L_s \cdot L_r} \right) \cdot i_{qs} = \sigma \cdot L_s \cdot i_{qs} \tag{10.42}$$

Using the d form of equation (10.20) and simplifying:

$$\lambda_{ds} = L_s \cdot i_{ds} + L_m \cdot i_{dr}$$

$$\lambda ds = Ls.ids + Lm.\left(-\frac{p \cdot \lambda_{dr}}{r_r}\right)$$

$$\lambda_{ds} = L_s \cdot i_{ds} + L_m \cdot \left[-\frac{p \cdot \left(\frac{L_m \cdot i_{ds}}{1 + \tau_r \cdot p}\right)}{r_r}\right]$$

$$\lambda_{ds} = L_s \cdot i_{ds} - \frac{\tau_r \cdot L_m^{\,2} \cdot p \cdot i_{ds}}{\left(1 + \tau_r \cdot p\right) \cdot L_r} \qquad (10.43)$$

$$\lambda_{ds} = L_s \left[1 - \frac{(1 - \sigma) \cdot \tau_r \cdot p}{1 + \tau_r \cdot p}\right] \cdot i_{ds}$$

$$\lambda_{ds} = L_s \left(\frac{1 + \sigma \cdot \tau_r \cdot p}{1 + \tau_r \cdot p}\right) \cdot i_{ds}$$

Using equation (10.37) and (10.40):

$$i_{qs} = \frac{4}{3 \cdot P} \cdot \frac{L_r}{L_m} \cdot \frac{T_e}{\lambda_{dr}} \qquad (10.44)$$

$$i_{ds} = \frac{1 + \tau_r \cdot p}{L_m} \cdot \lambda_{dr} \qquad (10.45)$$

APPENDIX B

EMTDC/PSCAD diagrams

The following figures show the PSCAD/EMTDC diagrams of a flywheel energy storage system model. The PSCAD/EMTDC implementation of models discussed in Chapters 4, 5 and 6 are shown in this chapter.

11.1 Flywheel energy storage system electrical model

Fig. 11.1 shows the PSCAD/EMTDC layout of the flywheel energy storage system electrical model. Fig. 11.1 was split at the common DC link, into Fig. 11.2 and Fig. 11.3 for clarity.

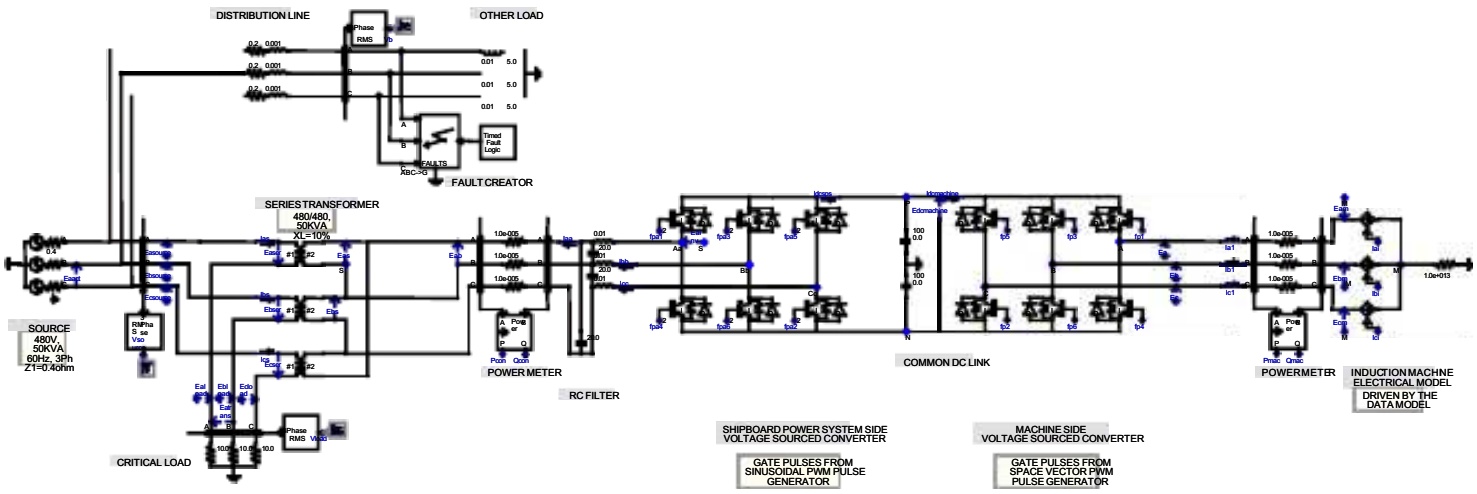

Fig. 11.1. Flywheel energy storage system model

11.2 Flywheel energy storage system electrical model

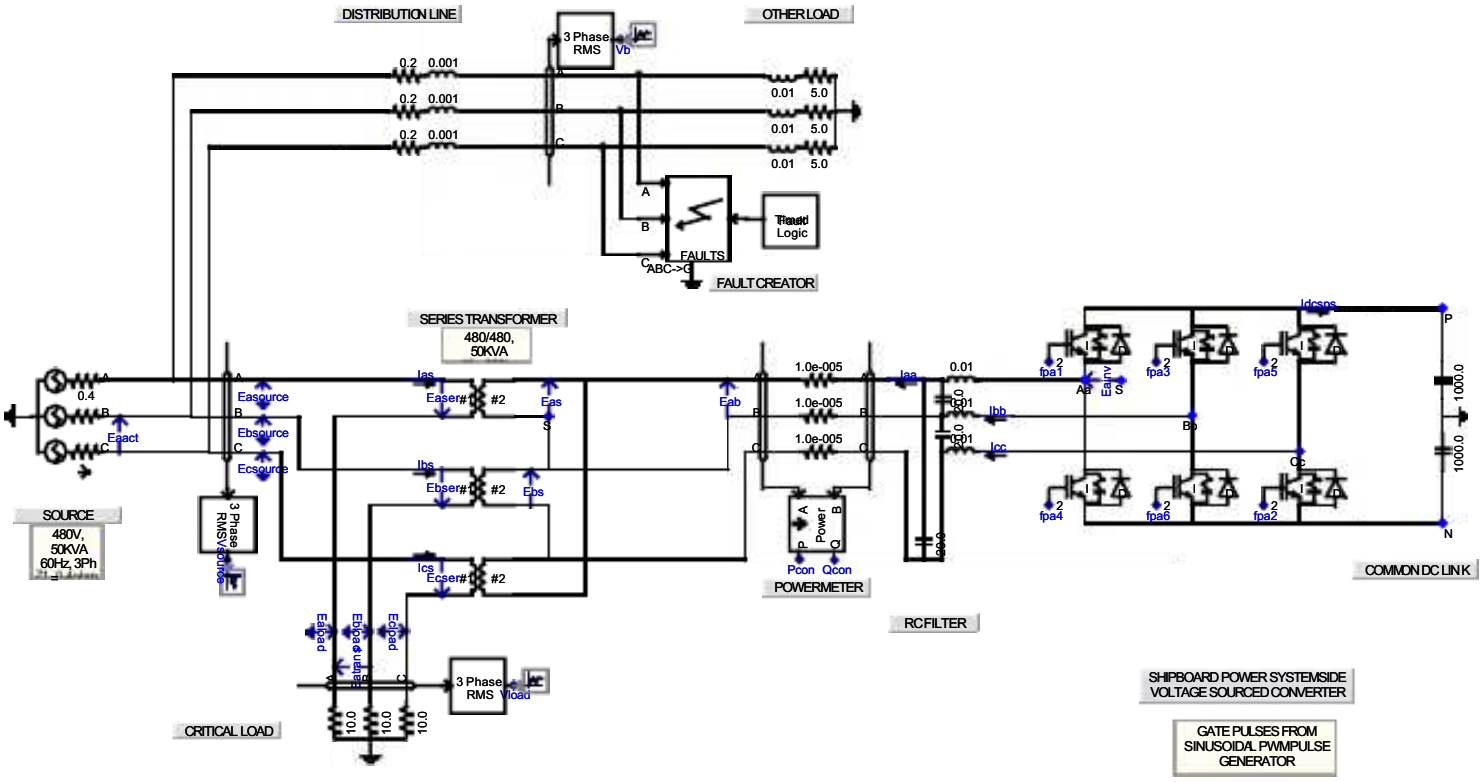

Fig. 11.2. Static series compensator model

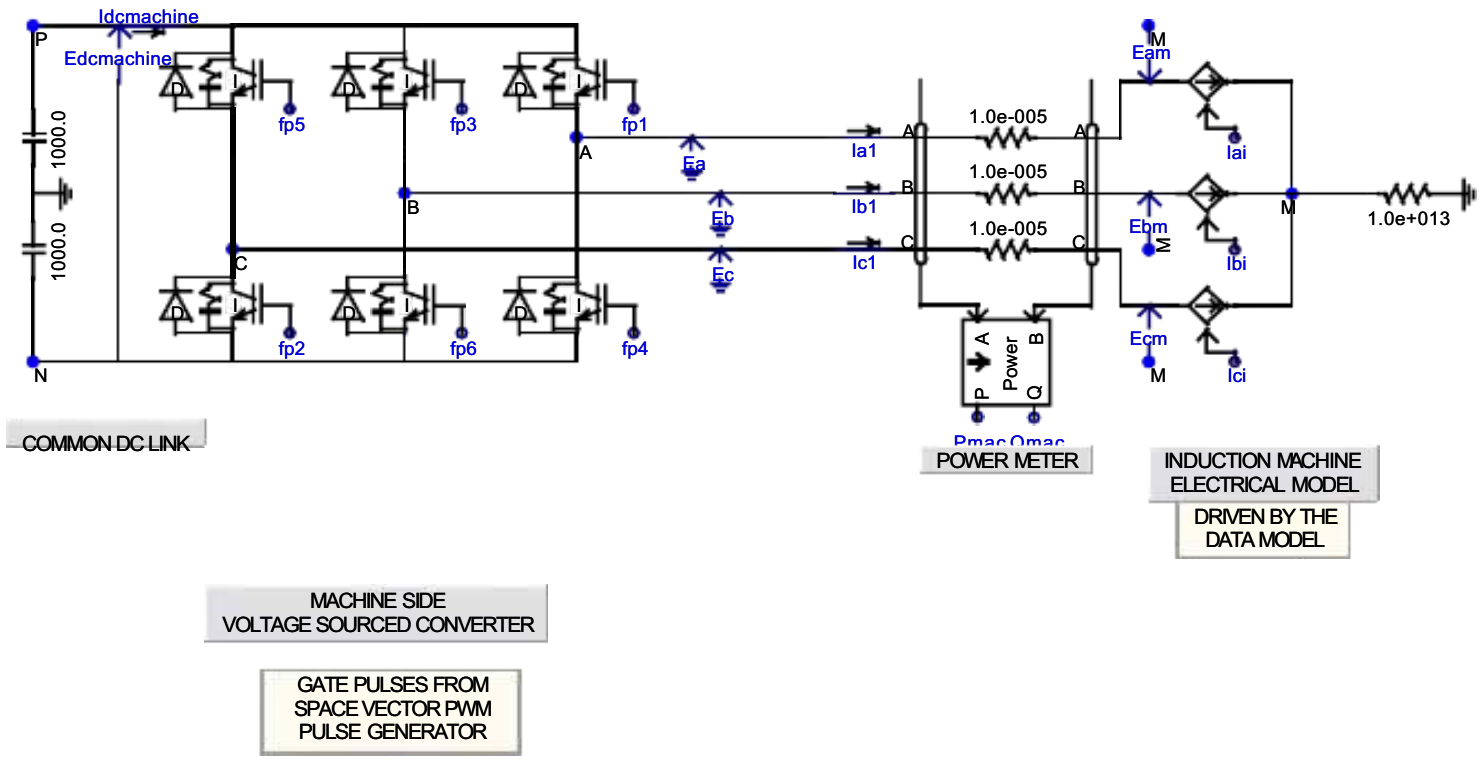

Fig. 11.3. Field oriented control AC drive model

11.3 Flywheel energy storage inner and outer control system and data models

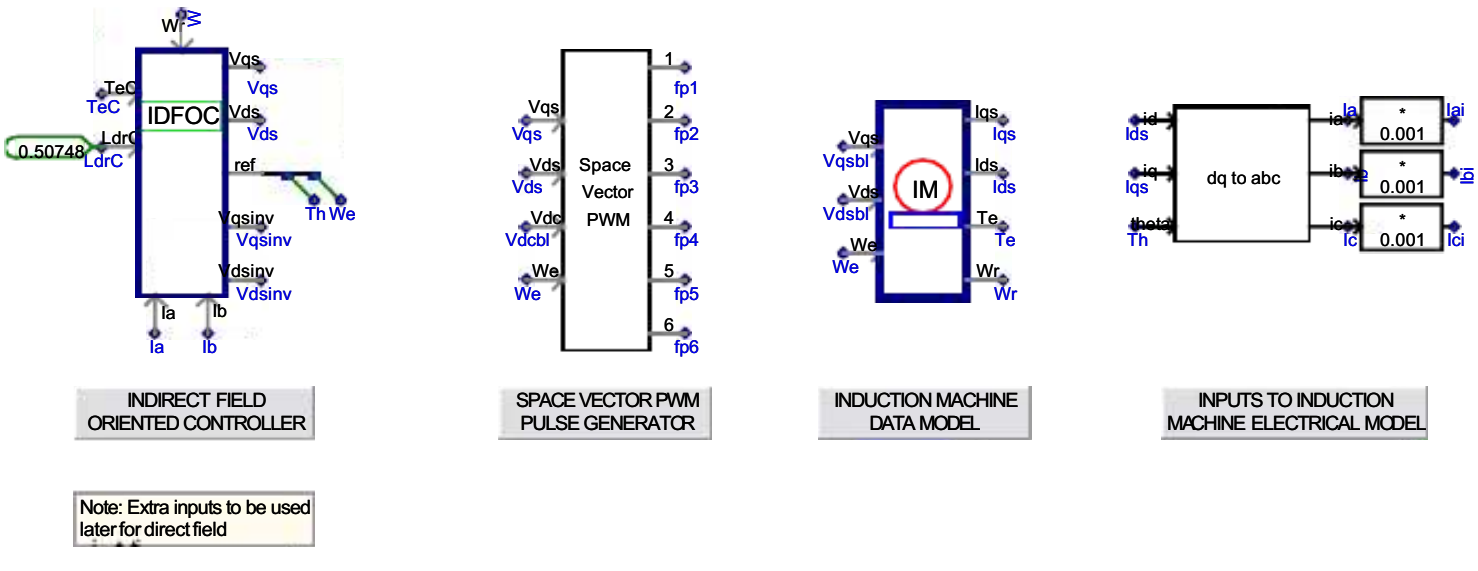

Fig. 11.4. Machine side inner control system

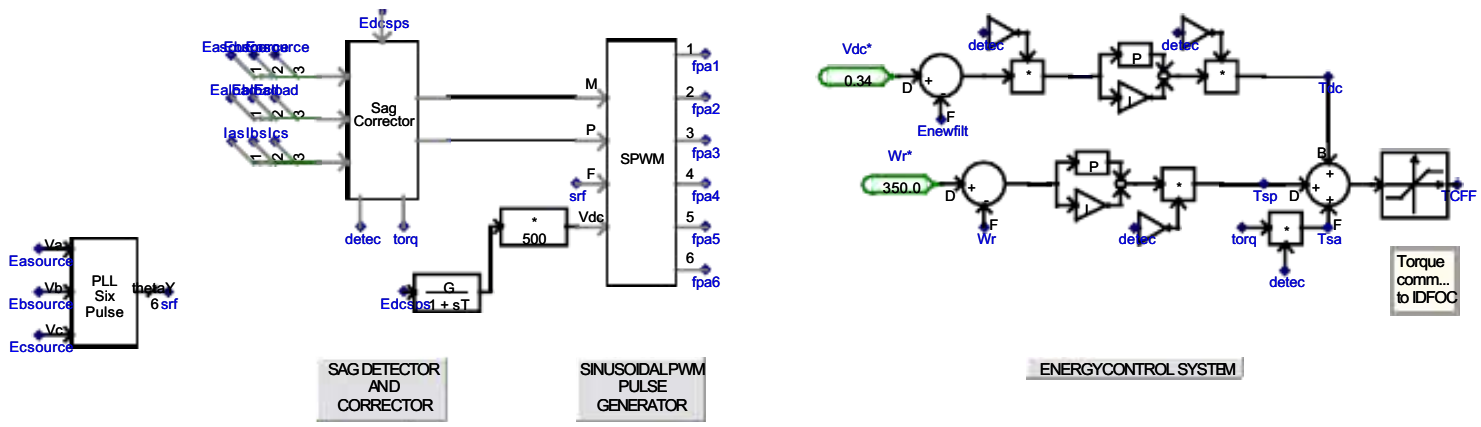

Fig. 11.5. Shipboard power system side inner control system and outer control system

11.4 Space vector PWM pulse generator model

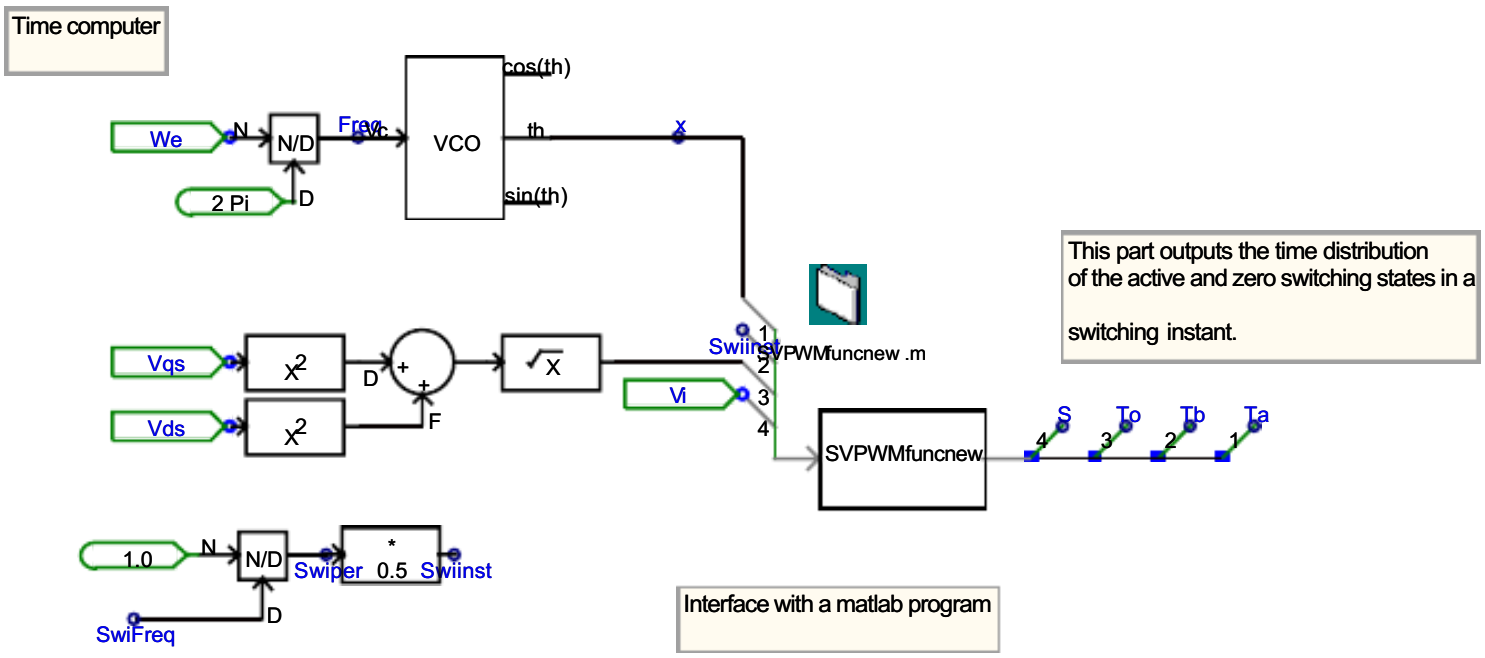

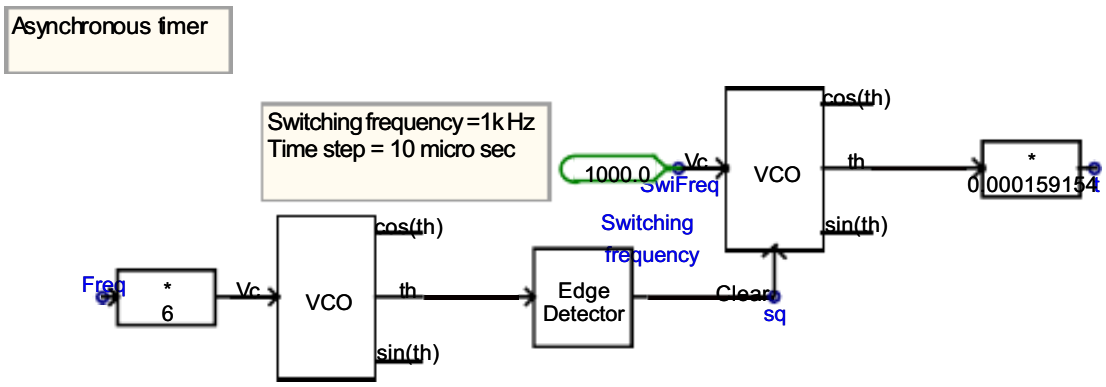

Fig. 11.6. Space vector PWM pulse generator model part-1

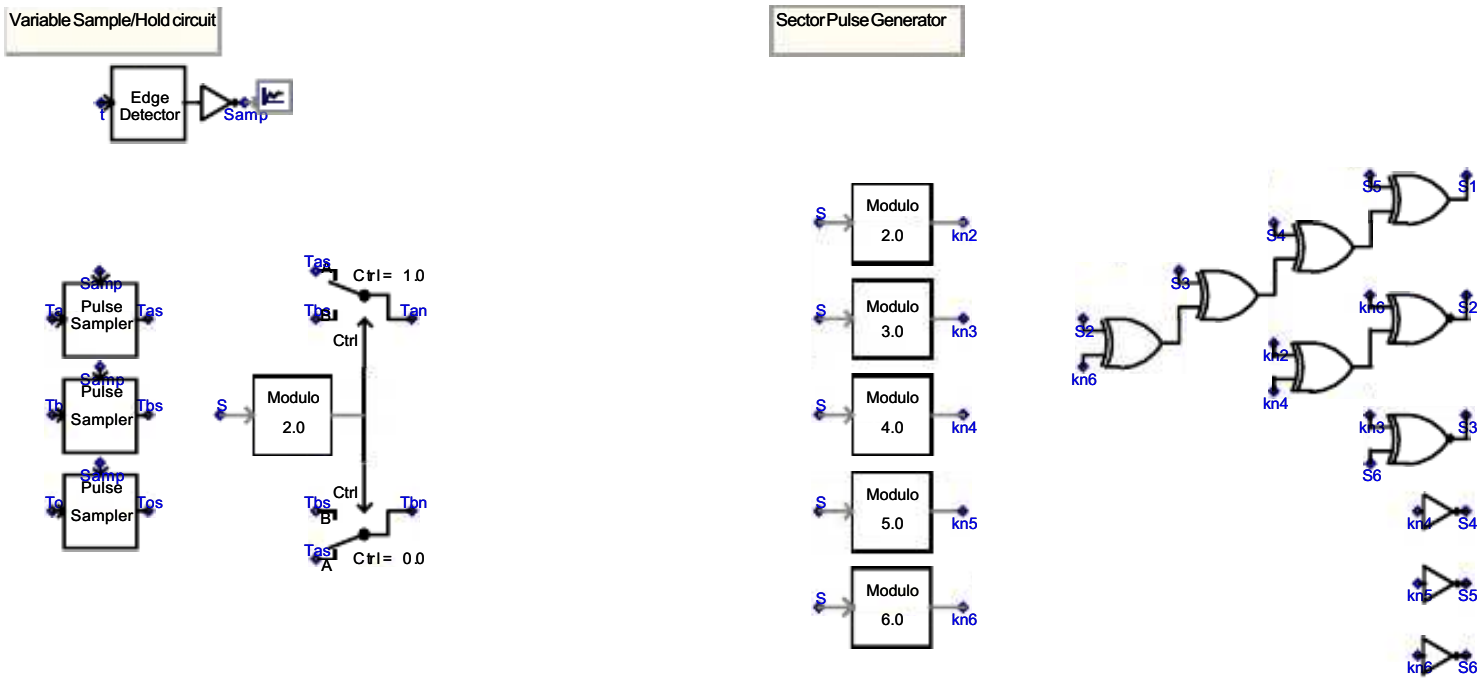

Fig. 11.7. Space vector PWM pulse generator model part-2

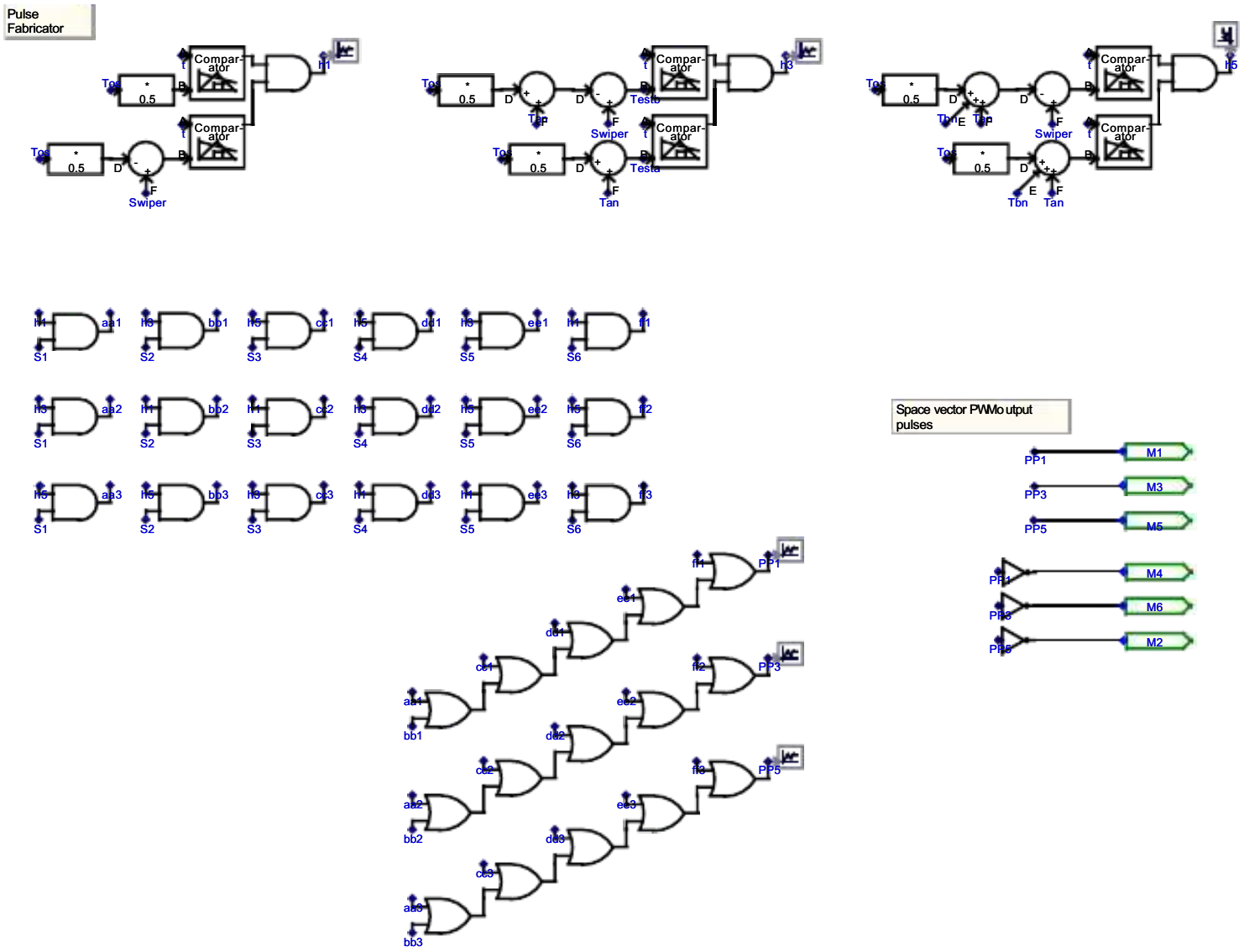

Fig. 11.8. Space vector PWM pulse generator model part-3

11.5 Sag detector and corrector

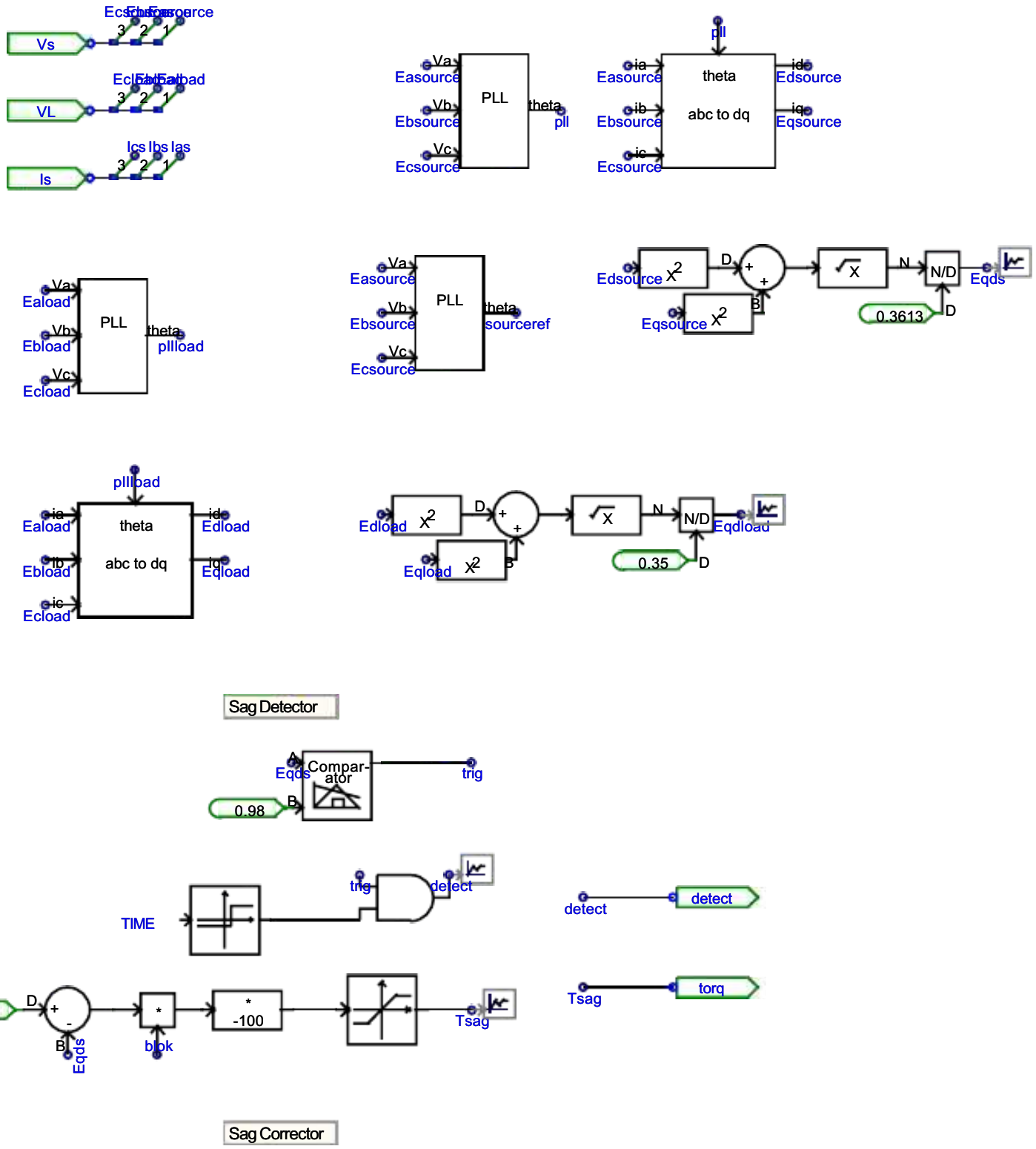

Fig. 11.9. Sag detector and corrector model

11.6 Sinusoidal PWM pulse generator model

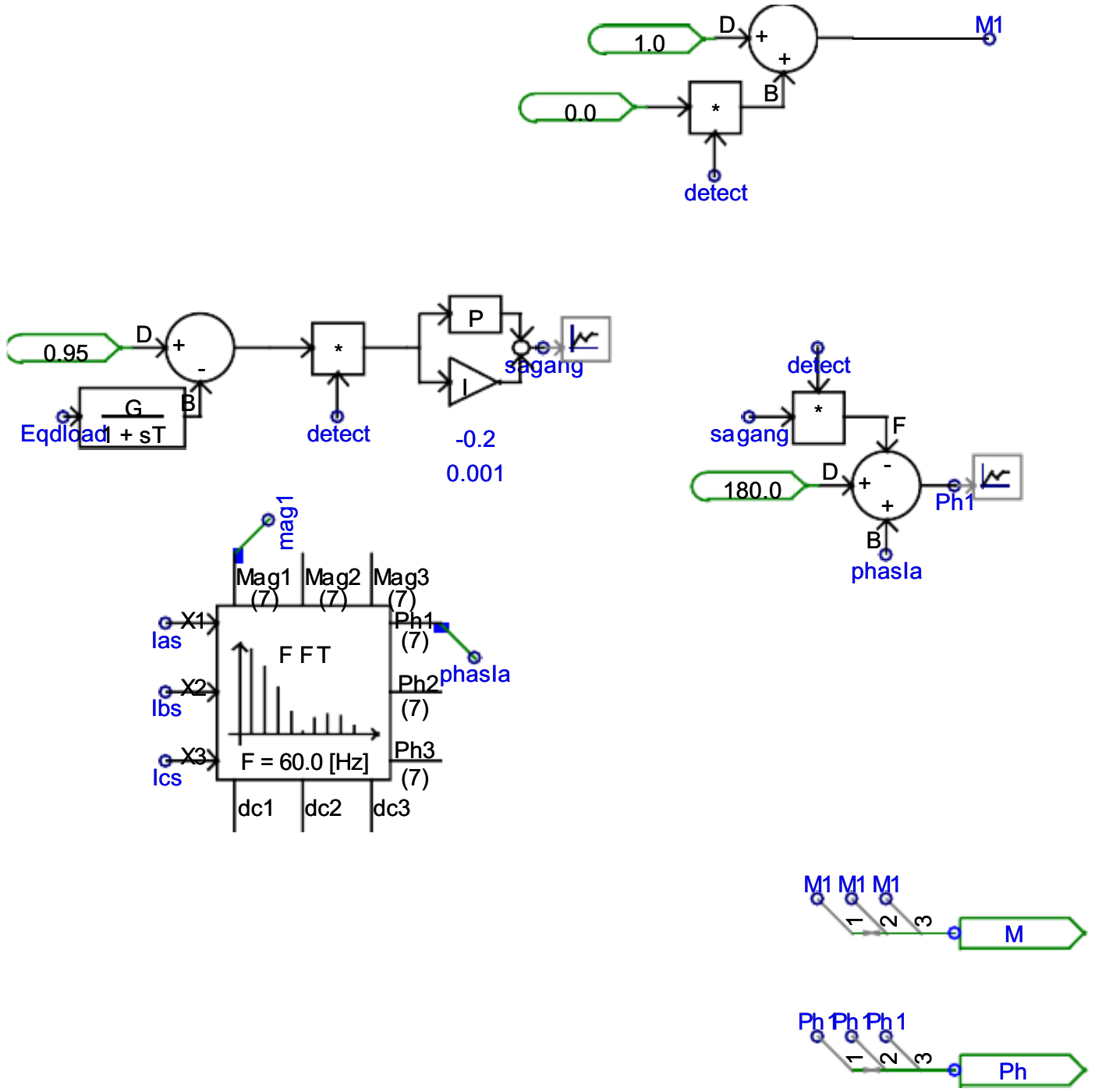

Fig. 11.10. Sinusoidal PWM pulse generator model part-1

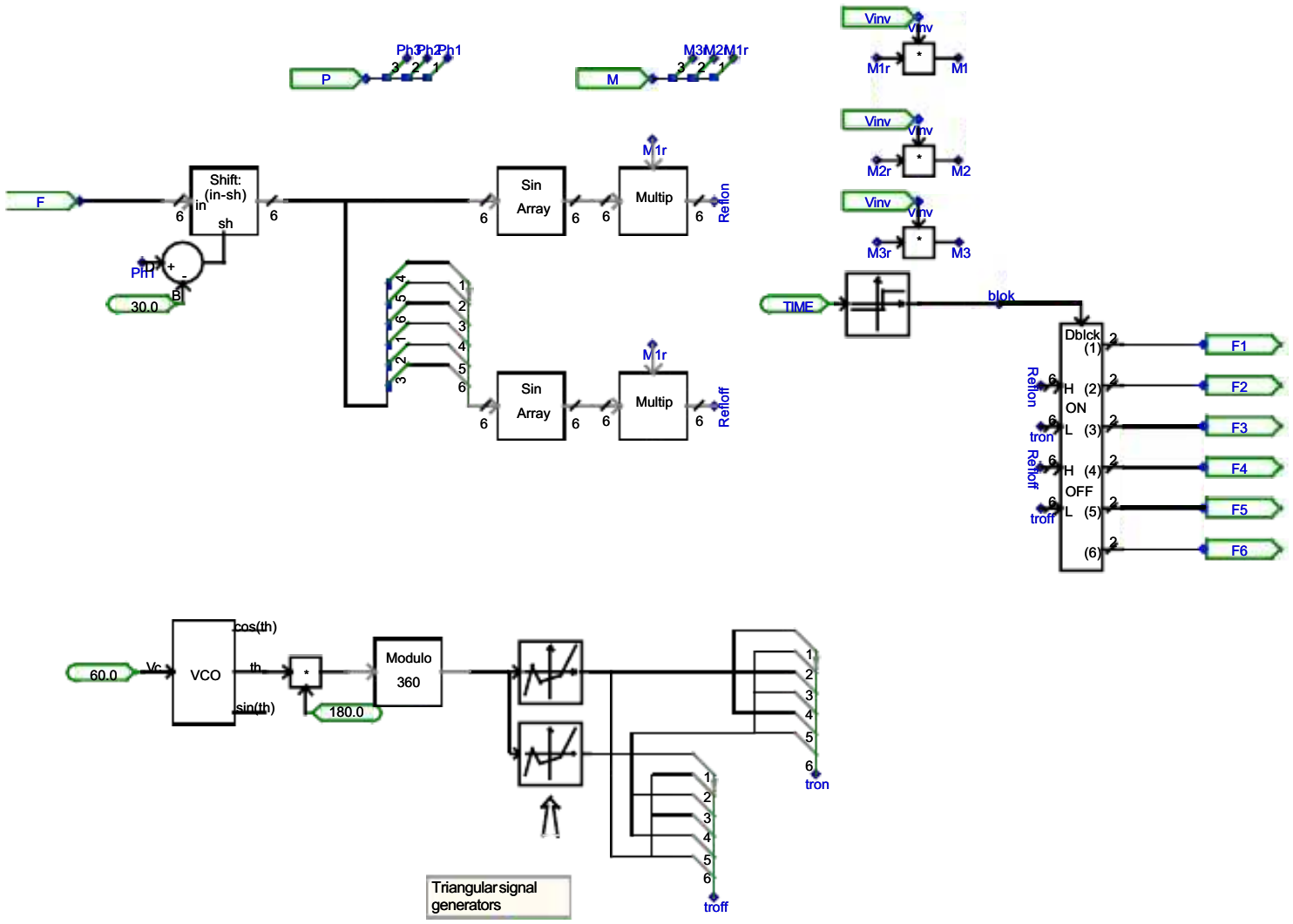

Fig. 11.11. Sinusoidal PWM pulse generator model part-2

11.7 Technical data

Table 11.1 Technical data

Shipboard Power system	3Ph, 480V, 60Hz, 50kVA
Series Transformer	480/480V, 50kVA, 10%
LC Filters	10mH, 20μF
Critical Load	Passive, 3Ph-Resistive load, 10Ω
Other Loads	Passive, 3Ph-RL load, 5Ω, 10mH
Line Impedance to other loads	0.2Ω, 1mH
DC Bus	340V, 2X1000μF center tapped
Flywheel Inertia	0.911 kg-m^2
Induction Machine	240V, 60Hz, 23.8A, 10hp, 4pole and 1755RPM
SVPWM switching frequency	1kHz
SPWM switching frequency	10.8kHz

11.8 Induction machine parameters (Courtesy Dr. Joseph D. Law)

$R_s := 0.162\,\Omega$ $R_r := 0.317\,\Omega$

$\omega_e := 376.99112\,\frac{rad}{s}$

$L_m := 0.05367\,H$ $L_{ls} := 0.001299\,H$ $L_{lr} := 0.001949\,H$

$L_s := L_{ls} + L_m$ $L_r := L_{lr} + L_m$

$L_s := 0.05497\,H$ $L_r := 0.05562\,H$

$\lambda_{drrated} := 0.50748 \cdot Wb$

$P := 4$

$J_{ind} := 0.089\,kg \cdot m^2$ $J_{flywheel} := 0.911\,kg \cdot m^2$

$J_{tot} := J_{ind} + J_{flywheel}$

$J_{tot} := 1.0 kg \cdot m^2$

11.9 Fortran file for MATLAB interface component

```
#STORAGE REAL:8
#DEFINE INTEGER I_CNT

    IF($Enabl.GT.0.9) THEN

       DO I_CNT=1,4,1
          STORF(NSTORF+I_CNT-1) = $In(I_CNT)
       END DO

       CALL MLAB_INT("$Path", "$Name", "R(4)" , "R(4)" )

       DO I_CNT=1,4,1
          $Out(I_CNT) = STORF(NSTORF+4+I_CNT-1)
       END DO
    ENDIF

 NSTORF = NSTORF + 8
```

11.10 MATLAB program

```
function [T] = SVPWMfuncnew (in)

global x Tz Vs Vi

x=in(1);
Tz=in(2);
Vs=in(3);
Vi=in(4);


if (x >= 0) & (x <= pi/3)
    k=0;
    T= SVP(k,x,Tz,Vs,Vi);
    T(4)=1.0;
 elseif (x >= pi/3) & (x <= 2*pi/3)
    k=pi/3;
    T= SVP(k,x,Tz,Vs,Vi);
    T(4)=2.0;
 elseif (x >= 2*pi/3) & (x <= pi)
    k=2*pi/3;
    T= SVP(k,x,Tz,Vs,Vi);
    T(4)=3.0;
 elseif (x >= pi) & (x <= 4*pi/3)
    k=pi;
```

```
    T= SVP(k,x,Tz,Vs,Vi);
    T(4)=4.0;
 elseif (x >= 4*pi/3) & (x <= 5*pi/3)
    k=4*pi/3;
    T= SVP(k,x,Tz,Vs,Vi);
    T(4)=5.0;
 elseif (x >= 5*pi/3)
    k=5*pi/3;
    T= SVP(k,x,Tz,Vs,Vi);
    T(4)=6.0;

end



function [T] = SVP(k,x,Tz,Vs,Vi)

if (x >= k) & (x <= (k+pi/6))
      T(1)=(sqrt(3))*(Vs/Vi)*Tz*sin(k+(pi/3)-x);
      if T(1) > Tz
      T(1)=Tz; T(2)=0; T(3)=0;
      else
      T(2)=(sqrt(3))*(Vs/Vi)*Tz*sin(x-k);
      if (T(1)+T(2)) > Tz
      T(2)=Tz-T(1); T(3)=0;
      else
      T(3)=Tz-(T(1)+T(2));
      end
      end
      else
      T(2)=(sqrt(3))*(Vs/Vi)*Tz*sin(x-k);
      if T(2) > Tz
      T(2)=Tz; T(1)=0; T(3)=0;
      else
      T(1)=(sqrt(3))*(Vs/Vi)*Tz*sin(k+(pi/3)-x);
      if (T(1)+T(2)) > Tz
      T(1)=Tz-T(2); T(3)=0;
      else
      T(3)=Tz-(T(1)+T(2));
      end
      end
end
```